POLITECNICO DI TORINO

Master's Degree in Automotive Engineering

Master's Degree Thesis

Integrating Fuel Cell, Battery, and Supercapacitors in Hybrid Electric Vehicles: Modeling, Control, and Hardware-in-the-Loop Considerations

Supervisor

Prof. Angelo BONFITTO

Co-supervisor

PhD candidate Saulius PAKŠTYS

Candidate

Jodie Edith Juliette RERAT

October 2023

Acknowledgements

I would like to thank Professor Bonfitto for being my supervisor and having given me the opportunity to study this field of research and to write this thesis. Many thanks go to Saulius Pakštys, who has been most helpful and patient in guiding me and discussing my work.

I also want to thank my family - my parents and my sister - who have been there for me in spite of the physical distance that has separated us these past 2 years. Their unwavering support is the reason I am here in the first place.

Finally, I want to thank all of my friends who have been kind enough to listen to me vent, brag, despair, hope and everything in between along the long and winding road that is writing a thesis.

I do want to end by specifically expressing my profound gratitude to Consiglia, Enrico and Fabrizio, Luca, Mattia and Nicola, and Claudia and Marco for their support in times of need.

Abstract

To meet the sustainability goals set by the European parliament by 2050 and attain the so-called "net-zero" emissions standard, the automotive industry will need to walk away from traditionally combustion-powered vehicles and develop alternative hybrid powertrains to propel private and commercial vehicles alike. In particular, hydrogen-powered vehicles have a lot of potential, especially if combined to a battery to palliate the slow dynamics of a fuel cell. However, the production of batteries is resource-intensive and their life cycle can be significantly shortened depending on the use case.

In this thesis, a model of a fuel cell hybrid electric light-duty vehicle has been proposed, with the fuel cell paired in series with a downsized battery with respect to the battery-only version. To determine the power delivered by the fuel cell stack to the battery, two types of energy management strategies have been defined, a rule-based control with two working modes and a formulation-based strategy depending on the state of charge of the battery and a tuning factor, optimized with the bisection method.

Supercapacitors have been added in parallel to the battery in order to take on the more stringent power requests and have been shown to preserve battery life through reduced C-rates. The associated control logic has been defined as a rule-based control strategy whose parameters have been optimized through two designs of experiment.

In order to control the validity of the model and associated control logics, a hardware-in-the-loop test bench is necessary. To be compatible with safety and laboratory requirements, a scaled-down version of the vehicle is preferable for implementation of the test bench. Therefore, a method for scaling down the electric machine has been chosen among the literature, its implementation tested and compared to results from the full-scale model simulation and its logic reversed to compute the scaling-down factor of the vehicle from the desired scaled-down power request. It has permitted to downscale the electric machine but research must still be conducted for scaling down the power sources components.

Table of Contents

List of Tables v

List of Figures vi

Acronyms ix

1 Introduction 1

2 Fuel cell hybrid electric vehicle modeling 9
2.1 General structure of the vehicle model 9
2.2 Architecture 12
2.2.1 Parallel 12
2.2.2 Series 13
2.3 Power sources modeling 14
2.3.1 Battery 15
2.3.2 Supercapacitors 21
2.3.3 Fuel cell stack 22

3 Simulation, analysis and comparison of different vehicle models 25
3.1 Analysis of fuel cell stack addition impact 25
3.1.1 Rule-Based Control strategy for the power delivery by the fuel cell stack 25
3.1.2 Battery downsizing 28
3.2 Evaluation of supercapacitors' impact on a fuel cell hybrid electric vehicle 29
3.2.1 Measure of supercapacitors' impact on battery life 37
3.3 Design of an adaptive energy management strategy for the fuel cell stack 38
3.3.1 Adaptive strategy 38
3.3.2 Comparison between rule-based and adaptive control strategies 40
3.3.3 Charge sustaining considerations 42

4 Scaling-down method for hardware-in-the-loop applications 47
4.1 Literature review of scaling-down strategies 47
4.2 Evaluation of power computation method suitability with respect to Simulink model 48
4.2.1 Evaluation of numerical derivation schemes for the acceleration computation 49

4.2.2 Compatibility analysis between Simulink resistance force-based models 51
4.3 Computation and analysis of downscaled power request 52
4.4 Determining the scaling factor k from a specified power ratio x . . . 54
4.5 Application to test bench 59

5 Conclusion 61

A Bisection results for adaptive strategy in charge-sustaining mode 63

Bibliography 67

List of Tables

2.1 Vehicle and environment characteristics. 9
2.2 Values of C_{batt} and associated C-rates used for the DOE. 16
2.3 Variation from initial value of SOC to minimal SOC value. 20
2.4 Characteristics of the Maxwell 2.7V 3000F Ultracapacitor Cell . . . 21
2.5 Cell characteristics for the Zubieta model. 21

3.1 Measure of impact on SOC and C-rate as a result of supercapacitors introduction. 38
3.2 Absolute values and relative difference of relevant parameters between the reference RBC strategy and the adaptive strategy. 42
3.3 Values of tuning factor γ for different values of SOC_{th} of the adaptive strategy over the WLTP cycle in charge-sustaining mode. 43
3.4 Absolute values and relative difference of relevant parameters between the reference RBC strategy and the different adaptive strategies with charge-sustaining mode on the WLTP cycle. 44

4.1 Decision table to compare the scaling-down strategies. 48
4.2 Parameters of the resistance force equations. 49
4.3 Derivation schemes and the associated expression of the acceleration. i represents the given time step. 49
4.4 Results of the comparison between the different derivation schemes with respect to the Simulink power request. 51
4.5 Definition of use cases used to test the robustness of the reverse procedure. 55
4.6 Parameters of the linear regression between $\log(k)$ and $\log(x)$ for three different scenarios. 57

List of Figures

2.1 General structure of the forward vehicle model. 10
2.2 Root structure of the Simulink model. 10
2.3 Structure of the controller. 11
2.4 Structure of the plant. 11
2.5 Torque-speed map of the electric machine. 12
2.6 Concept of the "parallel" architecture. 13
2.7 Concept of the "series" architecture. 14
2.8 Structure of the power sources. 15
2.9 Power request along the WLTP for the 7000kg vehicle. 16
2.10 Evolution of the SOC of the battery for the DOE on battery capacity. *The legend corresponds to the value (in A.h) of C_{batt} being tested.* . . . 17
2.11 Evolution of the SOC of the battery without the fuel cell stack for the DOE on battery capacity. *The legend corresponds to the value (in A.h) of C_{batt} being tested.* . . . 17
2.12 Evolution of the battery SOC for the DOE on battery capacity. *The legend corresponds to the value (in A.h) of C_{batt} being tested.* . . . 18
2.13 Evolution of the battery C-rate for the DOE on battery capacity. *The legend corresponds to the value (in A.h) of C_{batt} being tested.* . . . 18
2.14 Minimum SOC reached during the WLTP cycle as a function of C_{batt}. 19
2.15 Maximum C-rate reached during the WLTP cycle as a function of C_{batt}. 19
2.16 Block architecture of the battery model in Simulink. 20
2.17 Block architecture of the supercapacitors model in Simulink. 22
2.18 Look-up tables used for modelizing the fuel cell stack. 22
2.19 Structure of the fuel cell stack model. 23

3.1 Diagram of the RBC algorithm for the fuel cell stack. 26
3.2 Operating points for the rule-based control strategy of the fuel cell stack. 27
3.3 Results of the implemented RBC algorithm for the FCHEV without supercapacitors. 28
3.4 Time evolution of the SOC and the C-rates for the BEV and FCHEV without supercapacitors. 29
3.5 Diagram of the rule-based control algorithm for the supercapacitors. 30
3.6 Time derivative of the power request over the WLTP cycle. 31
3.7 Maximum C-rates reached by the battery during the WLTP cycle as a function of P'_{th}. 32
3.8 Minimum SOC reached during the WLTP cycle as a function of P'_{th}. 33

3.9 Maximum current reached by the supercapacitors during the WLTP cycle as a function of P'_{th}. 33
3.10 Power distribution between the battery and supercapacitors during the WLTP cycle as a function of P'_{th}. 34
3.11 Evolution of the C-rates reached by the battery during the WLTP cycle.
The legend represents the values of λ. 35
3.12 Evolution of the supercapacitors voltage during the WLTP cycle.
The legend represents the values of λ. 35
3.13 Maximum current reached by the supercapacitors during the WLTP cycle as a function of λ. 36
3.14 Power distribution between the battery and supercapacitors during the WLTP cycle as a function of λ. 36
3.15 Time evolution of the SOC and the C-rates for the FCHEV without and with supercapacitors. 37
3.16 Operating area for the adaptive strategy of the FCS 38
3.17 Tuning of γ factor through the bisection method to achieve equal SOC difference with both adaptive and rule-based control strategies. 40
3.18 Comparison of the command signals for the RBC and adaptive methods on the WLTP cycle. 41
3.19 Comparison of main results for the RBC and adaptive methods on the WLTP cycle. 41
3.20 Tuning of the threshold value of SOC_{min} through the bisection method to achieve charge-sustaining mode with the rule-based control strategy. 43
3.21 Comparison of main results for the RBC and adaptive method on the WLTP cycle when working in charge-sustaining mode. 44
3.22 Comparison of the command signals for the RBC and adaptive method on the WLTP cycle when working in charge-sustaining mode. 45
3.23 Histogram of the frequency of the fuel cell stack efficiency for the RBC and adaptive method over the WLTP cycle when working in charge-sustaining mode. 45

4.1 Comparison of power requests computed from the resistance forces with different derivation schemes for the acceleration. 50
4.2 Comparison of power requests computed from the resistance forces and from the Simulink model. 51
4.3 Full-scale and down-scaled (factor $k = 5$, $k = 7$, $k = 9$) power request over the WLTP cycle. 53
4.4 Components of the resistant force for $k = 1$, $k = 5$ and $k = 9$. . . . 54
4.5 Scaling-down factors k plotted against resulting power ratios x for three test cases. 55
4.6 Logarithm of scaling-down factors $\log(k)$ plotted against logarithm of resulting power ratios $\log(x)$ for three test cases. 56
4.7 Logarithm of scaling-down factors $\log(k)$ plotted against logarithm of resulting power ratios $\log(x)$ and associated linear regressions for three test cases. 57
4.8 Computed and ground truth scaling-down factors k plotted against power ratio x for three test cases. 58

4.9 Relative difference (in %) between the ground truth values of the scaling-down factor k and the values computed from knowing the power ratio x. 58
4.10 Full-scale and down-scaled power request for $k = 3.96$. 59

A.1 Tuning of the γ factor through the bisection method to achieve charge-sustaining mode with the adaptive strategy with $SOC_{threshold} = 65\%$. 63
A.2 Tuning of the γ factor through the bisection method to achieve charge-sustaining mode with the adaptive strategy with $SOC_{threshold} = 70\%$. 64
A.3 Tuning of the γ factor through the bisection method to achieve charge-sustaining mode with the adaptive strategy with $SOC_{threshold} = 75\%$. 64
A.4 Tuning of the γ factor through the bisection method to achieve charge-sustaining mode with the adaptive strategy with $SOC_{threshold} = 80\%$. 65

Acronyms

BEV battery electric vehicle

CG center of gravity

CS charge sustaining

DC direct current

DP dynamic programming

DIMEAS Dipartimento di Ingegneria Meccanica e Aerospaziale

DOE design of experiment

ECMS Equivalent Consumption Minimization Strategy

EM electric machine

EMS energy management system

FC fuel cell

FCHEV fuel cell hybrid electric vehicle

FCS fuel cell stack

GHG greenhouse gases

HESS hybrid energy storage system

HEV hybrid electric vehicle

HyPM hydrogenic power module

ICE internal combustion engine

LDV light-duty vehicle

LUT look-up table

OEM original equipment manufacturer

OOM order of magnitude

PCC Pearson correlation coefficient

PI proportional-integral

RBC rule-based control

RMS root mean square

SC supercapacitor

SOC state of charge

UDDS Urban Dynamometer Driving Schedule

WLTP Worldwide Harmonized Light Vehicles Test Procedure

Chapter 1

Introduction

Climate change and legislative context

"There is a rapidly closing window of opportunity to secure a livable and sustainable future for all" [1]. As the world is heating up and natural disasters become more frequent and more intense [2], climate change has become a major concern among citizens, companies and policy makers. In particular, the automotive industry is at the forefront of this battle, with transports representing 23% of CO_2 emissions in the world, of which 73.9% are due to road transportation [3], making the pursuit of emission reduction in this sector a significant lever in the fight against climate change. To maintain the world a livable place for current and future generations, evermore stringent GHG emission regulations are being put in place through certification norms or legislation, such as the Corporate Average Fuel Economy (CAFE) norm [4] or European Green Deal [5], with heavy fines for OEMs who overcome the emissions thresholds.
To comply with the law - and offer a better future for us all -, multiple technologies and architectures have been developed and optimized for different applications. Considering that a 46.5% share of road transport emissions is emitted by commercial vehicles [3], the application that will be studied in this thesis is the development and optimization of an alternative powertrain for a light-duty vehicle.

Alternatives to combustion-powered vehicles

Battery Electric Vehicles

Among the greener alternatives to a gasoline- or diesel-powered vehicle is the fully electric vehicle, fitted with a battery powering an electric machine that acts as the sole mechanical actuator. The battery is most often a Li-ion battery [6]. The main advantage of this technology is that it emits no CO_2 emissions in its use phase [7] and, if the electricity used to charge the battery is obtained from low-carbon energy, such as renewable or nuclear energy, the GHG emissions associated to the charging can be very low. However, the main disadvantages are that the driving range is reduced [8] and that, as the vehicle gets heavier, so must the battery in order to provide enough energy to meet the electric machine's power request. To achieve this, more material resources are needed to build the battery, increasing the carbon impact of its fabrication [9]. Moreover, the power request for a heavy

vehicle will be higher than for a lighter one, so the battery will be subjected to higher C-rates, or currents, which has been shown to result in a faster decrease of battery life [10]. In the case of a commercial vehicle as studied in this thesis, the full-electric option is not considered to be pertinent [11].

Hybrid Electric Vehicles

Another alternative to the combustion-powered vehicle that can be more adapted to heavier vehicles is to adopt a hybrid architecture, which present a good compromise between reducing fuel consumption and CO_2 emissions with respect to a combustion vehicle and having a smaller battery with a potentially longer life with respect to a battery electric vehicle [7][8].

Different variants of hybrid electric vehicles exist. The most widely researched and known to the general public is the combination of an internal combustion engine alimented by gasoline or diesel fuel and an electric machine alimented by a battery and possibly the ICE providing mechanical energy to another EM acting as a generator. There are 3 main types of architecture for this kind of HEV:

- Parallel architecture: the ICE and the EM both act as mechanical actuators and are respectively alimented by fuel and the battery. Because the traction power can be provided by either of them, both ICE and EM can be downsized [12]. Moreover, the overall powertrain has a high efficiency [12][13]. However, this architecture calls for a clutch [12] and there is a mechanical connection between the engine and the transmission, which means the ICE can operate at optimal efficiency only under a given set of conditions [12][13][14]. This architecture is most adapted to lighter vehicles, such as passenger cars [12].

- Power split architecture: the ICE can act as a mechanical actuator but can also be paired with an EM acting as a generator charging the battery or directly providing power to the electric machine acting as the mechanical actuator, effectively being able to work in either parallel or series architecture [12]. This allows flexible control [13] and allows the ICE to operate in its maximum efficiency region by controlling the speed of the generator motor [12]. However, the architecture itself is complex and can get very expensive due to its many components, including a planetary gear set, and the overall control strategy is also complex [12]. This architecture is most adapted to lighter vehicles, such as passenger cars [12].

- Series architecture: the electric machine acts as the sole mechanical actuator and the ICE is associated to a second EM to constitute a generator unit. As there is no mechanical connection between the engine and the transmission, the operating points of the former can be placed in its optimal efficiency region [13]. The overall control of the powertrain is also quite simple, as there is only one torque source, the electric machine, which moreover does not require a multigear transmission nor a clutch [12]. The downsides of this architecture are that the overall powertrain has a low efficiency and that the EM acting as mechanical actuator must be sized to meet the maximum power request, which makes the vehicle heavy and expensive [12][13]. This architecture is most adapted to heavier vehicles, such as commercial vehicles [12].

Therefore, the series architecture would be most relevant to the commercial vehicle application studied in this thesis.
Within the series hybrid classification, there are three sub-classifications of architecture, which depend on the sizes of the ICE, the electric generator and the battery. In increasing sizes of the ICE and electric generator and in decreasing size of the battery, the architecture are known as Range Extender, where the ICE is used to recharge the battery a little bit in long-range travel, Load Follower, where the engine sustains the charge of the battery, and Full Performance, which offers the flexibility to increase the efficiency of the engine by choosing its operating points.

Fuel Cell Hybrid Electric Vehicles

However, one major issue of regular HEVs is that they still emit CO_2 emissions during the Tank-To-Wheel phase and are dependent on fossil fuels [7][8], whose finite stocks are decreasing and do not represent a good long-term solution for commercial mobility, in addition to being a major contribution of air pollution which is a significant health hazard to populations [15]. An alternative to using a fossil-fuel-powered engine is to consider a hydrogen-powered fuel cell as the second power source providing power to the battery or electric machine, which is effectively a series architecture as defined above, making it a pertinent use case for heavier, commercial vehicles. It is worth pointing out that, at this stage of development, the production of hydrogen mostly still emits CO_2 gas but not only does a hydrogen-powered vehicle still emit less GHG over its entire life cycle than a vehicle powered by an ICE burning fossil fuels [7], there are hydrogen manufacturing methods emitting no CO_2 that already exist and are becoming more widespread [16].

Supercapacitors as a power buffer

The main issue related to pairing a battery with a fuel cell is that, because of the slow dynamics of the latter, the former has to provide the high-rate power request and therefore experience high C-rates. As previously mentioned, high C-rates tend to damage the battery life and are best avoided [10]. A common solution to this issue is to add supercapacitors in parallel to the battery as an additional power source to the electric machine. Indeed, supercapacitors can withstand an incredibly high amount of charging and discharging cycles [17]. Being a high-power, low-energy source, they are a good complement to batteries, which are high-energy, low-power sources, and are able to spare the battery the higher currents required by the power demand of the electric machine [18]. In practice, supercapacitors are composed of two electrodes facing each other, most often made of carbon [19], separated by a liquid electrolyte. Their very high capacitance C is due to the large surface of the electrodes and the double-layer capacitance due to the electrostatic interaction [18].

Power converter architectures

To connect the power sources together and to the electric machine, DC/DC power converters are often used. For hybrid energy storage system applications

containing a battery and supercapacitors, three main types of configurations are used: passive, semi-active and fully active [20].
In the passive configuration, the supercapacitors and the battery are directly connected in parallel with one another, and a DC/DC converter can be added before the DC bus. The main advantage of this configuration is that it is cheap, having few components. However, this results in the impossibility of implementing control strategies at the converter level and the supercapacitors performance is inherently limited. [20][21]
In the semi-active configuration, the supercapacitors and the battery are separated from each other by a bidirectional DC/DC converter. As for the passive configuration, another DC/DC converter can be added before the DC bus. This configuration allows more flexibility positioning the components. The most commonly used configuration is having the battery directly connected to the DC bus, with no power converter, and the supercapacitors connected to the battery in parallel, separated by a DC/DC converter. It represents a good compromise between control, cost and efficiency but is unable to provide an optimal solution for any of these aspects. [20][21]
Finally, the active configuration, in which two bidirectional DC/DC converters, one for the battery and one for the supercapacitors, are used, offers the best control possibilities. However, said control is very complex and the configuration is expensive due to its elevated number of components. [20][21]

For what concerns fuel cell hybrid electric vehicles, there are many different proposed configurations in the literature, where the fuel cell is systematically in parallel with the battery and supercapacitors [22][23][24][25].

In this thesis, the choice has been made to not modelize DC/DC converters as the focus is on the modeling and control strategies, as opposed to the physical representation of each component.

Energy management strategies

By designing and optimizing energy management strategies that rule the power distribution of one or more components, it is possible to minimize fuel consumption and pollutant emissions while ensuring good drivability [13][14]. There are two levels at which energy management strategies can be considered for hybrid electric vehicles: the powertrain level, where the torque distribution of two or more mechanical actuators is chosen based on their efficiency at a given operating point, and the power source level, where the power distribution between the battery and supercapacitors, for example, is dictated based on SOC concerns and the power demand. Since the fuel cell hybrid architecture, which has only one mechanical actuator, has been chosen for this thesis, the EMS acting at the powertrain level will not be reviewed.

Rule-Based Control Strategy

One of the entry points to energy management strategies is the deterministic rule-based control strategy, which is a heuristic method with pre-defined rules that dictate the power output of one or more power sources. The main advantage

of this strategy is that it is computationally very efficient. However, due to its lack of explicit optimization, it may fail to exploit the full potential of the hybrid architecture. Moreover, it requires a good knowledge and understanding of the system. In the literature, the rule-based control strategy has for instance been used to control the opening and closing of switches that activate or deactivate the links between the electric machine, supercapacitors and battery [21]. Another example of its use is by the authors of [26], who use the strategy to specify the power distribution between a battery and supercapacitors.

Equivalent Consumption Minimization Strategy

Another energy management strategy that is widely used for both torque and power control of HEVs is the Equivalent Consumption Minimization Strategy, or ECMS. It is a local optimization method that minimizes the instantaneous cost and is therefore a sub-optimal solution. In particular, for hybrid electric vehicles, the cost is defined as the equivalent fuel consumption and the control variables are chosen depending on the architecture of the vehicle. Ideally, the ECMS is subject to the charge-sustaining assumption (*i.e.* having the final SOC equal to the initial one), but if that is not ensured, a penalty function on the SOC of the battery can be introduced to penalize extreme charging values. The aforementioned equivalent fuel consumption is defined as the sum of the actual fuel consumption (hydrogen in the case of a FCHEV) and the virtual fuel consumption of the battery. Indeed, while the battery is not directly consuming fuel, discharging phases are followed by charging phases from the other power source, which will induce a further fuel consumption. When it is accounted for in the equivalent fuel consumption computation, it is weighted by an equivalence factor that represents the efficiency of the overall powertrain in charge and discharge conditions. This factor must be computed as a tuning parameter for a given driving cycle. In practice however, computing the virtual fuel consumption of the battery is difficult, as it requires to know in advance at which operating point the other power source will be when charging it. To palliate this issue, the difference in state of charge ΔSOC over the driving cycle is usually considered instead in the formulation of the equivalent fuel consumption. In spite of being a good local optimization technique for a given driving cycle, the ECMS has several drawbacks. First, it is very expensive computationally speaking. Indeed, at each time step of the simulation, the power demand must be computed and a finite number of control candidates must be identified. For each of those candidates, the equivalent fuel consumption must be computed. The optimal candidate is chosen such that it minimizes the equivalent fuel consumption while ensuring physical compatibility with the different components of the vehicle model. Moreover, the value of the equivalent factor that is found is very strongly related to the driving mission, so needs to be recomputed for each new driving cycle considered, and has to be estimated offline. In the literature, the ECMS is notably used by the authors of [27] as the second layer of a 2-layer optimization strategy for determining the power distribution between a fuel cell stack and a battery for a FCHEV equipped with supercapacitors.

Dynamic Programming

An alternative strategy that can be used is the dynamic programming (DP) method. Unlike the ECMS, DP is a global optimization strategy rather than a local one. The optimization process consists in a backward phase and a forward phase. In the backward phase, increasingly long tail sub-problems are iteratively solved with the global cost for each iteration and possible state variable is stored. In the forward phase, the initial state variable is used as a starting point and at each stage the optimal control candidate minimizing the global cost is identified. The main benefit of this EMS is that the optimal solution will surely be found, but this comes at the cost of very long computational times. In the literature, DP is used for instance to dictate the power and thermal management of a hybrid electric vehicle model [28].

There are many other, more complex, energy management strategies that exist [29], such as, but not limited to, Pontryagin's Maximum Principle [26], fuzzy rule-based control strategies [30] and model predictive control [31].

Test bench

To test the validity of a vehicle model and that the control strategies lead to the expected results in real applications, test benches are often used. Most frequently, the benches are a scaled-down version of the vehicle, mainly to keep the costs low. In the literature, for the modeling of a HESS, test benches of scale 1:10 are most often used [32][33]. However, the authors of the studies do not usually explain the methodology of how they scaled down the components of the powertrain and power sources. Several methods exist to scale-down components for hybrid electric vehicles and will be reviewed in depth in the chapter dedicated to the test bench.

Thesis objectives overview

In this thesis, the aims regarding the modelization of the fuel cell hybrid electric vehicle are three-fold. The first goal is to downsize the battery with respect to a regular full electric vehicle. Indeed, this will have a positive impact on many aspects, such as cost, vehicle weight and environmental impact of production. The second goal will be to increase the battery life. Defining battery life is in practice quite hard when dealing with theoretical models with little real-world data, as is the case in this thesis. Therefore, an intermediate Key Performance Indicator (KPI) is chosen to measure quantitatively the impact of the measures that will be introduced, that is to say the C-rates experienced by the battery. The goal will then be to decrease the C-rates experienced by the battery, the quantitative measure of which will be accompanied by a qualitative conclusion on battery life. Finally, the last goal will be to try and decrease the fuel consumption of hydrogen used by the fuel cell stack. The fourth and final goal relates to the test bench and is to find a scaling-down method that allows to scale down one or more components of the vehicle.

In the first chapter of this thesis, the vehicle model, its parameters and the models of its components will be presented. A particular emphasis will be placed on the model of the fuel cell stack as well as the sizing of the battery.

The second chapter will be dedicated to comparing different variants of the architecture, measuring the impact of the different components being introduced as well as the energy management strategies, whose development and tuning will be presented in detail.

The third and final chapter will present a scaling-down strategy for the electric machine of the vehicle in the context of hardware-in-the-loop applications on a scaled-down test bench. Several strategies from the literature will be reviewed. One will be chosen, studied and adapted to be able to obtain the value of a scaling-down factor from the desired rated power ratio for the electric machine.

Chapter 2

Fuel cell hybrid electric vehicle modeling

To study the behavior of a fuel cell hybrid electric vehicle, a model needs to be defined and implemented. The model for the vehicle that will be discussed has been developed in MATLAB SIMULINK. As the work conducted in the context of this thesis has been focused on power sources, the general structure of the model will be succinctly presented before introducing an in-depth description of the chosen architecture and the power sources modeling.

2.1 General structure of the vehicle model

The vehicle studied is based on the LDV IVECO eDAILY Fuel Cell Electric Vehicle [34] and IVECO Daily [35]. Its characteristics are defined in table 2.1.

Characteristic	Notation	Unit	Value
Mass	M	kg	4200
Mass for battery sizing	M_{max}	kg	7000
Distance from CG to front axle	a	m	1.4165
Distance from CG to rear axle	b	m	1.8835
CG height above ground	h	m	1.2
Frontal area	A_f	m^2	4.5808
Drag coefficient	C_d	-	0.316
Air density	ρ	$kg.m^{-3}$	1.21
Rolling radius	r	m	0.35

Table 2.1: Vehicle and environment characteristics.

The vehicle model studied in this thesis is a forward model and is presented on figure 2.1. The forward architecture has been chosen as opposed to a backward architecture. Indeed, the forward architecture is much more relevant in the context of component evaluation as it outputs the predicted future state of the model from the current state and the control inputs, whereas the backward architecture computes the control inputs required to reach a desired future state from the current state. Moreover, the architecture allows to obtain results more representative of

what would happen in real life because it allows the implementation of a driver model as the actuator.

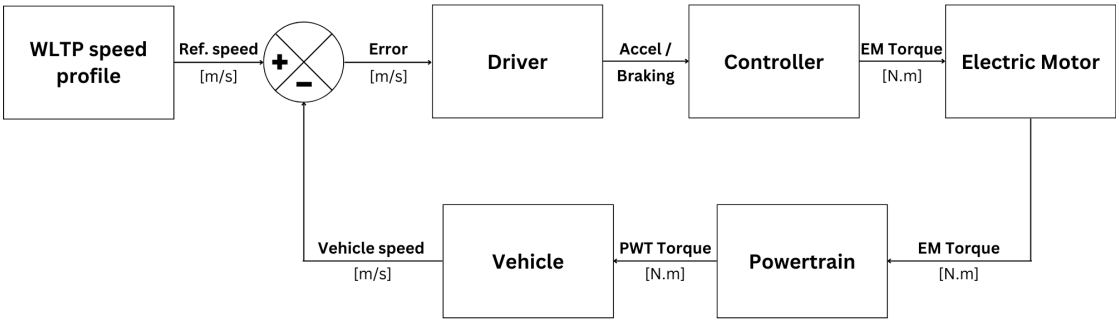

Figure 2.1: General structure of the forward vehicle model.

In Simulink, the model is divided in two major components, the controller and the plant, whose inputs and outputs are presented in figure 2.2.

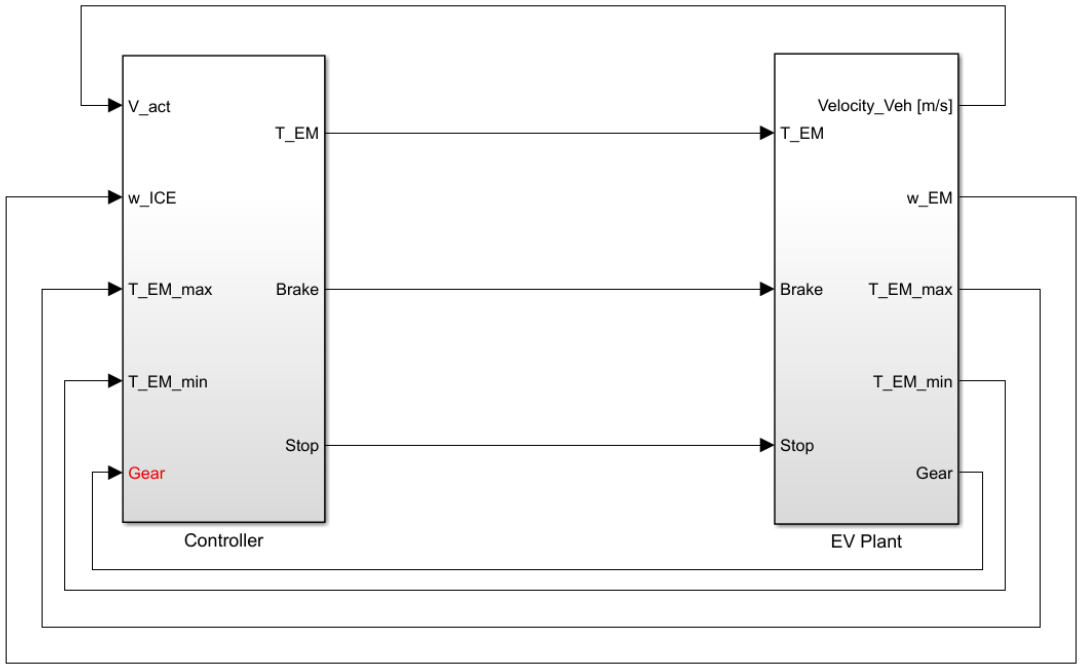

Figure 2.2: Root structure of the Simulink model.

In the controller (*cf.* fig. 2.3), the speed profile from the WLTP cycle is generated. It is a 23.25 kilometer-long standardized cycle that last 1800 seconds and is composed of an urban portion (from 0s to 600s), an extra-urban section (from 600s to 1000s), a rural portion (from 1000s to 1450s) and a highway scenario (from 1450s to 1800s). It is used in Europe as the sole vehicle homologation procedure since 2021, replacing the New European Driving Cycle (NEDC), which was deemed to be not representative enough of the reality, especially for what concerned fuel consumption and pollutant emissions.
A PI controller representing the driver translates the error between the target speed profile and the actual one into a throttle or brake normalized command. The proportional gain of the controller has been tuned to obtain a "reactive" driver.

For a heavier vehicle, it means increasing its value. The throttle/brake command output from the driver is then translated to a torque request based on the EM and brake characteristics. The controller outputs the torque and brake request and sends them to the plant.

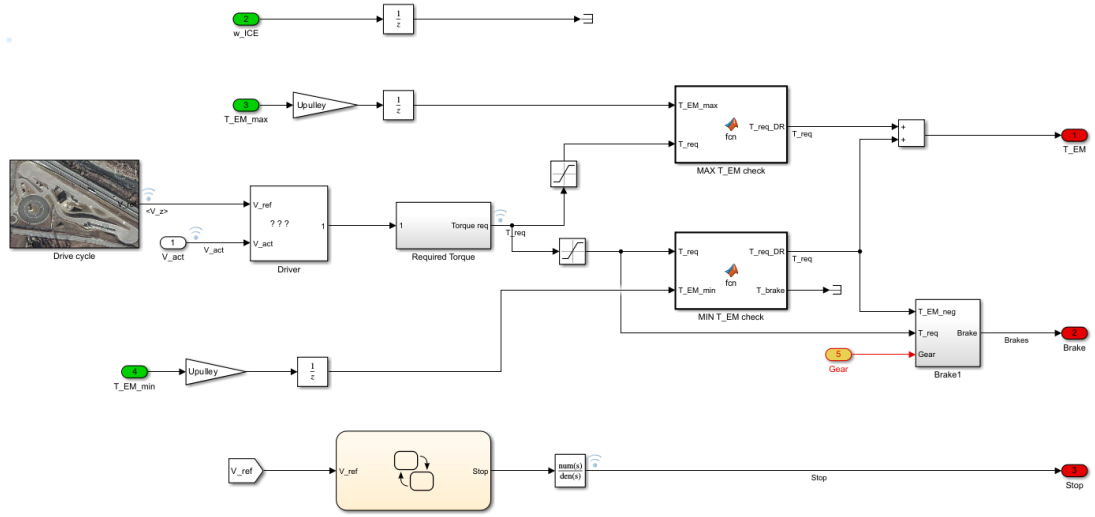

Figure 2.3: Structure of the controller.

The plant (*cf.* fig. 2.4) contains a modeling of the vehicle longitudinal dynamics which determines the actual speed of the vehicle as well as the tire forces and horizontal motion. Those are fed to the modeling of the tires also present in the plant. Finally, the plant contains the models of the EM and of the power sources.

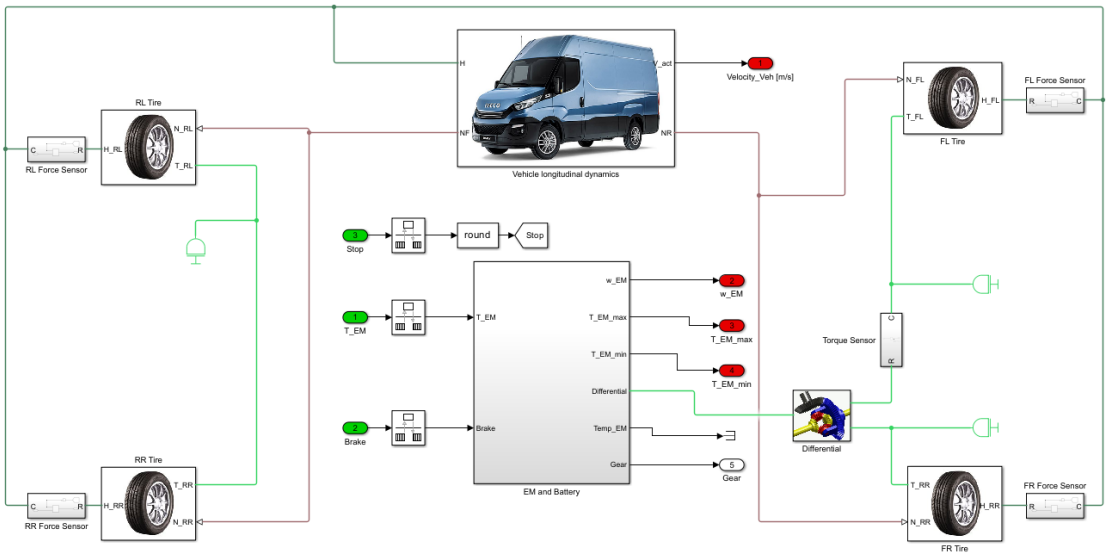

Figure 2.4: Structure of the plant.

The electric machine's model is based on a torque-speed map (*cf.* fig. 2.5) of a 345V, 350N.m machine that has been stretched along the torque axis to reach the 140kW power rating of the IVECO eDaily Fuel Cell Electric Vehicle from the map's initial 80kW rating [34].

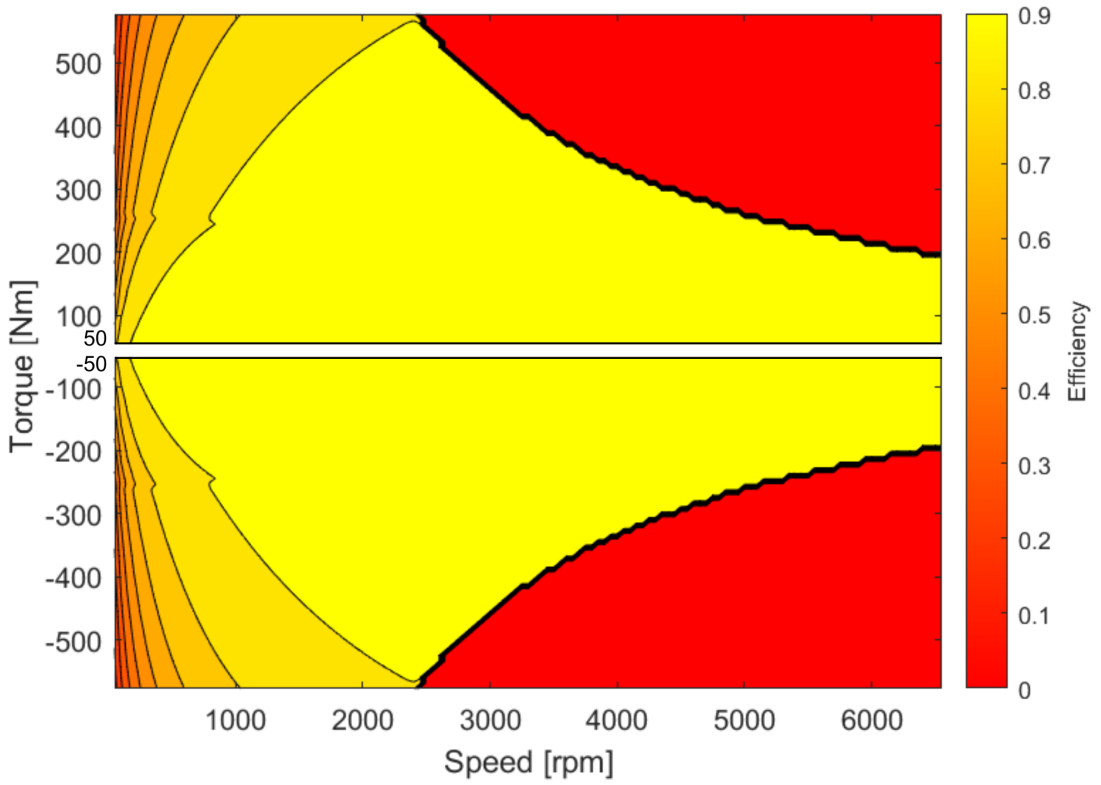

Figure 2.5: Torque-speed map of the electric machine.

The electric machine model generates a power request based on this LUT that is fed to the power sources block, which is detailed in figure 2.8. Additionally, the energy consumption in kWh/100km linked to the power request is computed.
One important thing to note about this model is that the power sources do not influence the power fed to the EM. Indeed, it has been decided to consider that the power request is always met at the EM level to allow the study of the power sources independently.

2.2 Architecture

The FCHEV is considered a hybrid vehicle as it has at least two power sources, the fuel cell stack and the battery, to which can be added a supercapacitor cells stack. As it has only one mechanical actuator, the electric machine, it is technically a series hybrid vehicle according to the Beretta method [36]. However, to distinguish between different powertrain architectures at the power source level, the terms defined by the Beretta method will not be used. In this thesis, two powertrain architectures were considered for the FCHEV, the so-called "parallel" and "series" architectures, referring to the position of the fuel cell stack with respect to the battery.

2.2.1 Parallel

The first architecture that was considered is the so-called "parallel" architecture, where the fuel cell and the battery can both directly provide power to the EM. The

supercapacitors are placed in parallel with the battery and are used to provide and absorb the high-rate power requests.

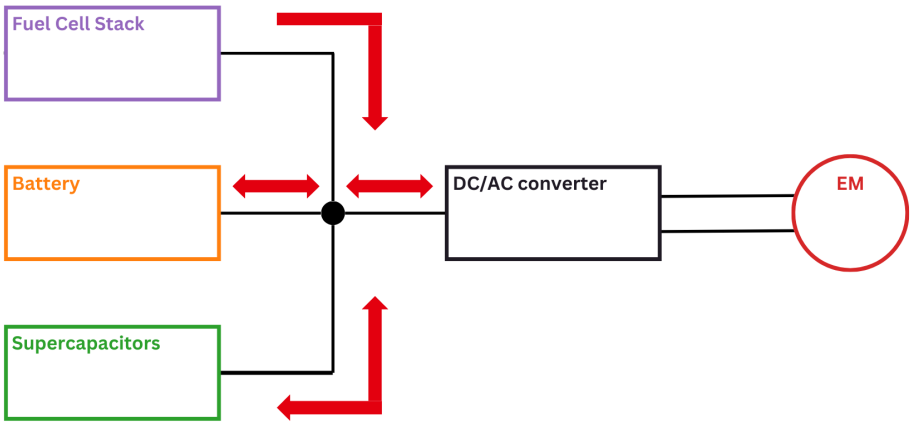

Figure 2.6: Concept of the "parallel" architecture.

This approach is based on the paper by Fu et al. [27], where a two-layer energy management strategy has been chosen, whereby the higher layer dictates the power taken on by the supercapacitors and the lower layer manages the power distribution between the fuel cell stack and the battery. Unlike the authors of the paper, which develop a low-pass filter, a simpler RBC approach could been chosen to manage the power sent to the supercapacitors. For the power distribution between the FCS and the battery, it is handled by an ECMS.

As explained in the introduction, it is a local optimization strategy which minimizes the equivalent fuel consumption of a hybrid vehicle. The equivalent fuel consumption of the vehicle is computed by considering the direct fuel consumption of the fuel cell (in this case) and the virtual fuel consumption of the battery that represents the energy the fuel cell will deploy to charge the battery later on to achieve charge sustaining mode (*i.e.* where the final SOC of the battery is equal to the initial SOC). It is an excellent strategy to minimize the fuel consumption for a specific driving cycle, which here would be pertinent as only the WLTP is considered, even if it might not lead to the most optimal solution as it is not a global optimization method. However, the main con of this method is that it requires to run a bisection algorithm for an unknown, but potentially high (OOM: 10^2), number n of values of the equivalent factor until the optimal one is found, which involves running the entire simulation for $t = 1600 \times 5\text{e} - 3 = 3.2\text{e}5$ time steps, at each of which the ECMS algorithm runs for a number of a (OOM: 10^1) values of the control candidate variable, which results in a computational complexity of $n \times t \times a = 10^2 \times 10^5 \times 10^1 = 10^8$ steps over the entire process. This is already incredibly high on its own, even more so when considering the complexity of the Simulink model which makes the duration of each time step quite long by itself.

2.2.2 Series

The second architecture that was considered is the so-called "series" architecture, where the FCS directly charges the battery, which provides power to the EM. The supercapacitors are still placed in parallel with the battery to provide and absorb

the high-rate power requests.

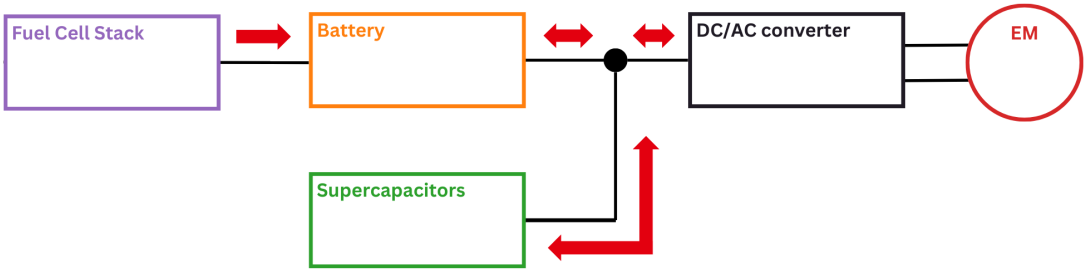

Figure 2.7: Concept of the "series" architecture.

This approach is developed by Bubna et al. in [37], where a fuel cell/battery series-hybrid bus has been developed. Theirs is a Range Extender, with a large battery and a small FCS.
In this thesis, as one of the objectives is to downsize the battery, a hybridization level closer to the Load Follower would be more pertinent, with the ultimate goal being to attain a charge-sustaining working mode for the battery.
This architecture presents the advantage of avoiding high-rate power requests from the FCS through continuous power being provided to the battery, palliating the slow dynamics of the fuel cell and reducing the C-rates it experiences, therefore prolonging the battery life.

Because the "series" architecture is much simpler computationally speaking and because a similar approach has been adopted in the literature, it has been chosen over the "parallel" one and will be the only one further explored in this thesis.

2.3 Power sources modeling

The modeling of the power sources, namely the battery, the supercapacitors and the fuel cell stack, are presented in the following section.

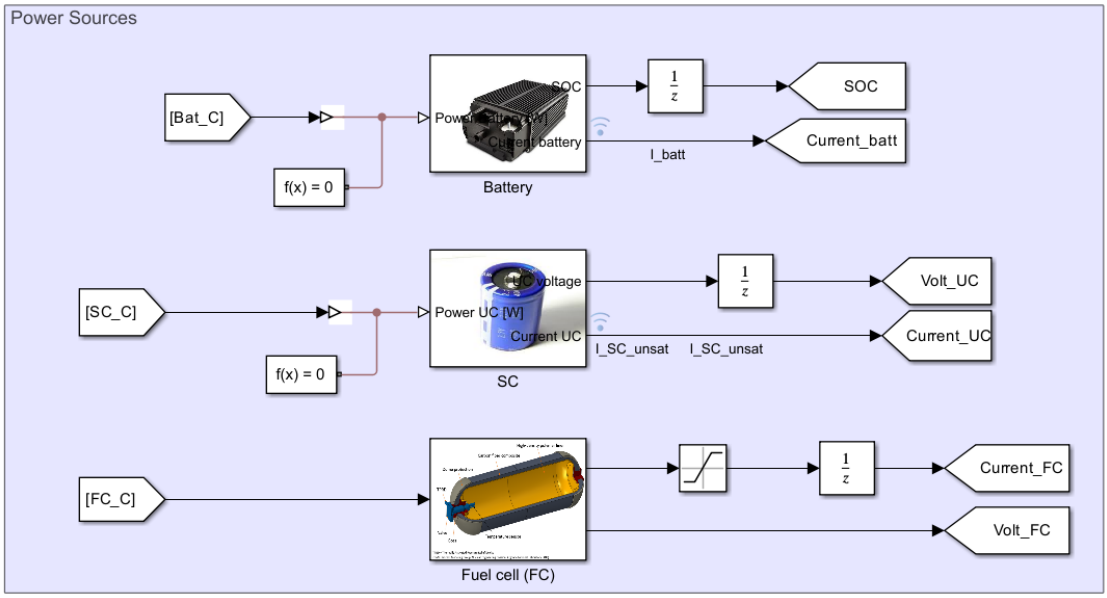

Figure 2.8: Structure of the power sources.

2.3.1 Battery

The battery characteristics have been chosen based on the electric machine and on its capability to sustain the power request on the WLTP cycle with the fuel cell stack present but not the supercapacitors.
To match the electric machine's rated voltage, the battery rated voltage $U_{batt,r}$ has been set to 345V. Its maximal current $I_{batt,max}$ has been computed as follows:

$$I_{batt,max} = \frac{P_{EM,max}}{U_{batt,r}} = \frac{140.10^3}{345} = 405.8A$$

The battery capacity C_{batt} has been sized considering the vehicle mass $M_{max} = 7000$kg as defined in table 2.1 to modelize a fully loaded vehicle.
The power request with such a vehicle mass is represented on figure 2.9.

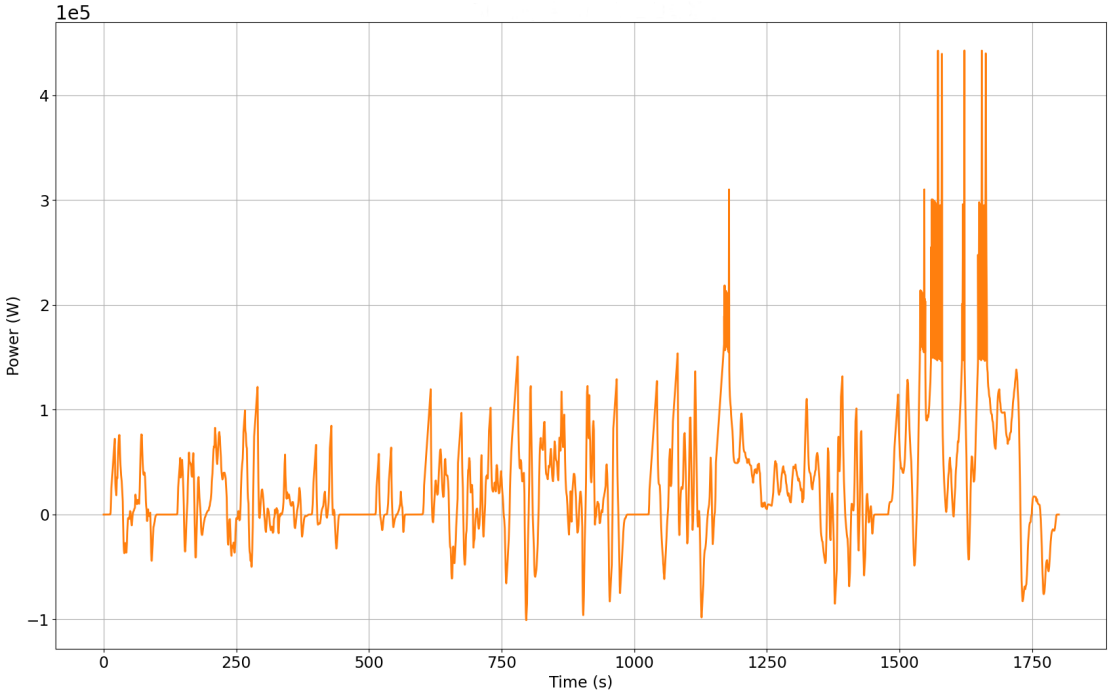

Figure 2.9: Power request along the WLTP for the 7000kg vehicle.

A DOE has been conducted on 10 different values of battery capacities, computed for C-rate values from 1C to 10C such that:

$$C_{batt} = \frac{I_{batt,max}}{\text{C rate}}$$

C-rate (h^{-1})	1	2	3	4	5	6	7	8	9	10
Capacity C_{batt} (A.h)	405.8	202.9	135.3	101.4	81.2	67.6	58.0	50.7	45.1	40.6

Table 2.2: Values of C_{batt} and associated C-rates used for the DOE.

The battery capacity must be a compromise between being high enough to meet the power request, and to avoid deep charges and discharges in order to preserve battery life, and being low enough to limit the battery's weight, its volume and the resources necessary to build it.
The first thing to do is to ensure that the battery is meeting the power request. To do so, one must make sure that the SOC of the battery does not goes to 0. As can be seen in figure 2.10, all configurations meet the power requirement as the battery never becomes fully depleted. It can be interesting to look at how the battery would fare should the fuel cell not be present, to modelize an empty tank for instance.
The results of this analysis are presented on figure 2.11. It can be seen that batteries with a capacity lower than 81.2A.h cannot deliver the requested power without the FCS being present. Because misuse of the vehicle by the user is a possibility and to let them reach the next refuelling station, these battery capacities will not be considered any further for the battery sizing.

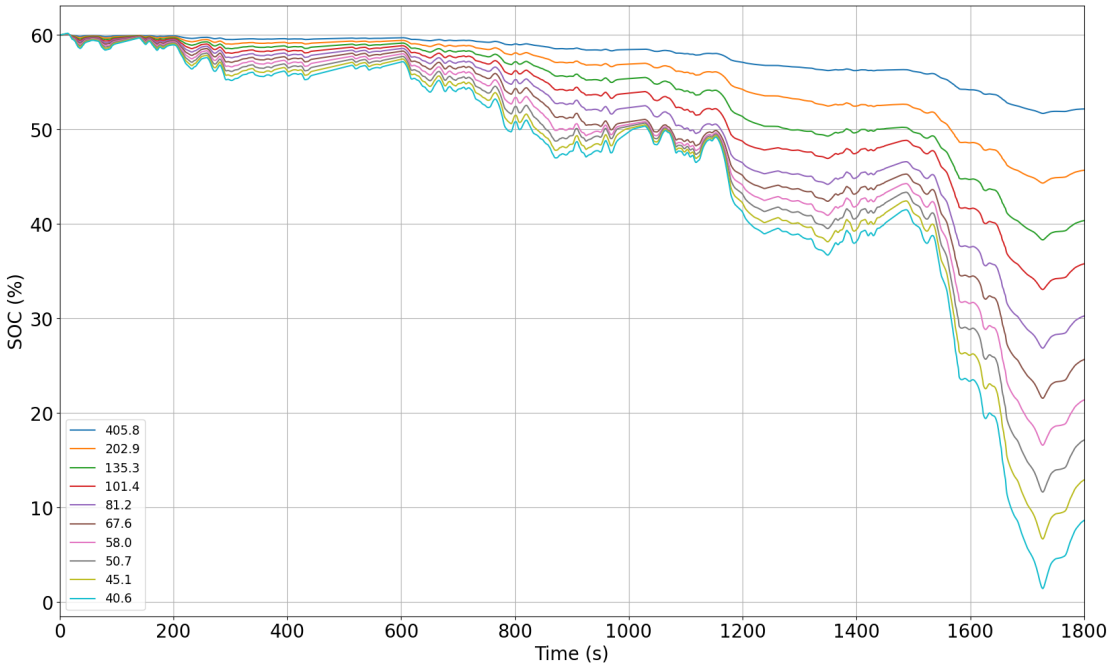

Figure 2.10: Evolution of the SOC of the battery for the DOE on battery capacity. *The legend corresponds to the value (in A.h) of C_{batt} being tested.*

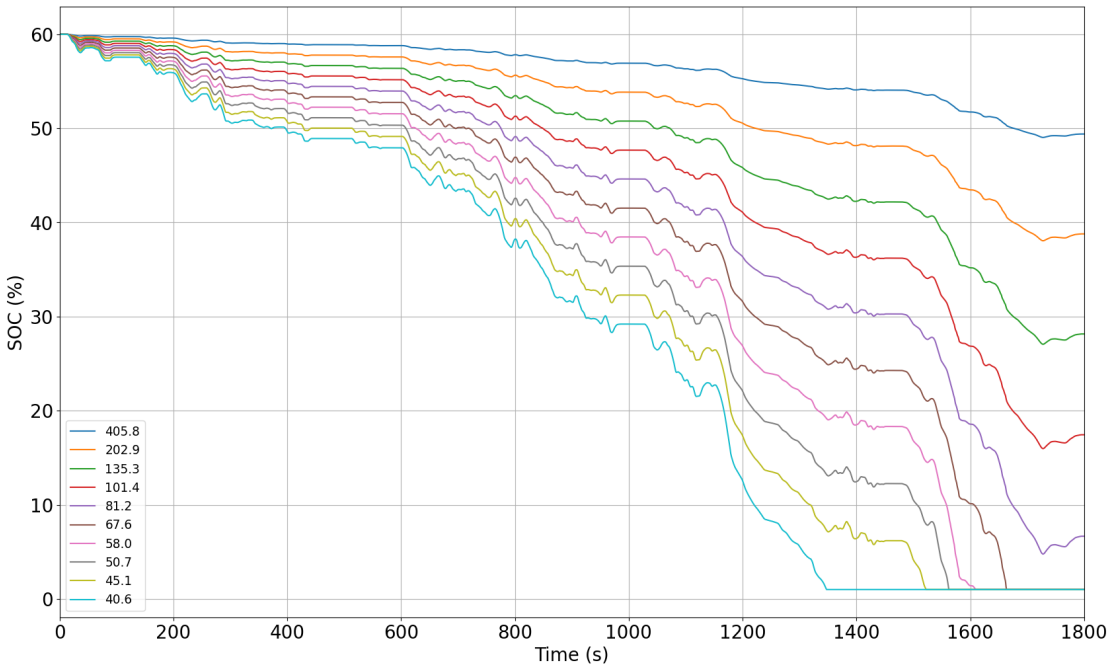

Figure 2.11: Evolution of the SOC of the battery without the fuel cell stack for the DOE on battery capacity.
The legend corresponds to the value (in A.h) of C_{batt} being tested.

The evolution of the battery SOC and C-rates, presented respectively in figures 2.12 and 2.13, are considered. As the superposing lines can make it hard to read the plots, the relevant information has been extracted and plotted as a function of battery capacity in figures 2.14 and 2.15.

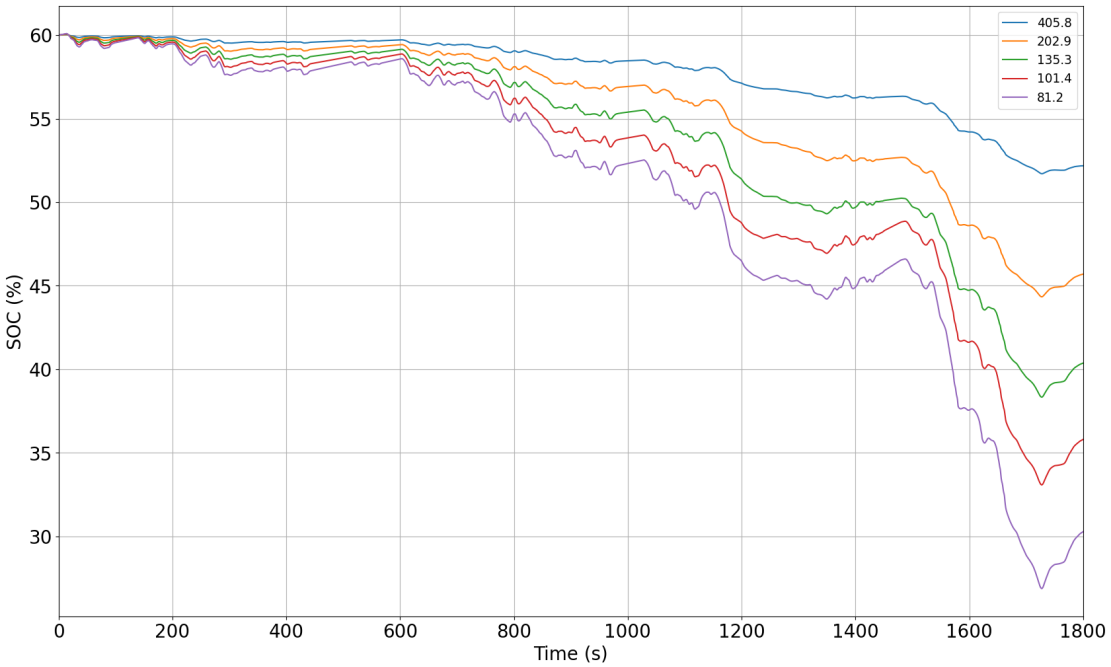

Figure 2.12: Evolution of the battery SOC for the DOE on battery capacity. *The legend corresponds to the value (in A.h) of C_{batt} being tested.*

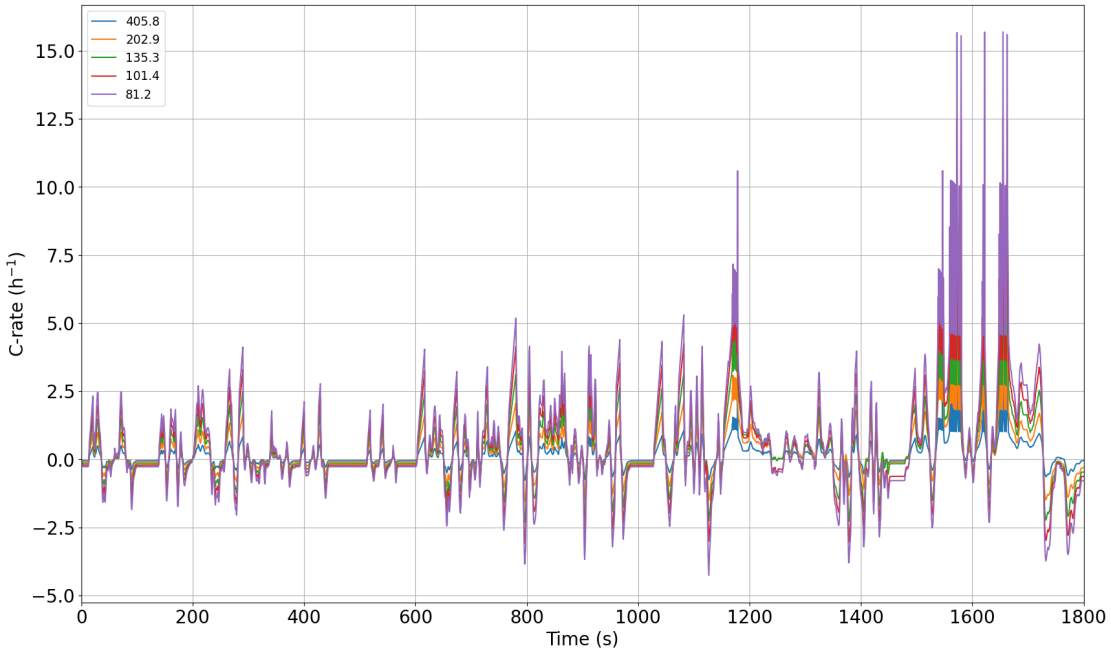

Figure 2.13: Evolution of the battery C-rate for the DOE on battery capacity. *The legend corresponds to the value (in A.h) of C_{batt} being tested.*

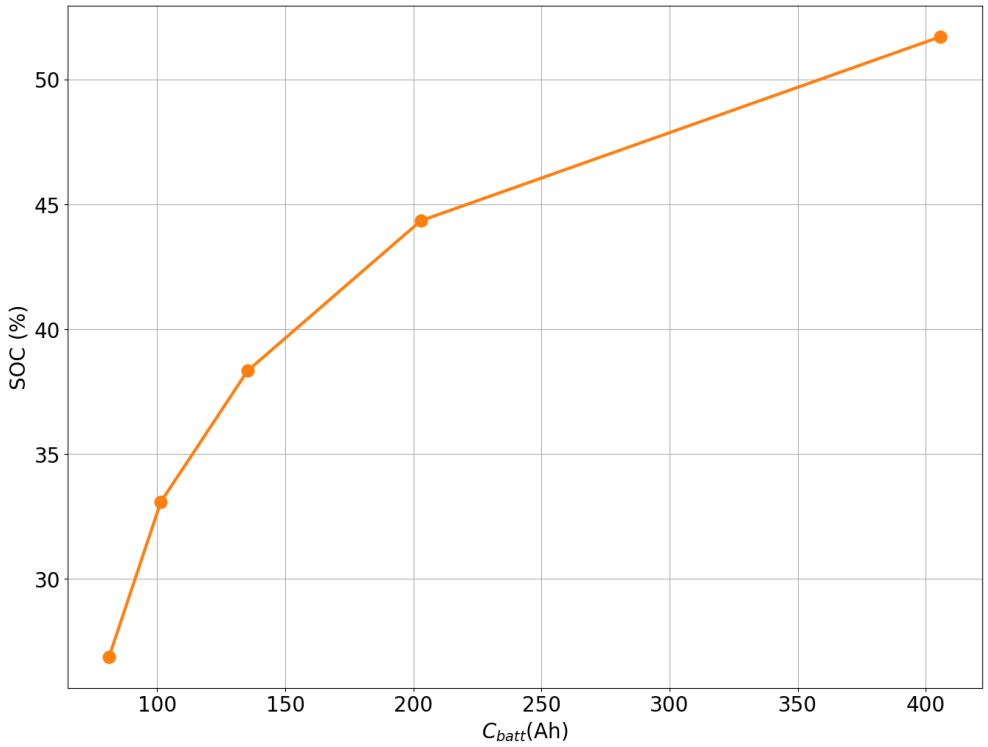

Figure 2.14: Minimum SOC reached during the WLTP cycle as a function of C_{batt}.

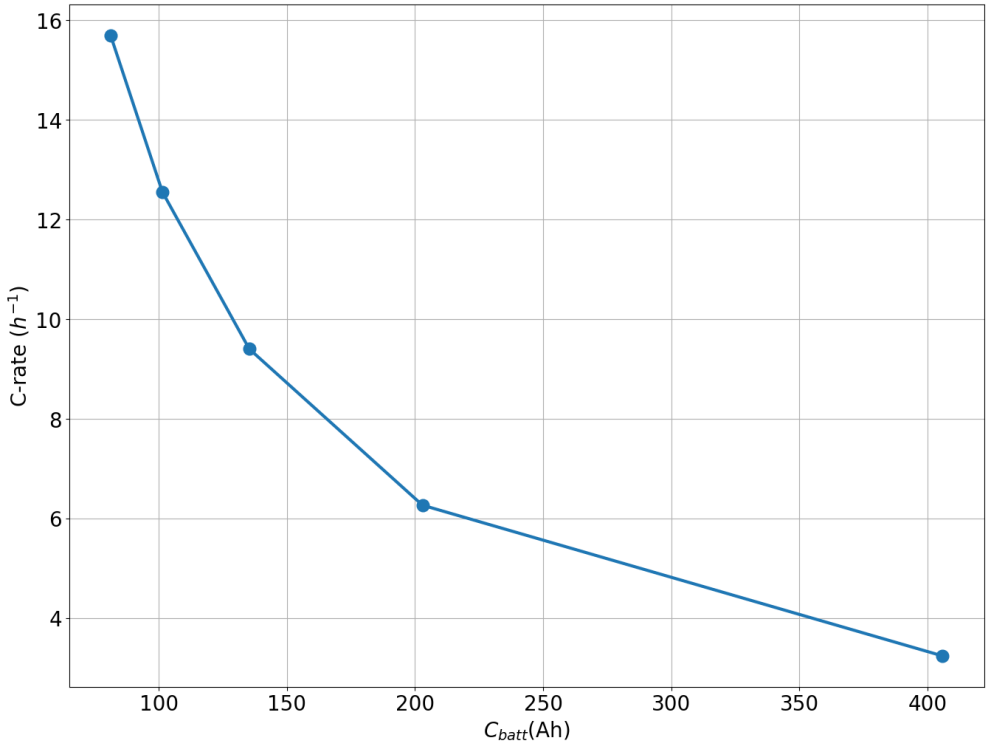

Figure 2.15: Maximum C-rate reached during the WLTP cycle as a function of C_{batt}.

To quantify how easily near-charge-sustaining conditions can be reached, the

minimum SOC value reached by the battery during the WLTP cycle (*cf.* fig. 2.14) for each battery capacity value is considered and the difference from the initial SOC value of 60% is computed. As shown by table 2.3, battery capacities of 101.4A.h and 81.2A.h result in a drop quasi equivalent to halving the initial SOC of the battery, which is not deemed optimal with respect to the objective of having a hybridization level close to Load Follower.

Capacity (A.h)	**SOC variation (%)**
405.8	-14
202.9	-26
135.3	-36
101.4	-45
81.2	-55

Table 2.3: Variation from initial value of SOC to minimal SOC value.

For what concerns the C-rates experienced by the battery during the cycle, figure 2.13 clearly shows that, as expected, the C-rates increase with decreasing battery capacities. The plot on figure 2.15 in particular highlights the maximum C-rate value as a function of battery capacity. With the 135.3A.h battery, an acceptable 10C C-rate is reached and choosing it over the bigger capacities would limit the weight, size and environmental impact of the battery and, consequently, of the overall vehicle. Such a battery capacity corresponds to an energy of 47kWh, which is in line with the OOM of the modular battery concept used for the IVECO eDaily, between 37kWh and 111kWh [38].

The battery is modelized as an ideal voltage source whose Simulink model has not been studied in the context of this thesis and has been retrieved from previous works within the DIMEAS at Politecnico di Torino. Figure 2.16 shows how the battery has been modeled in Simulink.

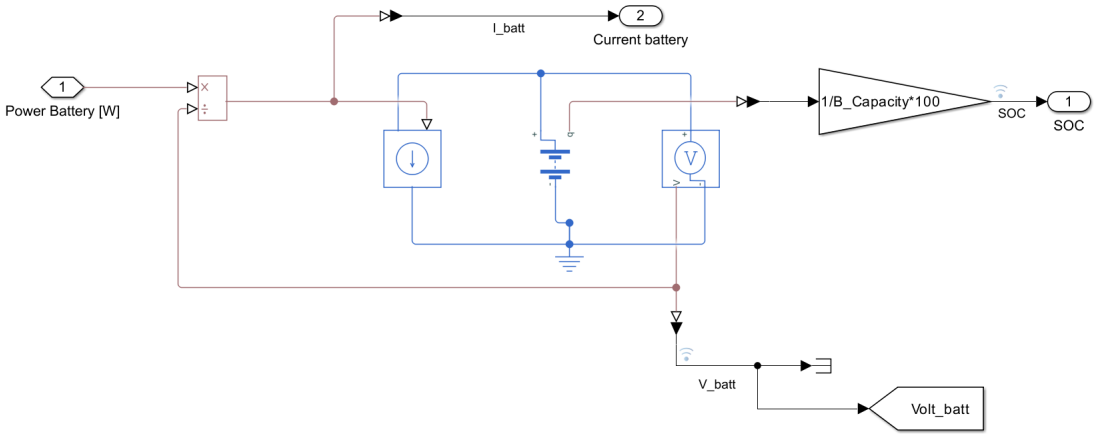

Figure 2.16: Block architecture of the battery model in Simulink.

2.3.2 Supercapacitors

The supercapacitors cell being modelized is Maxwell's 2.7V 3000F Ultracapacitor Cell of model number BCAP3000 P270 K04/05. It presents the following main characteristics:

Parameter	Unit	Value
Rated voltage	V	2.7
Max. rated capacitance	F	3600
Peak current	A	2300
Continuous current	A	280

Table 2.4: Characteristics of the Maxwell 2.7V 3000F Ultracapacitor Cell

For the application at hand, 128 cells are placed in series to reach a voltage of 345.6V, which is almost equal to the rated voltage of the battery. Only one row of cells in parallel is considered.
The supercapacitors have been modeled using the Zubieta model, which provides results of acceptable [39] and similar [40] accuracy as the Stern-Tafel model, which are the two most common models for supercapacitors. It is based on the concept of fixed capacities and resistances [39][40][41]. The characteristics of the chosen SC cell have been determined experimentally by [42] and have been adopted in this work. They are presented in table 2.5.

Characteristic	Unit	Value
Fixed Resistances (R1, R2, R3)	Ω	0.32232e-3
		0.38065
		1.3284
Fixed Capacitances (C1, C2, C3)	F	2934.7
		76.841
		1518.8
Voltage-dependent capacitor gain	F/V	130.81
Self-discharge resistance	Ω	59436

Table 2.5: Cell characteristics for the Zubieta model.

Figure 2.17 shows how the supercapacitors have been modeled in Simulink.

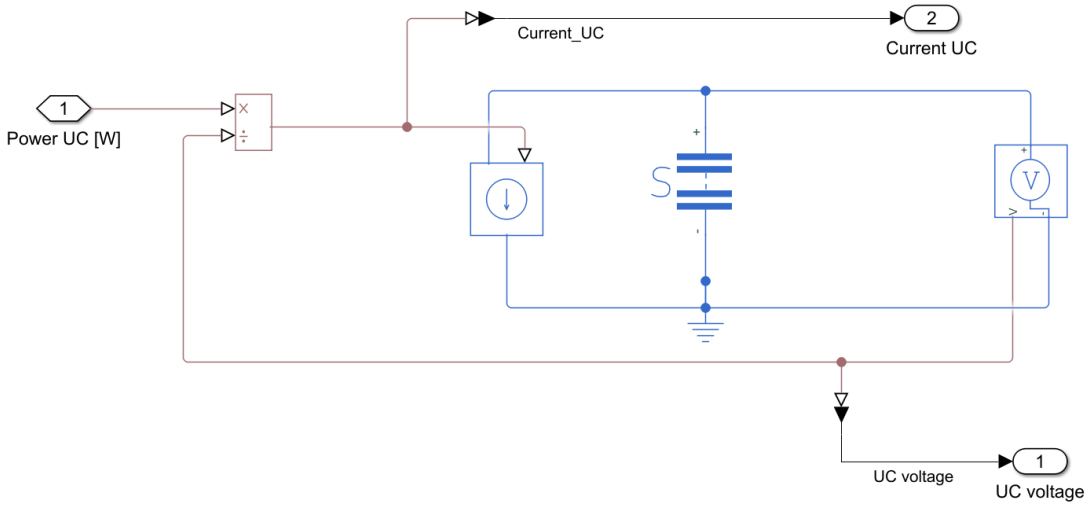

Figure 2.17: Block architecture of the supercapacitors model in Simulink.

2.3.3 Fuel cell stack

The fuel cell stack has been dimensioned as having a maximum voltage of 345V, to match that of the EM and the battery, and a maximum current of 100A to be in line with the order of magnitude defined by the literature while maintaining a small-enough size for the application at hand [37][43].

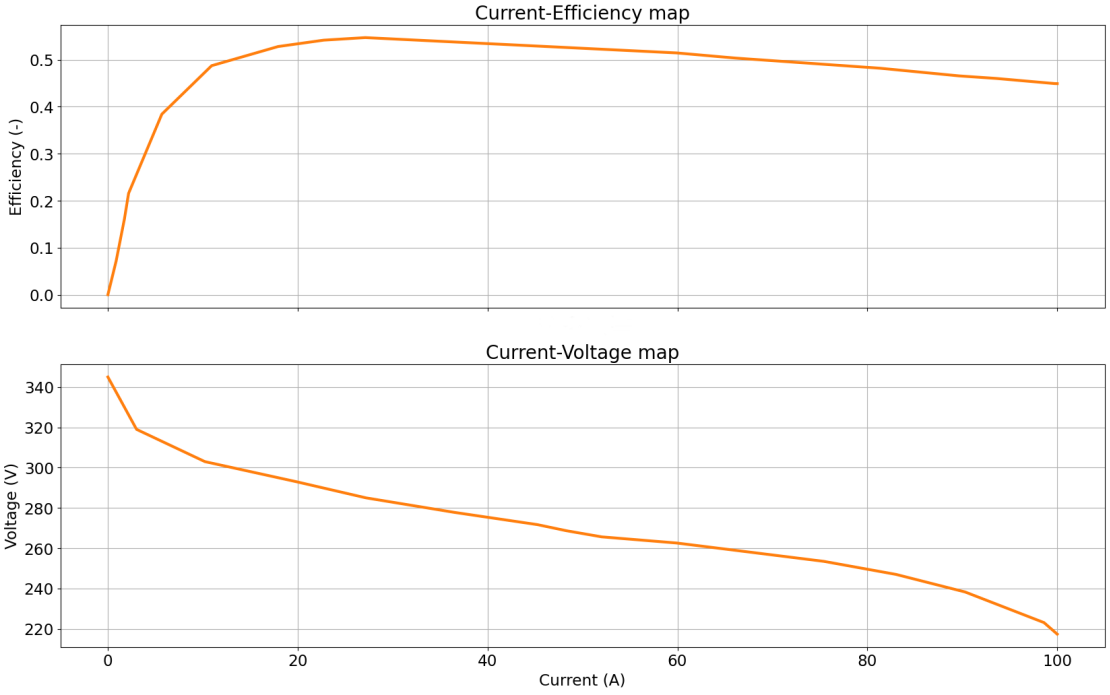

Figure 2.18: Look-up tables used for modelizing the fuel cell stack.

As for the Simulink model of the fuel cell stack, it is based on two look-up tables representing the current-efficiency and current-voltage characteristics of a HyPM fuel cell [44]. These specific LUTs have been chosen because they represent the characteristics as a percentage of the maximum current and voltage, which makes

them easily scalable to any application. The scaled maps are presented in figure 2.18.
However, it is important to keep in mind that for automotive applications, HyPM fuel cells are often not used [45] and the modeling of the fuel cell stack should reflect that. For the current application, which is mainly focused on developing energy management strategies and getting a broad understanding of the impact of a fuel cell stack on the battery, the HyPM model is deemed suitable enough.
The Simulink model of the FCS presented in figure 2.19 takes as input the power command and outputs its current and voltage, the latter being computed from the aforementioned LUT. The current-efficiency LUT is introduced at the energy management level.

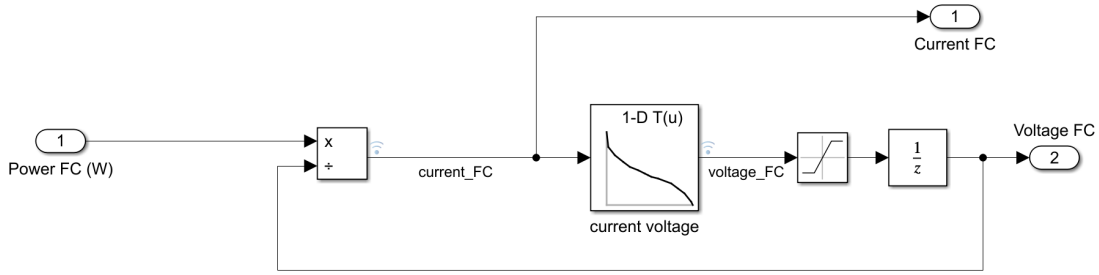

Figure 2.19: Structure of the fuel cell stack model.

One limit of this model, however, is that it does not account for the poor dynamics of the fuel cell [46], which are due to different types of losses, namely activation, ohmic and concentration losses, which are more or less significant as the load changes. The time constant τ in a first-order low-pass filter accounting for the slow dynamics of the fuel cell is defined by the authors of [47] as:

$$\tau = CR_a = \frac{C(V_{act} + V_{con})}{i - i_c} \tag{2.1}$$

with V_{act} and V_{con} respectively the voltage activation and concentration losses, and i and i_C the load and capacitor currents. In order to compute this time constant, which is a function of the FC current, the electrochemical characteristics of the fuel cell must be known, which is not the case here.
To palliate this lack of knowledge while reflecting, even if only roughly, the slow dynamics of the power delivery by the fuel cell stack, a first-order transfer function of unit gain has been introduced in the Simulink model at the power level. This transfer function has a fixed time constant τ.
Its value has been chosen based on the available literature on the matter. The authors of [47] present results for a fuel cell that has a rated voltage of 18.5V and a maximum current of 85A and they find that τ has an OOM of 10^{-1} second.
To reflect the fact that the fuel cell considered in this thesis has a much higher rated voltage (about 19 times, *i.e.* one OOM higher) and to be on the safer side by considering a slower response, the time constant has been set to 1, to be one OOM higher than that presented in the paper. It is also relevant to note that, since a "series" architecture has been adopted where the fuel cell stack constantly charges the battery, the dynamics of the fuel cell are not of significant relevance for the

overall behavior of the powertrain.
Another limit of the fuel cell stack model is that it does not implement a physical limit on the current and/or voltage it can reach.

Chapter 3

Simulation, analysis and comparison of different vehicle models

As previously stated, the goal of this thesis is to develop a model for a fuel cell hybrid electric vehicle in order to downsize the battery and extend its life. To verify that these goals are achieved and to try to optimize the results, the following models will be defined and compared:

- battery electric vehicle model;
- FCHEV model with rule-based control strategy and without supercapacitors;
- FCHEV model with rule-based control strategy and with supercapacitors;
- FCHEV model with adaptive strategy and with supercapacitors.

In particular, the BEV model is computed in Simulink by directing the power request from the electric machine directly to the battery and removing its link with the fuel cell stack.

3.1 Analysis of fuel cell stack addition impact

3.1.1 Rule-Based Control strategy for the power delivery by the fuel cell stack

The first idea for the energy management strategy of the fuel cell stack is to develop a rule-based control strategy to provide continuous power to the battery when it needs it and to optimize the operating points of the FCS.
In this strategy, visually described on figure 3.1, the fuel cell stack has two working modes:

- at maximum efficiency: when the battery is considered to be charged enough as to not need maximum power (SOC between 0.5 and 0.7), the operating point is chosen as to maximize the efficiency of the FCS.

- at maximum power: when the battery is considered to be not charged enough (SOC strictly below 0.5), the operating point is chosen as to maximize the power of the fuel cell stack.

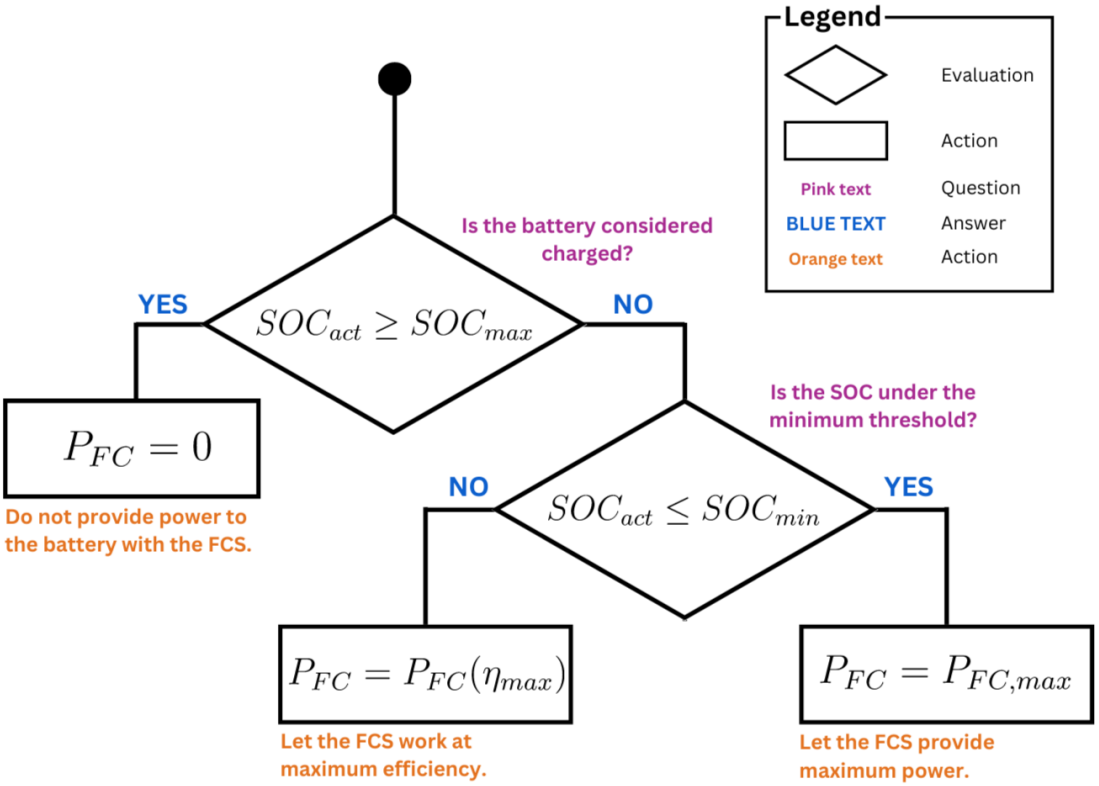

Figure 3.1: Diagram of the RBC algorithm for the fuel cell stack.

In order to compute the power commands associated to the aforementioned working modes, the maps shown in figure 2.18 are exploited. In particular, the voltage-current map is used in combination with the efficiency-current one to obtain the efficiency-power map of the fuel cell stack. The operating points for both working modes are represented on figure 3.2.
This strategy is implemented in Simulink using a Matlab Function block, whose code is defined in listing 3.1. It takes as input at every time step the SOC of the battery and the voltage of the fuel cell stack, as well as the constant currents and efficiencies associated to the two working modes described above, which are computed offline in the Matlab Workspace, and the maximum and minimum thresholds of the SOC, which are set to 70% and 50% respectively, in order to obtain a behavior close to charge sustaining mode.

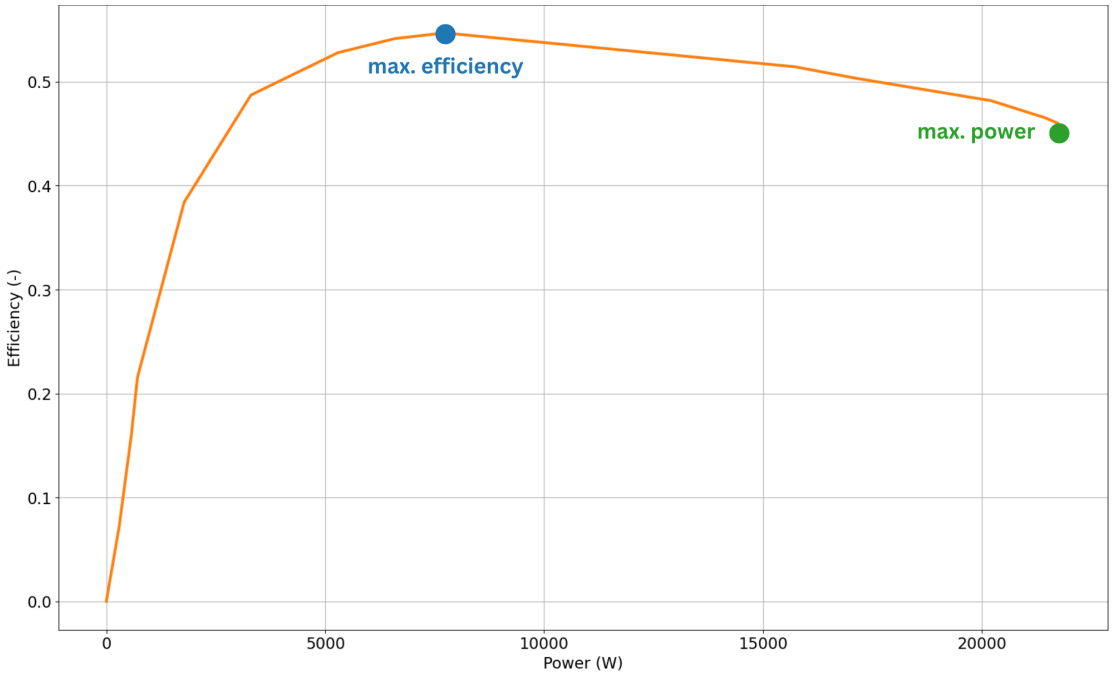

Figure 3.2: Operating points for the rule-based control strategy of the fuel cell stack.

```
function [P_FC, I_FC_command, eta_FC_command] = RBC_FC(SOC_act,
    SOC_min, SOC_max, V_FC, FC_max_eta, FC_max_abs)
    % RBC_FC: Rule-Based Control for Fuel Cell Power Attribution
    %   This function determines the power to be attributed to a fuel
     cell based on a rule-based control approach.
    % Inputs:
    %   - SOC_act: Actual state of charge of the system (%)
    %   - SOC_min: Minimum state of charge threshold (%)
    %   - V_FC: Fuel cell voltage (V)
    %   - FC_max_eta: [Fuel cell current (A), efficiency (-)] at high
     efficiency
    %   - FC_max_abs: [Fuel cell current (A), efficiency (-)] at max
    power
    % Outputs:
    %   - P_FC: Power to be attributed to the fuel cell (W)
    %   - I_FC_command: Current command of the FCS (A)
    %   - eta_FC_command: Efficiency of the FCS associated to the
    current command (-)

    % Max efficiency
    I_FC_max_eta = FC_max_eta(1);
    eta_FC_max = FC_max_eta(2);
    % Max power
    I_FC_max_abs = FC_max_abs(1);
    eta_FC_abs = FC_max_abs(2);

    if SOC_act >= SOC_min && SOC_act <= SOC_max
        P_FC = V_FC * I_FC_max_eta;
        I_FC_command = I_FC_max_eta;
        eta_FC_command = eta_FC_max;
    elseif SOC_act < SOC_min
        P_FC = V_FC * I_FC_max_abs;
```

```
28            I_FC_command = I_FC_max_abs;
29            eta_FC_command = eta_FC_abs;
30        else
31            P_FC = 0;
32            I_FC_command = 0;
33            eta_FC_command = 0;
34        end
35    end
```

Listing 3.1: Coded algorithm of the RBC for the fuel cell stack

The results of the simulation ran with this algorithm are presented in figure 3.3, with notably a cumulative fuel consumption for the fuel cell stack of 0.25kg over the full WLTP cycle. This represents a 1.08kg/100km fuel consumption, an order of magnitude in line with other hydrogen-powered vehicles, such as the Toyota Mirai, a passenger car, which has a fuel consumption that ranges between 0.79kg/100km and 0.89kg/100km depending on the specifications [48].
It can be seen that the logic works properly, as the current command goes from maximum efficiency working mode to maximum power delivery when the SOC of the battery goes under the minimum threshold of 50%. It can also be noticed that the state of charge of the battery actually never goes above the maximum threshold of 70%.

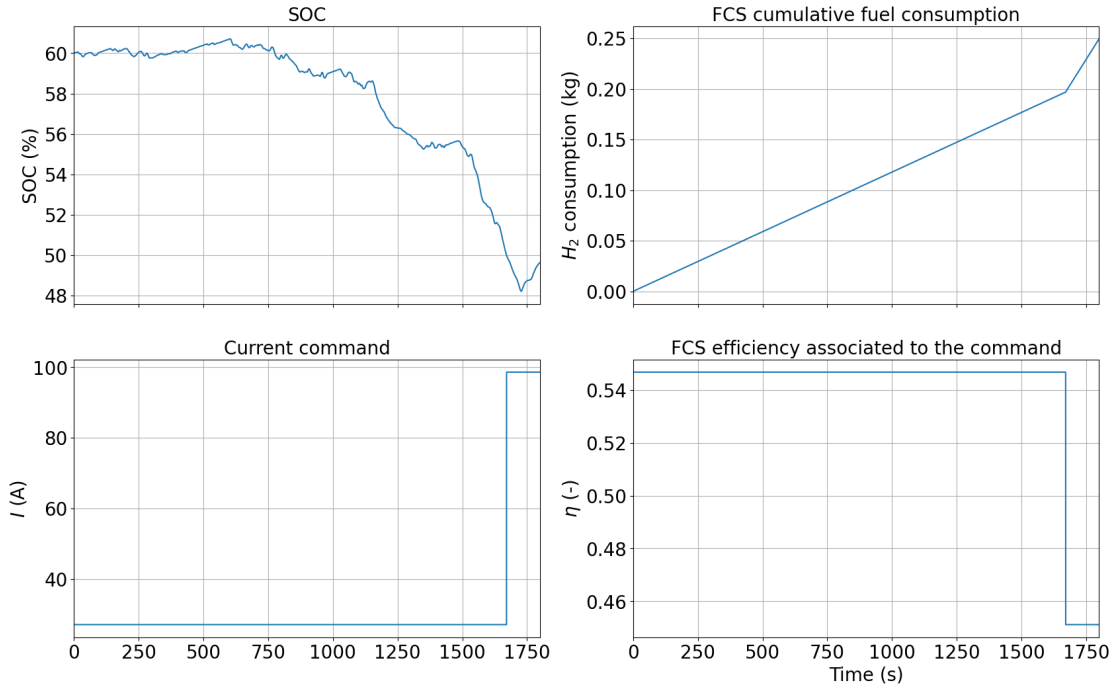

Figure 3.3: Results of the implemented RBC algorithm for the FCHEV without supercapacitors.

3.1.2 Battery downsizing

To compare the FCHEV model to a BEV in a relevant way, the IVECO eDaily vehicle is considered, as the IVECO eDaily Fuel Cell Electric Vehicle and IVECO Daily are the base of the FCHEV vehicle parameters. The eDaily has a battery size equal to 74kWh [49]. Considering a rated voltage of 345V, this corresponds to

the following battery capacity:

$$C_{batt} = \frac{E_{batt}}{U_{batt,r}} = \frac{74.10^3}{345} = 214.5\text{A.h} \tag{3.1}$$

For the fuel cell hybrid electric vehicle, the battery sizing process conducted in subsection 2.3.1 has led to a battery capacity of 135.3A.h. This represents a downsizing of the battery of 37%, which has a positive impact on vehicle mass as well as potential reduction of production emissions [9].
Figure 3.4 compares the evolution of the SOC and of the C-rates of the battery for the BEV with battery capacity equal to 214.5A.h and the FCHEV with the rule-based control algorithm and no supercapacitors. It highlights that the SOC is subject to less variations with the later vehicle model, closer to expected behavior of a Load Follower, but that it is subject to higher C-rates, which can be translated to a shorter battery life, although they remain under the 3C threshold, which is in line with the objectives.

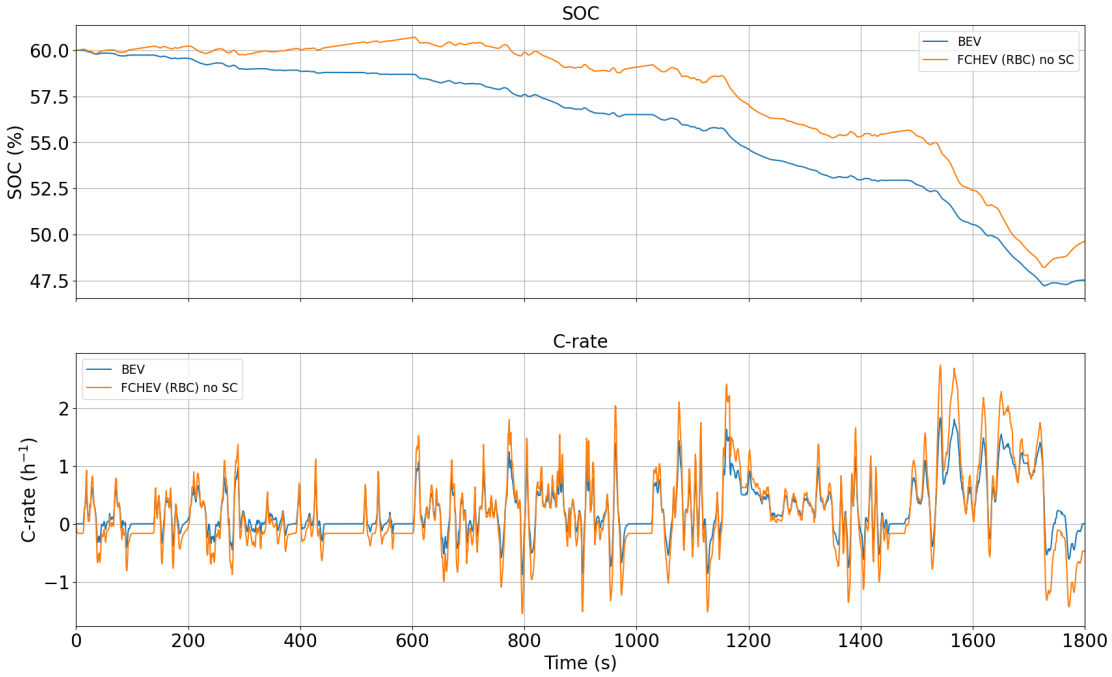

Figure 3.4: Time evolution of the SOC and the C-rates for the BEV and FCHEV without supercapacitors.

3.2 Evaluation of supercapacitors' impact on a fuel cell hybrid electric vehicle

The control strategy adopted for managing the power distribution between the supercapacitors and the battery is another rule-based control algorithm. The logic of the algorithm is presented in figure 3.5. The concept is to send all power requests who present a time derivative higher than a given threshold P'_{th} to the supercapacitors in order to preserve battery life.
However, the supercapacitors can only deliver a traction power request if it is charged to more than half of its maximal voltage [50]. It will also have priority in

charging from regenerative braking over the battery (which is being continuously charged by the FCS) if its voltage is below a given λ percentage of its maximum voltage, and will absorb the power request regardless of the voltage if its absolute time derivative is above P'_{th}.
This is translated in the Simulink model by a Matlab Function block that takes as input the power requests at time instants t and $t-1$, the voltage of the supercapacitors and some constants predefined in the Matlab workspace. It outputs the power command to send to the supercapacitors, which is subtracted from the initial power request to compute the power command for the battery. The commented code of the block is detailed in Listing 3.2.

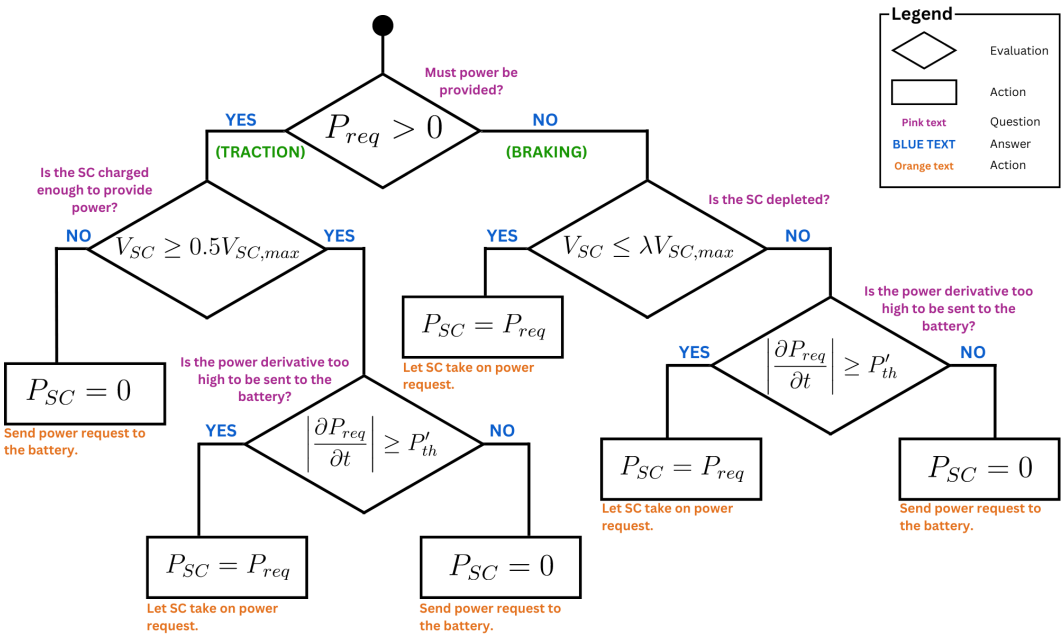

Figure 3.5: Diagram of the rule-based control algorithm for the supercapacitors.

```
function P_SC = RBC_SC(P_req_t, P_req_t_1, dt, V_SC_max, V_SC,
    charge_th_SC, P_der_threshold)
% Inputs:
%   - P_req_t: Requested power at time t (W)
%   - P_req_t_1: Requested power at time t-1 (W)
%   - dt: Time step (s)
%   - V_SC_max: Maximum voltage of the supercapacitor (V)
%   - V_SC: Current voltage of the supercapacitor (V)
%   - charge_th_SC: Percentage threshold of the max voltage under
    which
%    to charge the SC (-)
%   - P_der_threshold: Threshold for power derivative (W/s)
% Output:
%   - P_SC: Power to be attributed to the supercapacitor (W)
% Calculate power derivative
P_der = (P_req_t - P_req_t_1) / dt;

if P_req_t > 0
    if V_SC >= 0.5 * V_SC_max && abs(P_der) >= P_der_threshold
        P_SC = P_req_t;
    else
        P_SC = 0;
```

```
21      end
22  else
23      if V_SC <= charge_th_SC * V_SC_max || abs(P_der) >=
        P_der_threshold
24          P_SC = P_req_t;
25      else
26          P_SC = 0;
27      end
28  end
```

Listing 3.2: Coded algorithm of the RBC for the supercapacitor

The values of P'_{th} and λ were not chosen randomly, but determined by conducting two designs of experiment.

Design of experiment conducted on the power derivation threshold

To determine the threshold for the time derivative of the power, its evolution over the WLTP cycle has been plotted, for a vehicle mass of $M = 4200$kg, and is displayed in figure 3.6. It highlights that most peaks are of the OOM of 10^4W.s^{-1}. Therefore, the DOE has been conducted on values of P'_{th} ranging from 1000W.s^{-1} to 40000W.s^{-1}.

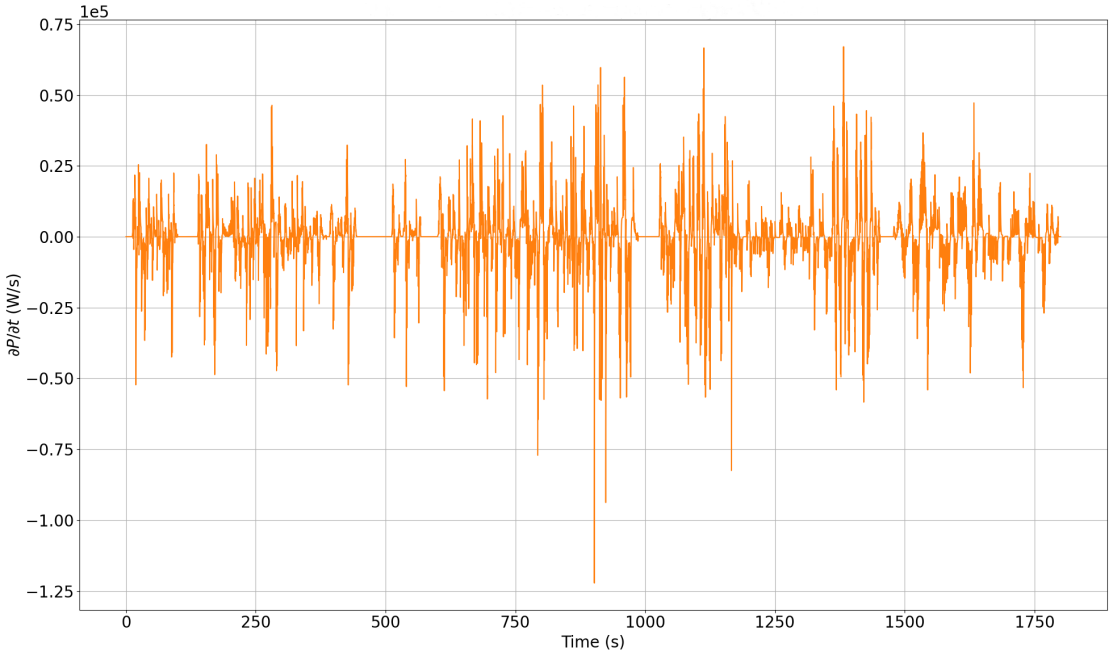

Figure 3.6: Time derivative of the power request over the WLTP cycle.

Figure 3.7 highlights (by looking at the Y-axis scale) that the threshold value has little to no impact on the maximum C-rate experienced by the battery, whose capacity has been chosen so that it experiences a maximum C-rate of 3h^{-1}.
As for the SOC of the battery, as can be seen on figure 3.8, its minimum value along the WLTP cycle is maximal for $P'_{th} = 1.10^5$W.s^{-1}, although the impact of the threshold value does not significantly impact it.
By looking at figure 3.9, it can be seen that the maximum current experienced by the supercapacitors is minimal for $P'_{th} = 2.10^5$W.s^{-1} For the aforementioned value

of 1.10^5W.s^{-1}, the maximum current is also quite low, at 550A.
Finally, figure 3.10 highlights the power distribution between the battery and the supercapacitors. For $P'_{th} = 1.10^5$W.s^{-1}, the distribution is about 84% and 16% for the battery and supercapacitors respectively, while for $P'_{th} = 2.10^5$W.s^{-1} it is closer to 95% and 5% respectively.

Because the supercapacitors are added to be used, the value of P'_{th} is set to 1.10^5W.s^{-1}.

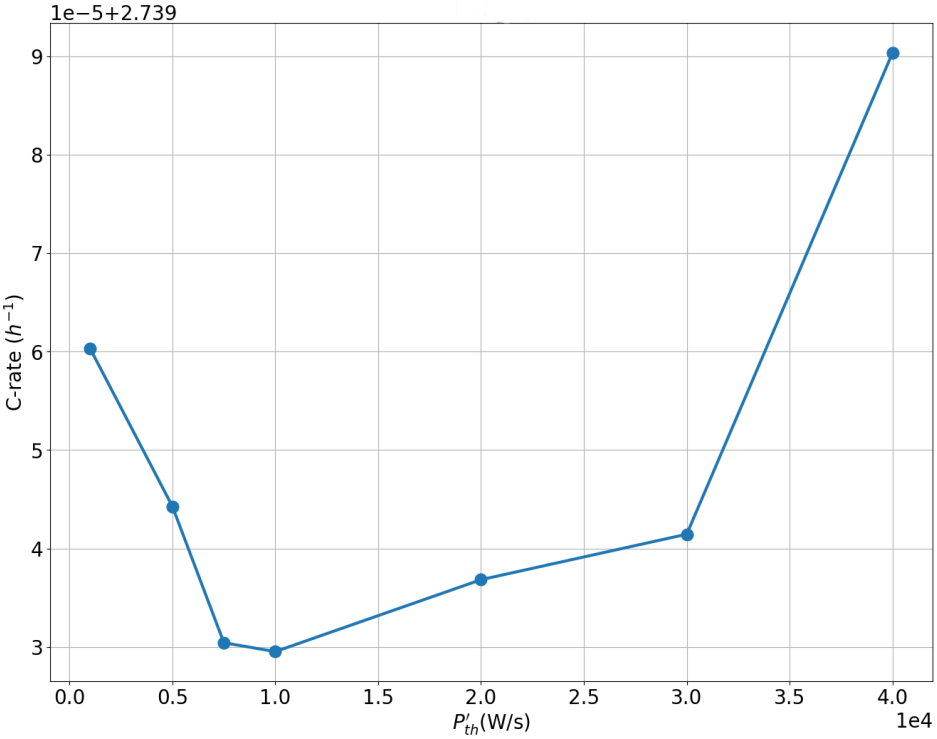

Figure 3.7: Maximum C-rates reached by the battery during the WLTP cycle as a function of P'_{th}.

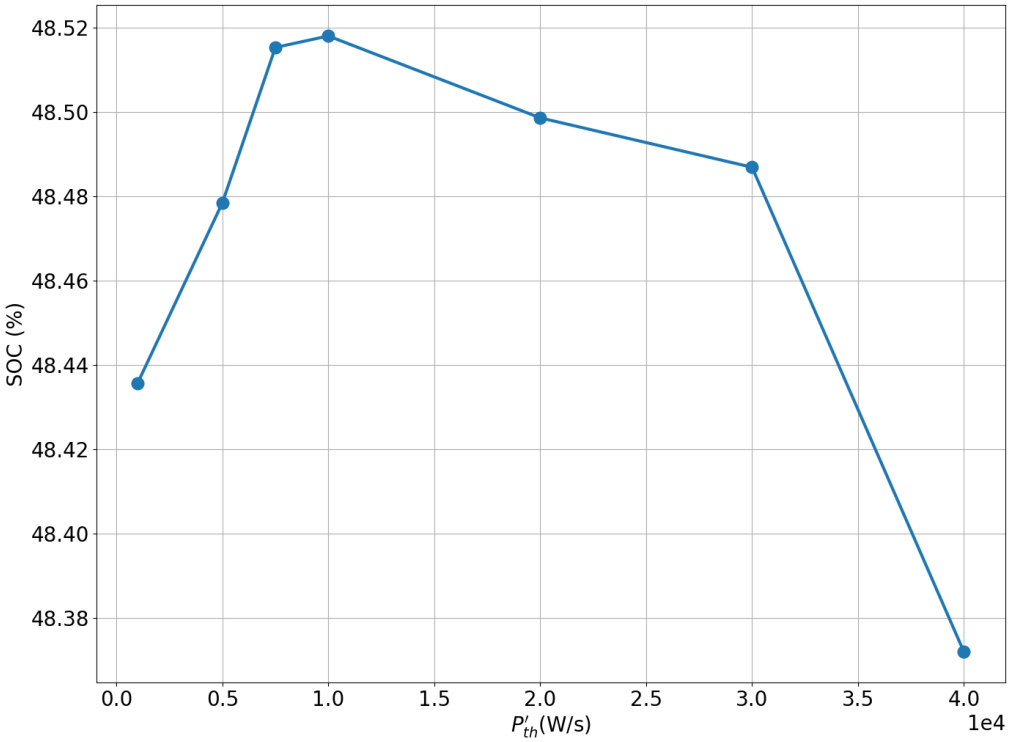

Figure 3.8: Minimum SOC reached during the WLTP cycle as a function of P'_{th}.

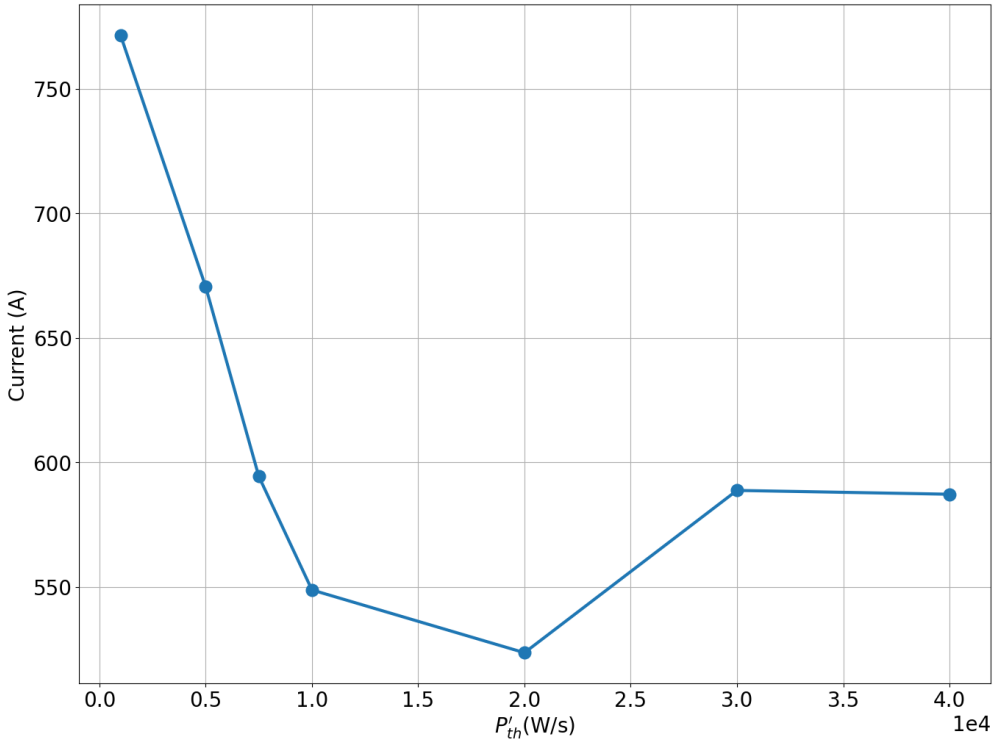

Figure 3.9: Maximum current reached by the supercapacitors during the WLTP cycle as a function of P'_{th}.

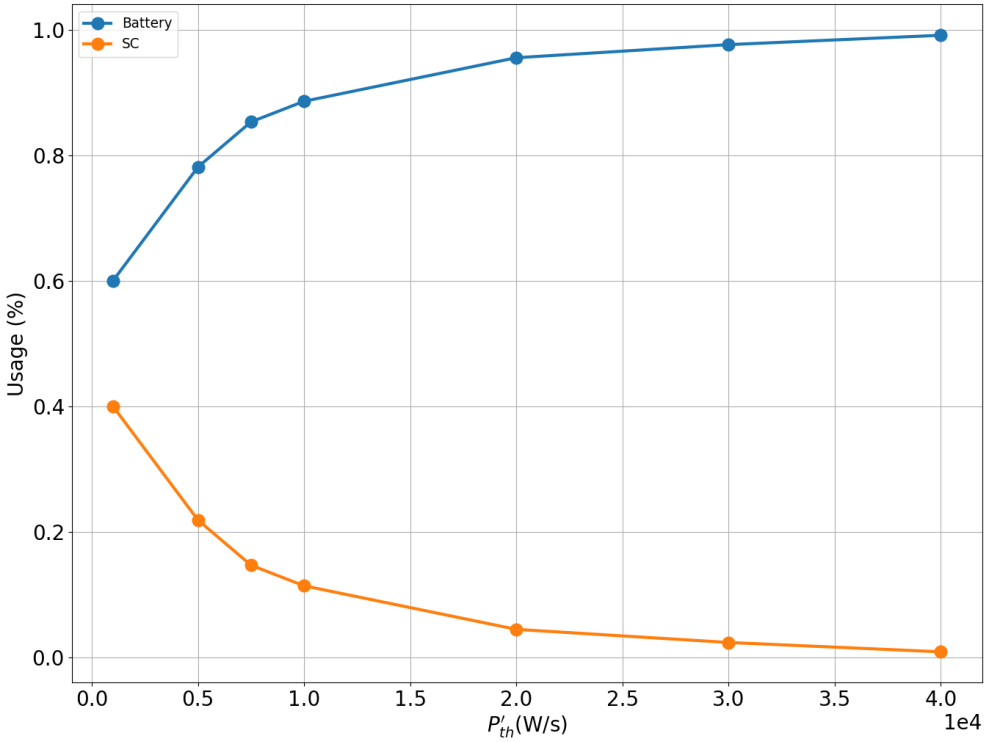

Figure 3.10: Power distribution between the battery and supercapacitors during the WLTP cycle as a function of P'_{th}.

Design of experiment conducted on the charging threshold

The charging threshold value λ represents the percentage of the rated voltage below which the supercapacitors should be charged. It has been determined by conducting a DOE on 3 values ([0.5, 0.6, 0.7]), using the P'_{th} value determined above. On figure 3.11, it can be seen that a value of $\lambda = 0.7$ allows to reduce significantly the negative C-rates experienced by the battery. This is due to the fact that the charging window is higher, as can be seen in figure 3.12, where the voltage is allowed to go back to a higher value.
However, as figure 3.13 demonstrates, for such a value of λ, the maximum current experienced by the supercapacitors is the highest of all tested values, about 840A, which remains however under the maximum peak current specified in table 2.4.
Finally, as shown by figure 3.14, the usage of the supercapacitors increases with λ, up to 30% over the WLTP cycle for $\lambda = 0.7$.

As the objective is to reduce the C-rates experienced by the battery, the chosen value of λ is 0.7.

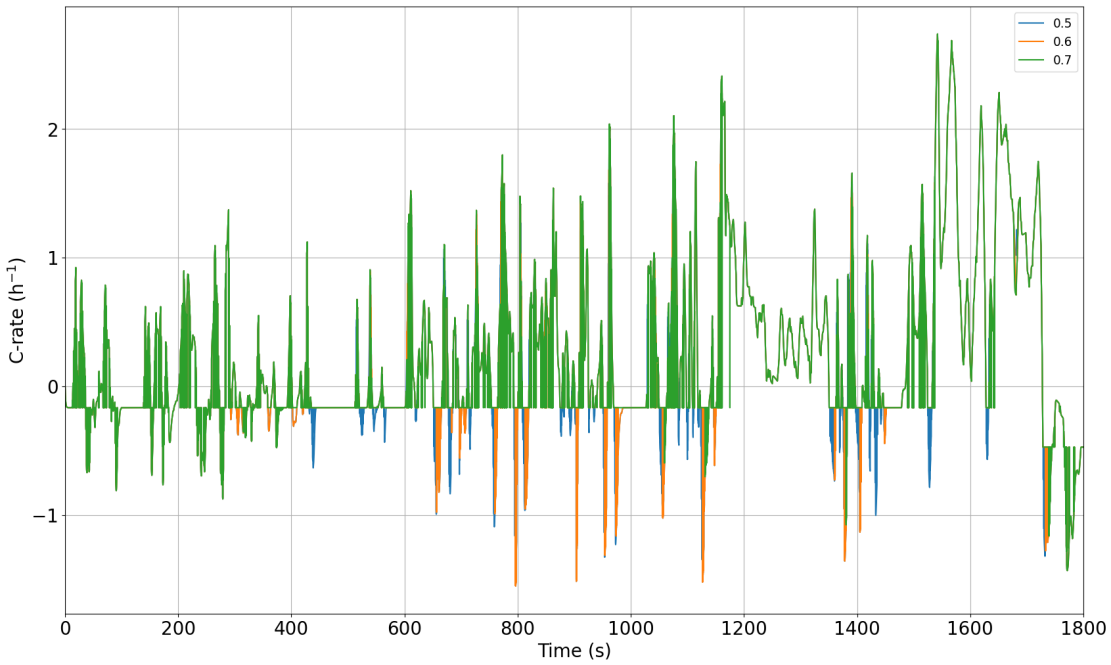

Figure 3.11: Evolution of the C-rates reached by the battery during the WLTP cycle.
The legend represents the values of λ.

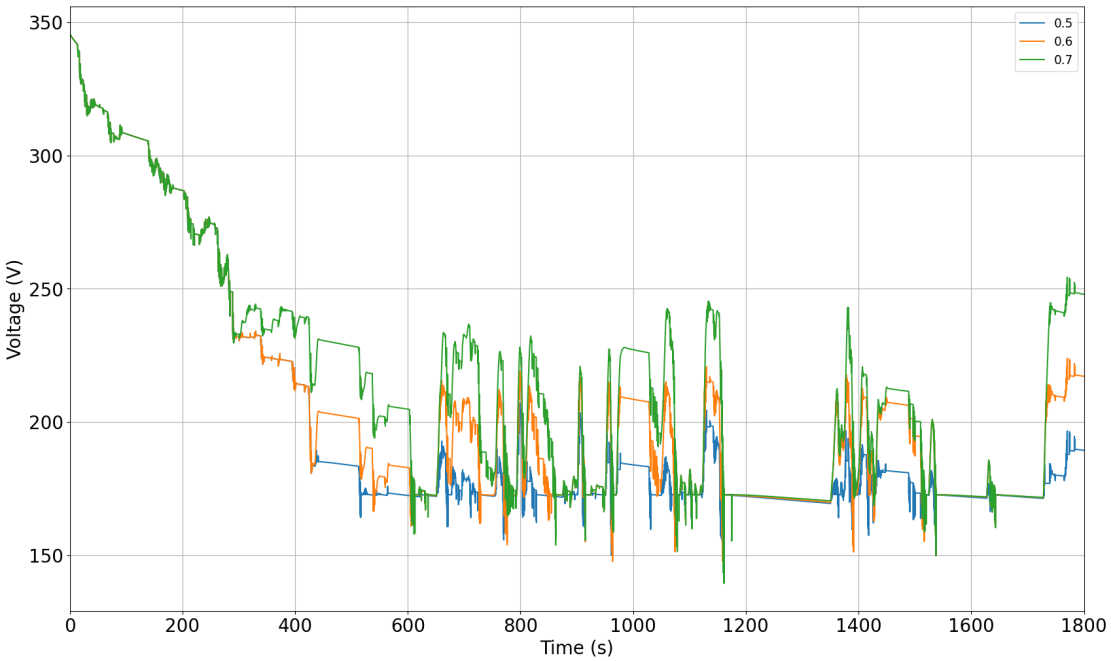

Figure 3.12: Evolution of the supercapacitors voltage during the WLTP cycle.
The legend represents the values of λ.

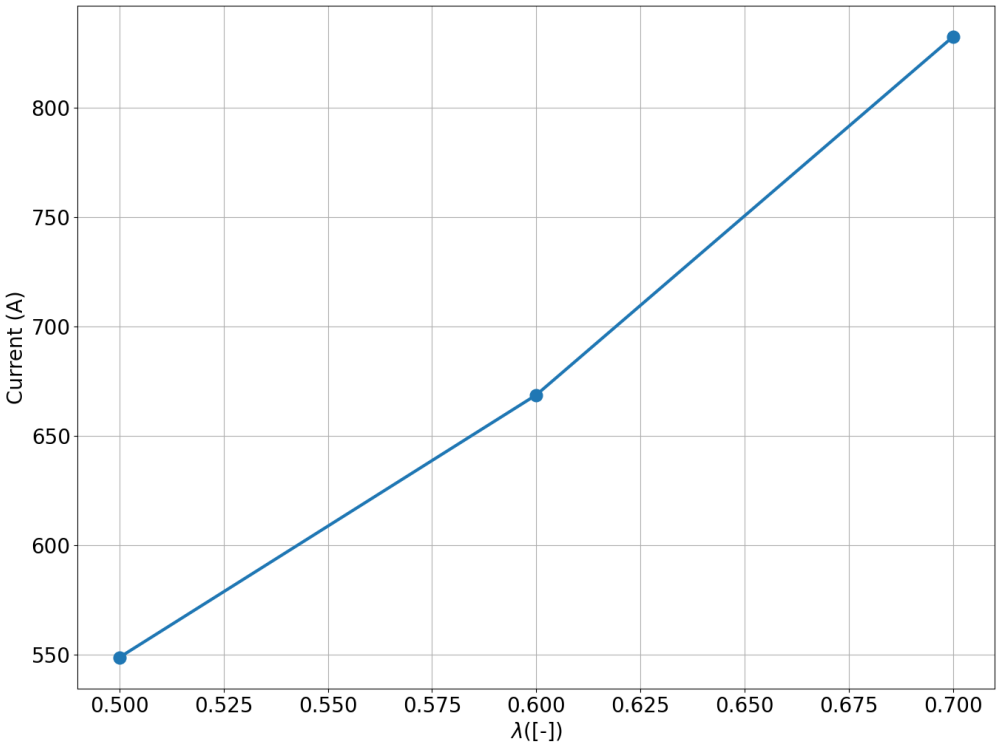

Figure 3.13: Maximum current reached by the supercapacitors during the WLTP cycle as a function of λ.

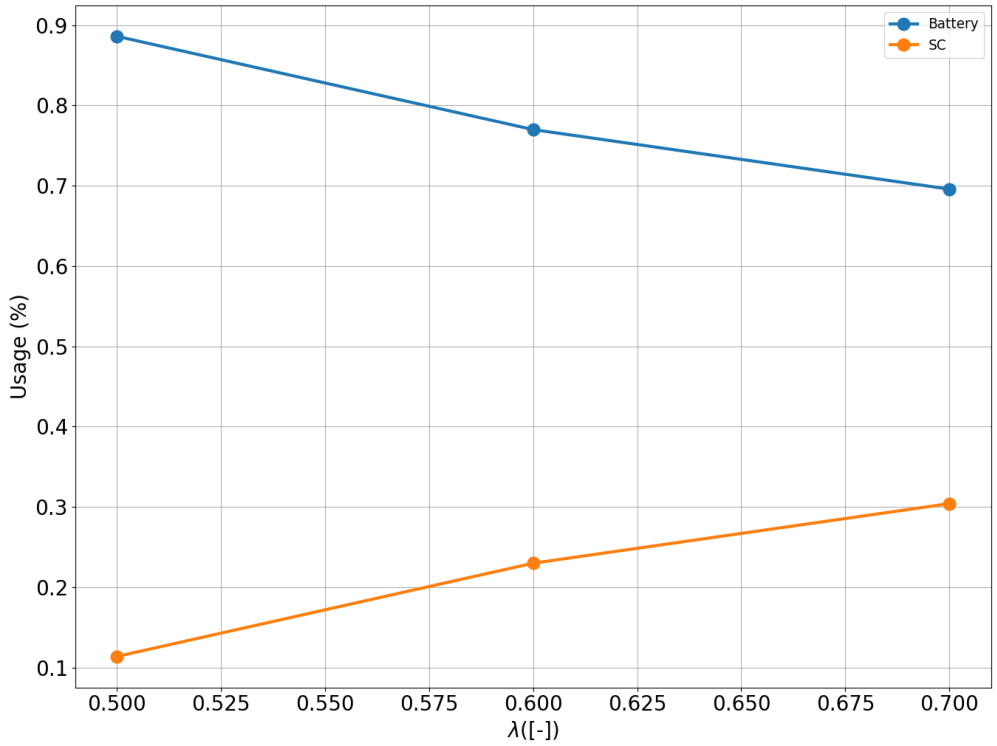

Figure 3.14: Power distribution between the battery and supercapacitors during the WLTP cycle as a function of λ.

3.2.1 Measure of supercapacitors' impact on battery life

To evaluate the impact of adding the supercapacitors on battery life, the evolution of the battery SOC and of the C-rates resulting from the FCHEV model without and with supercapacitors have been evaluated and compared on figure 3.15. It is evident that adding supercapacitors has little to no impact on the SOC of the battery but it seems to have a significant impact on the negative C-rates experienced by the battery.

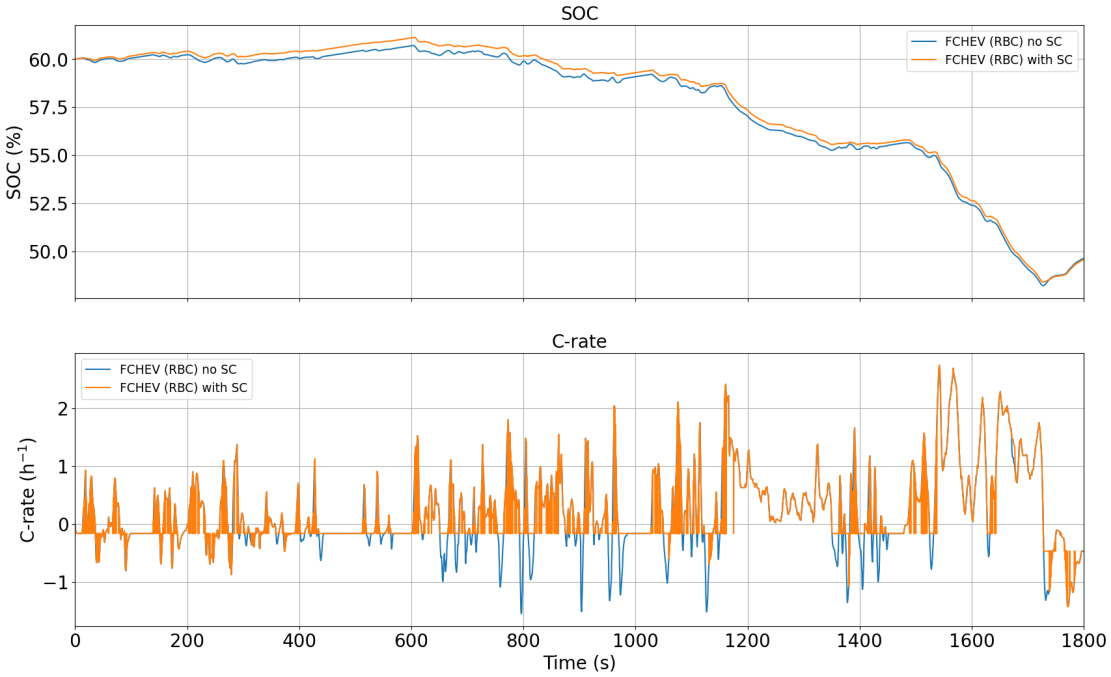

Figure 3.15: Time evolution of the SOC and the C-rates for the FCHEV without and with supercapacitors.

In order to quantify the impact, the root mean square calculation is introduced:

$$RMS = \sqrt{\frac{\sum_{i=1}^{N}(x_i)^2}{N}} \tag{3.2}$$

It is used to compute the RMS relative difference, defined as:

$$RMS_{\%} = \frac{RMS_y - RMS_x}{RMS_x} \times 100 \tag{3.3}$$

where x and y respectively represent the C-rates experienced by the battery without and with supercapacitors.
The quantified results are presented in table 3.1 and highlight the significant impact of the supercapacitors on the C-rates experienced by the battery, with an improvement of 9.76% with respect to the configuration with no supercapacitors.

		No supercapacitors	With supercapacitors
SOC	Absolute value (%)	57.76	58.03
	Relative difference	-	+0.47%
C-rate (*RMS*)	Absolute value (h^{-1})	0.72	0.65
	Relative difference	-	−9.76%

Table 3.1: Measure of impact on SOC and C-rate as a result of supercapacitors introduction.

3.3 Design of an adaptive energy management strategy for the fuel cell stack

3.3.1 Adaptive strategy

A second energy management strategy for the power delivery by the fuel cell stack to the battery has been proposed to improve the previously defined rule-based control strategy and try to achieve CS mode. This new strategy is called "adaptive" as it is based on a formulation of the FCS power that is a function of the difference between the actual SOC of the battery and a preset threshold SOC value. The idea is for the fuel cell stack to provide power at maximum efficiency when the SOC of the battery is greater than or equal to the threshold SOC and to provide more power as it is lower than the threshold. The initial value of the threshold state of charge is set to 60%, equal to the initial SOC. A somewhat similar approach has been developed by the authors of [37], although they are not focused on achieving maximum efficiency of the fuel cell.
The concept is illustrated on figure 3.16.

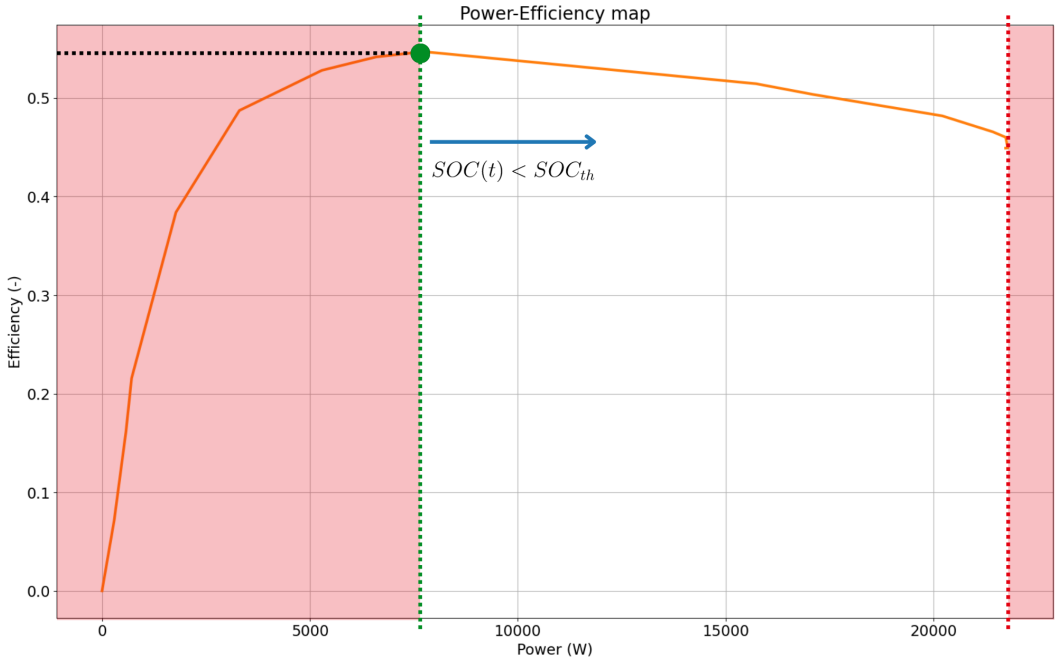

Figure 3.16: Operating area for the adaptive strategy of the FCS

In order to implement this strategy, the formulation defined in equation 3.4 is elaborated. It is defined such that the power provided by the fuel cell stack P_{FC} is bounded between $P_{FC}(\eta_{th})$ and $P_{FC,max}$, taking the following values:

- $P_{FC}(t) = P_{FC}(\eta_{max})$ if $SOC(t) = SOC_{th}$;
- $P_{FC}(t) > P_{FC}(\eta_{max})$ if $SOC(t) < SOC_{th}$;
- $P_{FC}(t) < P_{FC}(\eta_{max})$ if $SOC(t) > SOC_{th}$.

A tuning factor γ is introduced as an exponent to the normalized difference of actual and threshold SOC.

$$\mathrm{P}_{FC}(t) = max\left(P_{FC}(\eta_{th}), min\left(P_{FC,max}, P_{FC}(\eta_{max}) \times \left(1 + \frac{SOC_{th} - SOC(t)}{SOC_{th}}\right)^{\gamma}\right)\right) \quad (3.4)$$

In Simulink, the power in equation 3.4 is replaced with the current for simplicity with respect to the look-up tables available, hence why the current command will be considered going forward. The power of the fuel cell stack is computed multiplying the current command with the voltage of the FCS at the given time instant.

The method chosen for the optimization of γ is the bisection algorithm, where different values of γ are tested until $|f(\gamma)| < \varepsilon$, where $\varepsilon = 0.01$.
The bisection method aims at finding the optimal value of the argument that results in the image of the function being strictly inferior in absolute value to a threshold value ε. It does so by computing the image of a function for two initial arguments a and b. Both images must have different signs for the bisection method to work. If that is the case, the image of the function is computed for the mean value c of a and b. If the image $f(c)$ is of the same sign as $f(a)$ (respectively $f(b)$), then c becomes the new a (respectively b), and the process repeats until $|f(a)| < \varepsilon$ or $|f(b)| < \varepsilon$.
The first definition of $f(\gamma)$ is formulated to achieve the same SOC by the end of the WLTP cycle as that obtained with the formerly defined rule-based control strategy. Therefore,

$$f(\gamma) = \Delta SOC_{adaptive}(\gamma) - \Delta SOC_{RBC}(t = t_f) = \Delta SOC_{adaptive}(\gamma) - 10.43\%$$

For the bisection algorithm to be successful, the function $f(\gamma)$ should be continuous, which it is for $\gamma \in [0, +\infty)$.
Figure 3.17 shows the different values of γ tested and the resulting ΔSOC at the end of the WLTP cycle. The value of the tuning factor γ obtained is equal to 3.429.

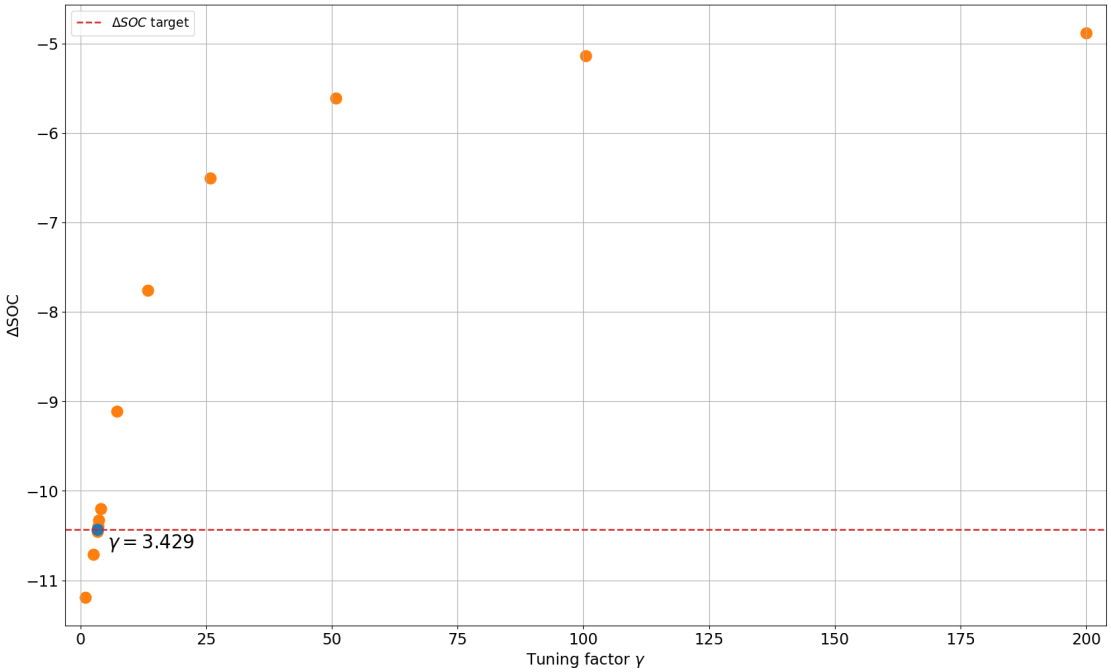

Figure 3.17: Tuning of γ factor through the bisection method to achieve equal SOC difference with both adaptive and rule-based control strategies.

3.3.2 Comparison between rule-based and adaptive control strategies

The main goal of implementing this adaptive strategy is to reduce the fuel consumption of the fuel cell and the C-rates the battery experiences due to the fuel cell stack in order to increase its life cycle duration. To evaluate the effects of implementing the adaptive strategy, the results are compared to those obtained with the rule-based control strategy defined in the subsection 3.1.1.
As figure 3.18 demonstrates, the adaptive strategy works as expected. Indeed, the current command varies continuously with time and is evidently a function of the battery SOC, as the current command becomes bigger than that of the maximum efficiency working mode of the RBC strategy when the SOC gets lower than the threshold SOC.
The results are displayed in figure 3.19, which shows the time evolution over the WLTP cycle of the battery SOC, the cumulative fuel consumption of the fuel cell stack, and the C-rates experienced by the battery.
The top plot shows that the objective of obtaining an equal SOC by the end of the cycle is achieved.
The fuel consumption, whose cumulative evolution is represented in the middle plot, is slightly lower for the adaptive strategy with respect to the RBC strategy.
Conclusions are harder to draw visually for the C-rates, which are displayed in the bottom plot.

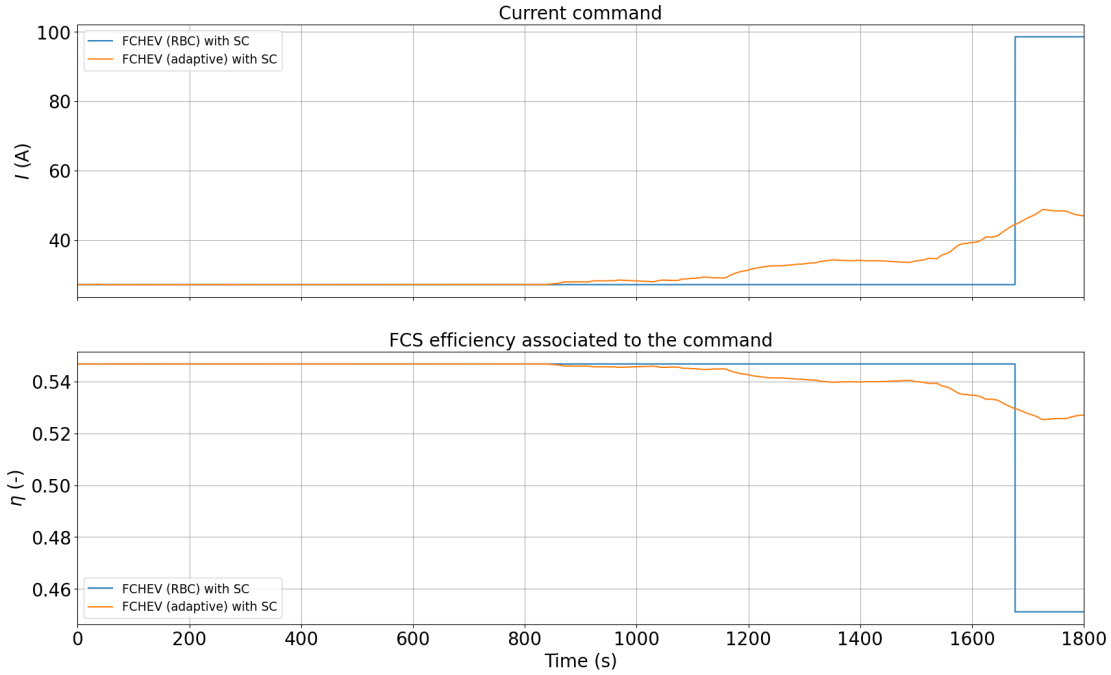

Figure 3.18: Comparison of the command signals for the RBC and adaptive methods on the WLTP cycle.

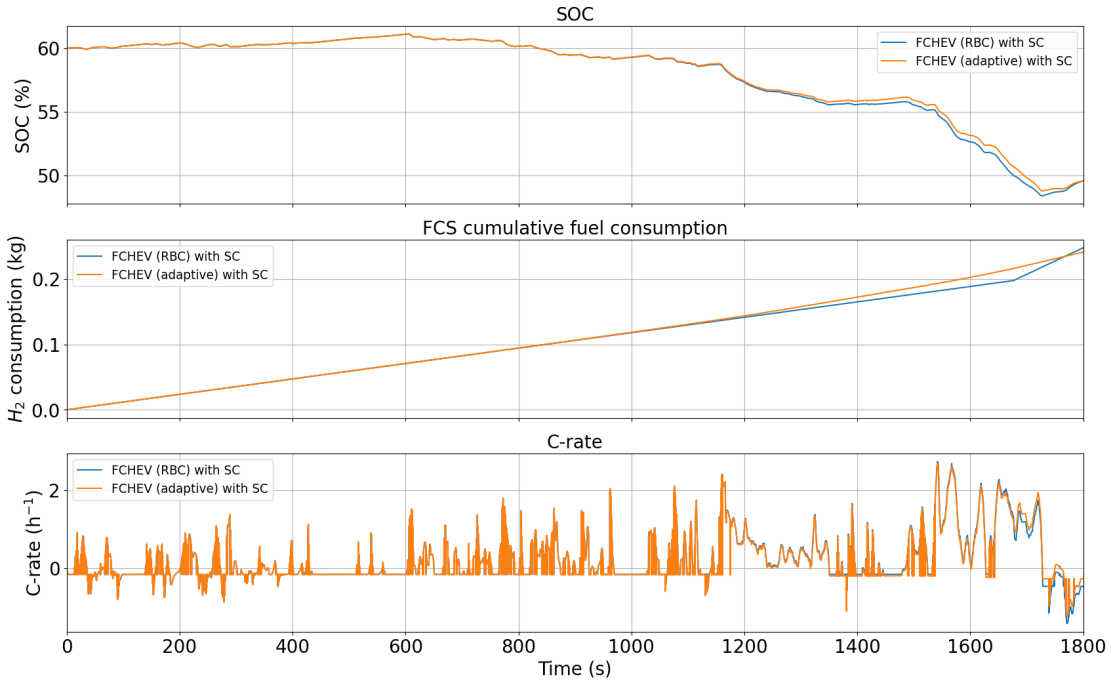

Figure 3.19: Comparison of main results for the RBC and adaptive methods on the WLTP cycle.

In order to quantitatively interpret those results, the relative difference of the results obtained from the adaptative strategy with respect to those obtained with the rule-based control strategy, is computed for the following parameters over the WLTP cycle:

- the final H_2 consumption;
- the RMS value of the C-rates.

The results are displayed in table 3.2. It highlights that the adaptive strategy achieved decreased C-rates as desired, more specifically a decrease of 1.5% for the RMS value of the C-rates.
Moreover, a decrease in fuel consumption is observed, with a quantitative reduction of 2.7% with respect to that obtained with the rule-base control strategy.

	C-rates (*RMS*)		**H_2 consumption**	
	Value (h^{-1})	Relative difference	Value (kg)	Relative difference
RBC	0.65	-	0.25	-
Adaptive	0.64	-1.5%	0.24	-2.7%

Table 3.2: Absolute values and relative difference of relevant parameters between the reference RBC strategy and the adaptive strategy.

3.3.3 Charge sustaining considerations

An interesting constraint to bring to the battery is the charge-sustaining mode over the WLTP cycle, which is characteristic of Load Follower architectures. Charge-sustaining means that the battery state of charge at the end of the cycle must be equal to its initial value.
To reach charge-sustaining mode with the rule-based control strategy, the minimum SOC threshold SOC_{min}, under which the fuel cell stack works at maximum power, must be increased. To find the value of SOC_{min} that ensures charge-sustaining mode, *i.e.* $f(\gamma) = \Delta SOC(\gamma) = 0$, the bisection method is used. As figure 3.20 shows, the ideal value of the SOC minimum threshold obtained is 64.648%.

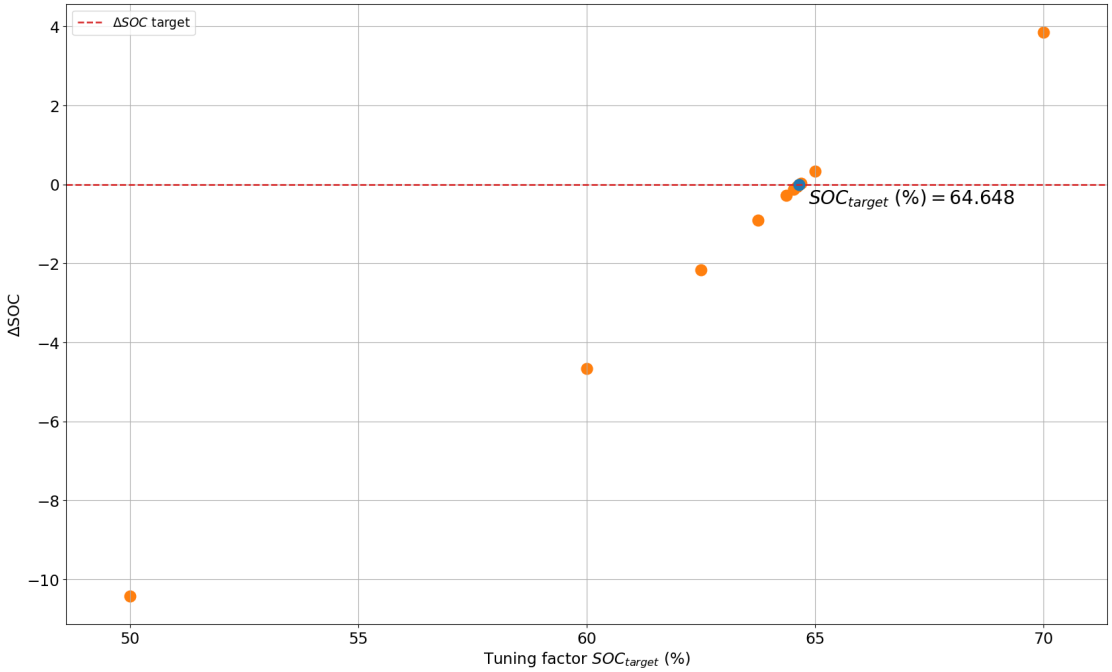

Figure 3.20: Tuning of the threshold value of SOC_{min} through the bisection method to achieve charge-sustaining mode with the rule-based control strategy.

Based on this value, the threshold value SOC_{th} of the adaptive strategy is increased from 60% to 65%, 70%, 75% and 80% to obtain charge-sustaining mode. Indeed, with $SOC_{th} = 60\%$, the bisection algorithm cannot converge, even with values of the tuning factor γ as high as 1e9. Moreover, when trying with $SOC_{th} = 64.648\%$, the value obtained for the RBC strategy, the bisection algorithm does not converge either. The results of the bisection algorithm conducted on finding γ (such that charge-sustaining mode is achieved) for each tested value of SOC_{th} are displayed in Appendix 5 on figures A.1, A.2, A.3 and A.4, and the optimal values of the tuning factor γ are reported in table 3.3.

$\boldsymbol{SOC_{th}}$ (%)	65	70	75	80
Tuning factor γ	149.3	12.1	7.0	5.3

Table 3.3: Values of tuning factor γ for different values of SOC_{th} of the adaptive strategy over the WLTP cycle in charge-sustaining mode.

The results of the different simulations are displayed in figure 3.21. Since they are quite difficult to qualitatively interpret, the relative difference with respect to the baseline results obtained with the RBC strategy is computed for the RMS value of the C-rates and for the fuel consumption resulting from each variation of the adaptive strategy. These quantitative results are reported in table 3.4. It can be seen that all of the variants of the adaptive strategies result in a lowered fuel consumption and slightly increased C-rates with respect to that obtained with the rule-based control strategy. Moreover, it can be remarked that increasing the threshold value of the SOC in the adaptive strategy results in higher decreases in fuel consumption, up to a decrease of 6.63% with respect to the fuel consumption obtained with the RBC, and very slightly higher increases of the RMS value of the

C-rates experienced by the battery, up to 1.93%.

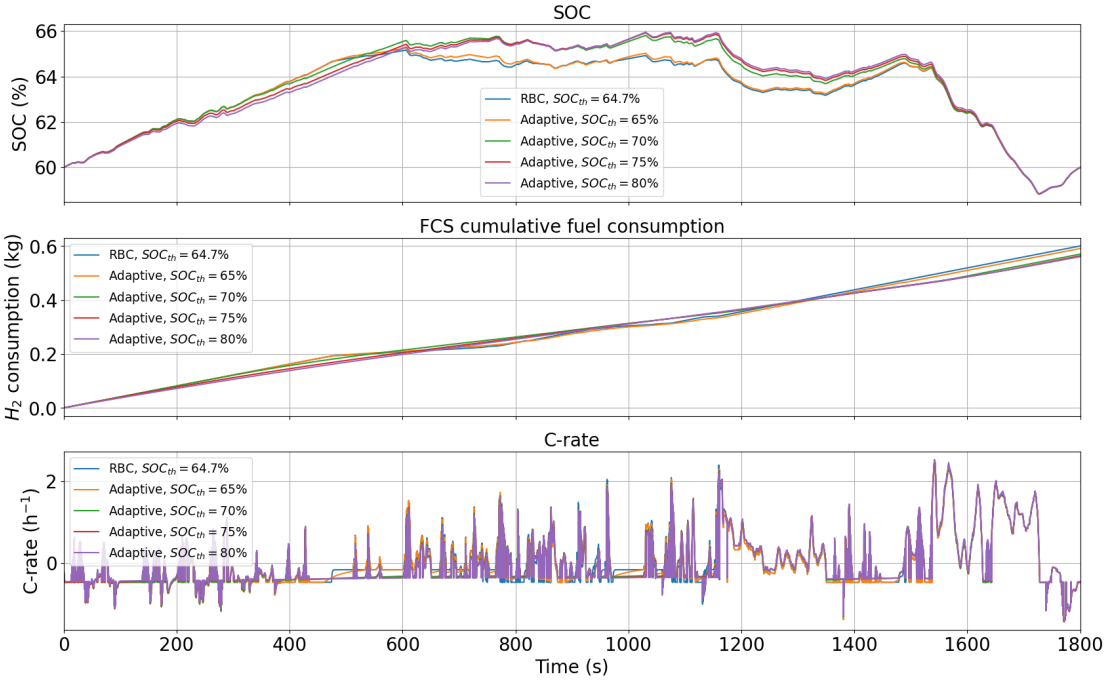

Figure 3.21: Comparison of main results for the RBC and adaptive method on the WLTP cycle when working in charge-sustaining mode.

	C-rates (*RMS*)		**H_2 consumption**	
	Value (h^{-1})	Relative difference	Value (kg)	Relative difference
RBC	0.606	-	0.601	-
Adaptive (SOC_{th}=65%)	0.610	0.59%	0.591	-1.55%
Adaptive (SOC_{th}=70%)	0.616	1.61%	0.571	-5.02%
Adaptive (SOC_{th}=75%)	0.617	1.82%	0.564	-6.08%
Adaptive (SOC_{th}=80%)	0.618	1.93%	0.561	-6.63%

Table 3.4: Absolute values and relative difference of relevant parameters between the reference RBC strategy and the different adaptive strategies with charge-sustaining mode on the WLTP cycle.

The decreased fuel consumption can be explained by looking at figure 3.22, which shows the current command of the fuel cell stack and the efficiency at which it operates. Combined with the histogram on figure 3.23, which aims at better showing at which efficiency the fuel cell stack tends to operate, it can be seen that the adaptive strategies result in the FCS operating less frequently at low efficiency and more often at medium to high efficiency. Interestingly, it can be noticed that for $SOC_{th} \geq 70\%$ the fuel cell stack actually never operates at maximum efficiency, but compensates by operating at moderate efficiency and very rarely at low efficiency.

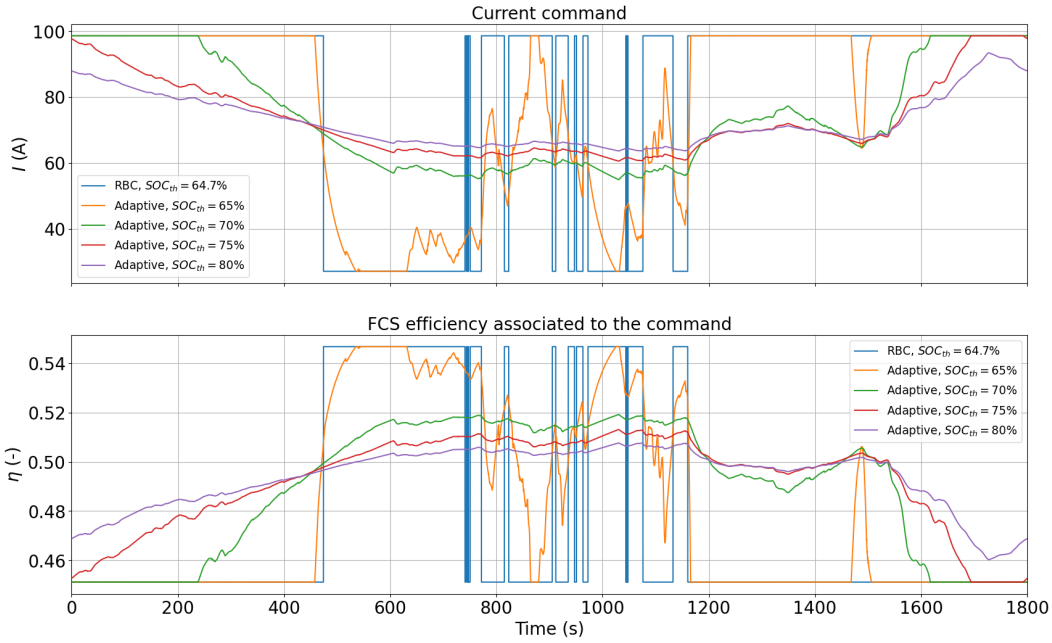

Figure 3.22: Comparison of the command signals for the RBC and adaptive method on the WLTP cycle when working in charge-sustaining mode.

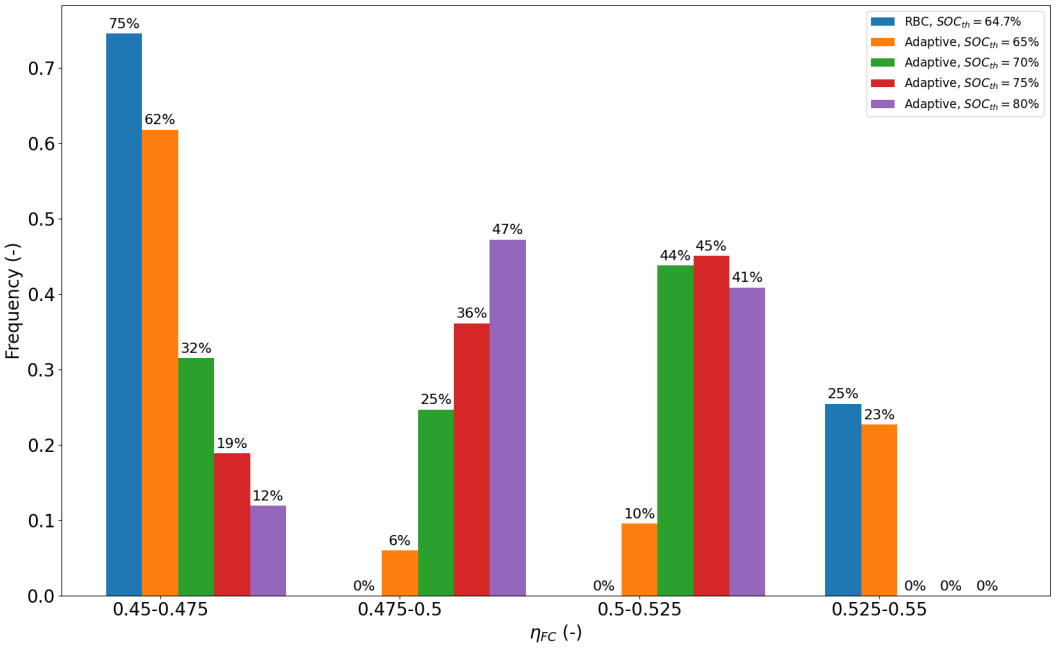

Figure 3.23: Histogram of the frequency of the fuel cell stack efficiency for the RBC and adaptive method over the WLTP cycle when working in charge-sustaining mode.

It can therefore be concluded that, when operating at charge-sustaining mode, the adaptive strategy results in fuel economy with respect to the rule-based control strategy, with decreases from 1.55% up to 6.63%. However, this comes at the cost of higher C-rates experienced by the battery, with a relative difference in root mean square value between +0.59% and +1.93%, which means a slightly decreased battery life.

Chapter 4

Scaling-down method for hardware-in-the-loop applications

To verify that the vehicle model is valid and that the associated control strategies work as expected in real life as they do online, it is relevant to design and make a test bench. Indeed, the control logic can be tested on the physical components of the bench, in what is called a hardware-in-the-loop test. However, making a 1:1 scale bench with respect to the vehicle is not pertinent for many reasons, including costs, safety, feasibility and space, and a scaled-down bench is to be considered. The goal of this chapter is to choose a scaling-down strategy, validate it for the model developed in this thesis and standardize the procedure.

4.1 Literature review of scaling-down strategies

A literature review has been conducted and three main categories of scaling-down strategies have been identified in order to downscale the vehicle model for the test bench.
The first type of strategy is to apply a scaling factor k to the individual parameters of the vehicle and compute the scaled-down power request from the resistance forces with these new parameters [51][52]. This strategy has the advantage of being quite simple to implement, but it only allows to downscale the entire power request and therefore can only contribute to downscaling the electric machine, not the rest of the components.
The second strategy consists in applying the Buckingham π-theorem, which is a dimensionless theory that allows to reduce the number of parameters and make dynamically equivalent systems [53][54][55]. This approach presents the advantage of using a rigorous method to scale down all the components of the powertrain but it is very complex and presents a steep and long learning curve.
Finally, the third type of scaling-down strategy considered is the impedance matching strategy [56]. It is widely used in a lot of research fields, but papers on research associated to this strategy applied to the automotive industry are scarce.

	Scaling factor	Buckingham π-theorem	Impedance matching
Complexity	simple	complex	simple
Downscaling EM	yes	yes	yes
Downscaling power sources	no	yes	?
Implementation time	low	high	high

Table 4.1: Decision table to compare the scaling-down strategies.

Based on the summary presented in table 4.1, the first strategy of the scaling factor, particularly as described by the authors of [51] is adopted and will be explored henceforth. It will allow to scale down the electric machine of any hybrid electric vehicle, in particular all of the configurations of the FCHEV studied in this thesis.

4.2 Evaluation of power computation method suitability with respect to Simulink model

Before implementing the chosen downscaling strategy, it is important to make sure that the power request computed from the resistance forces, as presented in the paper [51], is the same as the one output by the much more complex Simulink model.
To this effect, the total resistance force F_{res} is considered as the sum of the aerodynamic resistance force:

$$F_{aero} = \frac{1}{2}\rho A_f C_d (V + V_{wind})^2 \tag{4.1}$$

the inertia force:

$$F_{iner} = M.a \tag{4.2}$$

the rolling resistance force:

$$F_{rr} = k_r.M.g.\cos\alpha \tag{4.3}$$

and the climbing resistance force:

$$F_{cl} = M.g.\sin\alpha \tag{4.4}$$

The parameters of these forces are defined in the following table.

Parameter	Notation	Unit	Value
Air density	ρ	$\mathrm{kg.m^{-3}}$	1.21
Frontal area	A_f	$\mathrm{m^2}$	4.5808
Drag coefficient	C_d	-	0.316
Vehicle speed	V	$\mathrm{m.s^{-1}}$	$f(t)$
Wind velocity	V_{wind}	$\mathrm{m.s^{-1}}$	0
Vehicle mass	M	kg	4200
Vehicle acceleration	a	$\mathrm{m.s^{-2}}$	$f(t)$
Rolling resistance coefficient	k_r	-	0.015
Gravity acceleration	g	$\mathrm{m.s^{-2}}$	9.81
Road inclination angle	α	rad	0

Table 4.2: Parameters of the resistance force equations.

The resistant power to overcome is computed by multiplying the total resistance force with the vehicle velocity, which is obtained from the WLTP cycle.

4.2.1 Evaluation of numerical derivation schemes for the acceleration computation

As a way to choose the most appropriate numerical derivation scheme for the acceleration, three finite difference methods are considered and the strength of the correlation with respect to the reference power request obtained from Simulink is evaluated for each of the schemes.
The numerical derivation schemes evaluated are presented in table 4.3 and the resulting power requests are plotted on figure 4.1.

Derivation scheme	Order	Expression
Forward	1	$a(i) = \frac{v(i+1)-v(i)}{t(i+1)-t(i)}$
Central	1	$a(i) = \frac{v(i+1)-v(i-1)}{t(i+1)-t(i-1)}$
2nd order forward (approx.)	2	$a(i) = \frac{-3v(i)+4v(i+1)-v(i+2)}{t(i+1)-t(i-1)}$

Table 4.3: Derivation schemes and the associated expression of the acceleration. i represents the given time step.

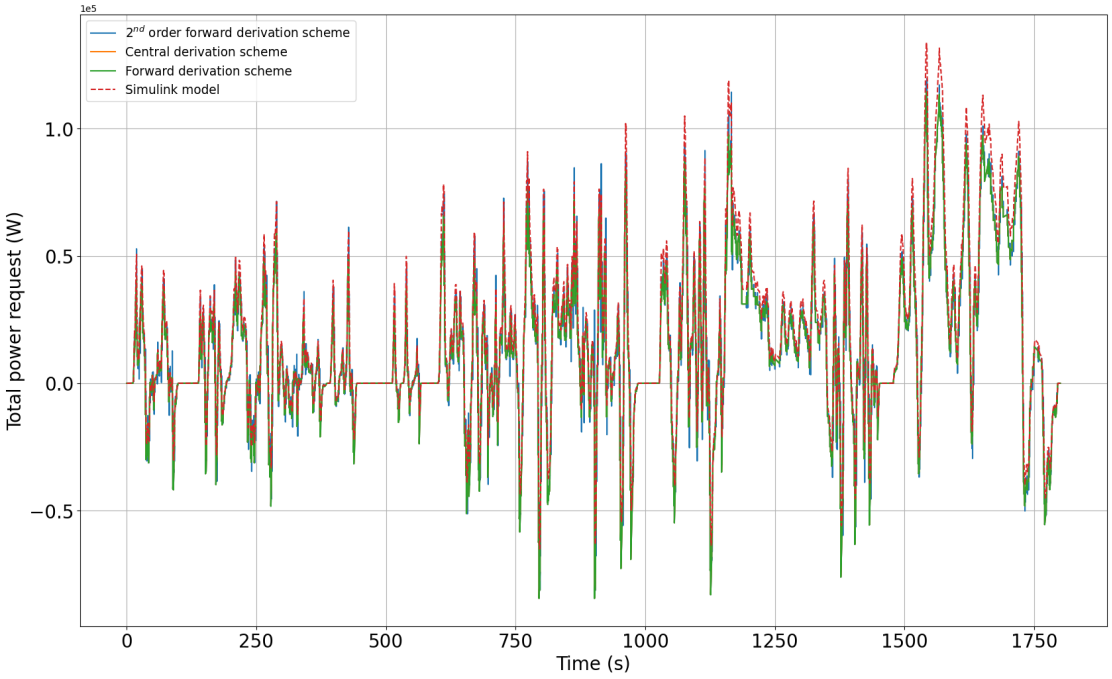

Figure 4.1: Comparison of power requests computed from the resistance forces with different derivation schemes for the acceleration.

It is evident that the power requests resulting from the resistant forces computation all are similar to that generated by the Simulink model but that they differ in the amplitude of the peaks. Visually, all the derivation schemes lead to a very similar evaluation of the power request but the differences are hard to tell qualitatively. Therefore, quantitative measures of the difference between the derivation schemes with respect to the reference power request from Simulink are introduced.
In particular, the RMS relative difference is evaluated, as defined in equation 3.3, as well as the Pearson correlation coefficient (PCC). The PCC, referred to as R, is a measure of the strength (between 0 and 1) and direction (negative or positive) of the correlation between two variables or, in this case, two datasets. It is defined as follows:

$$R_{xy} = \frac{C_{xy}}{\sqrt{C_{xx}C_{xy}}} \tag{4.5}$$

where C_{xy} is the covariance factor between datasets x and y, which is defined as such:

$$C_{xy} = \frac{\sum_{i=1}^{N}(x_i - \bar{x})(y_i - \bar{y})}{N-1} \tag{4.6}$$

where $\bar{x}$ is the average value of dataset x and N is the number of values in each dataset.
The results are presented in table 4.4 and highlight that the differences between the derivation schemes are very small and that the correlation is very strong ($R > 0.98$) between the resistance force-based model and the Simulink output.

Derivation scheme	$RMS_{\%}$	PCC (R)
Forward	12.1%	0.9811
Central	12.1%	0.9813
2nd order forward (approx.)	12.1%	0.9811

Table 4.4: Results of the comparison between the different derivation schemes with respect to the Simulink power request.

Given the results, the central finite different derivation scheme is chosen as it results in a slightly higher correlation to the reference power request than the other derivation scheme but the differences are so negligeable that any method would work equally.

4.2.2 Compatibility analysis between Simulink resistance force-based models

For clarity, the power request computed with the central finite difference derivation scheme is replotted on figure 4.2 against the reference from Simulink.

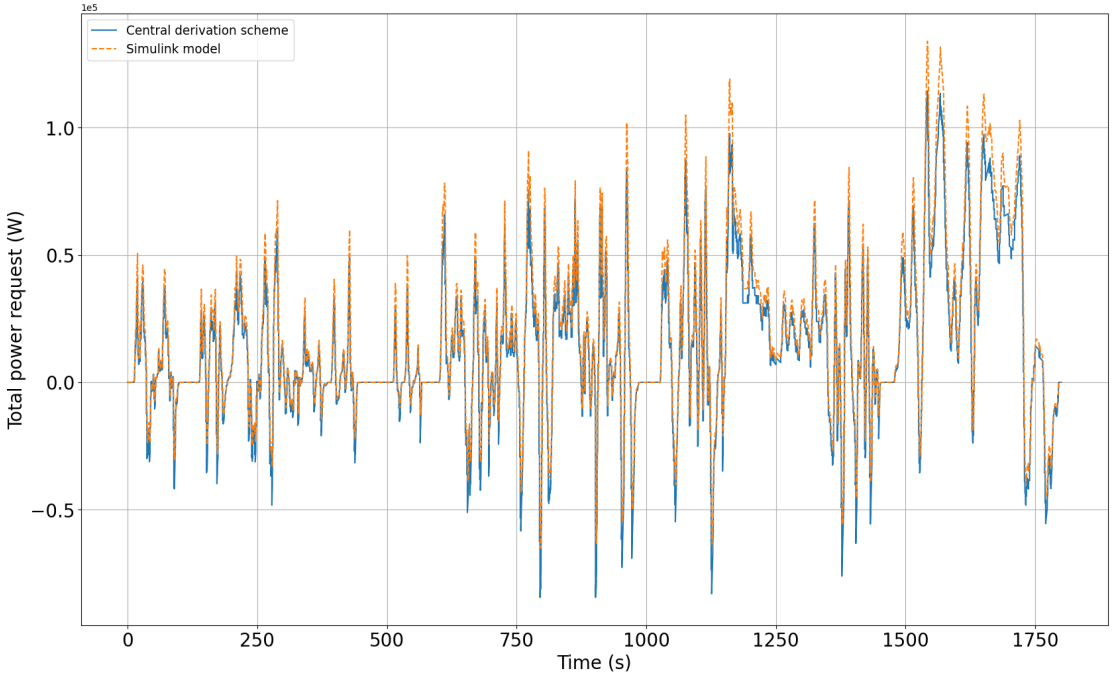

Figure 4.2: Comparison of power requests computed from the resistance forces and from the Simulink model.

The differences in peak amplitude between the power requests generated by the resistance force-based model and by the Simulink model may be explained by the encompassing aspect of the later. Indeed, in Simulink, the power request depends on the driver model, which outputs a torque command in order to palliate the difference between the reference speed profile of the WLTP cycle and the actual speed profile attained by the vehicle.

However, as shown by table 4.4, the correlation between the power request of the resistant force-based model and that of the Simulink model is very strong ($R > 0.98$) and the simplified model shall be considered close enough to carry on the analysis.

4.3 Computation and analysis of downscaled power request

The resistance force-based model having been validated, the scaling-down method from paper [51] can be introduced in more detail and implemented. In this method, a scaling factor k is applied to the equation of the total resistant force, obtained by summing the forces defined in equations 4.1, 4.2, 4.3 and 4.4. Following the laws of kinematic, this process is equivalent to downscaling the mass M, the acceleration a, the velocity v and the wind velocity V_{wind} by the factor k and downscaling the frontal area A_f by k^2. This results in the following definition of the downscaled (indicated by the index SD) resistant force:

$$F_{res,SD} = \frac{\frac{1}{2}\rho A_f C_d (V + V_{wind})^2}{k^4} + \frac{Ma}{k^2} + \frac{k_r M g \cos\alpha}{k} + \frac{M g \sin\alpha}{k} \tag{4.7}$$

The resistant power at the wheels being defined by the product of the resistant force and the velocity of the vehicle $P = F \times v$, the following expression of the scaled-down power request related to the full-scale velocity profile is obtained:

$$P_{SD} = F_{SD}.v_{SD} = F_{SD}\frac{v}{k} \tag{4.8}$$

Figure 4.3 shows the full-scale power request on the top plot and the downscaled power requests for different values of the scaling down factor k on the bottom plot. It can be seen that the power request is effectively scaled-down but that, for $k = 9$, the power request is no longer reaching negative values, *i.e.* there is longer the braking operation.

Figure 4.3: Full-scale and down-scaled (factor $k = 5$, $k = 7$, $k = 9$) power request over the WLTP cycle.

This is due to the fact that only the inertia force F_{iner} reflects the traction or braking component through the acceleration a. Looking at equation 4.7, it is evident that the inertia component of the resistance force will decrease faster than the climbing and rolling resistance components, due to being divided by k^2 instead of k, with only the aerodynamic component that will decrease faster.
Therefore, as the value of k increases, the inertia component will be dwarfed by the rolling resistance force, as shown by figure 4.4, and the scaled-down power request will no longer be representative of the full-scale power request.

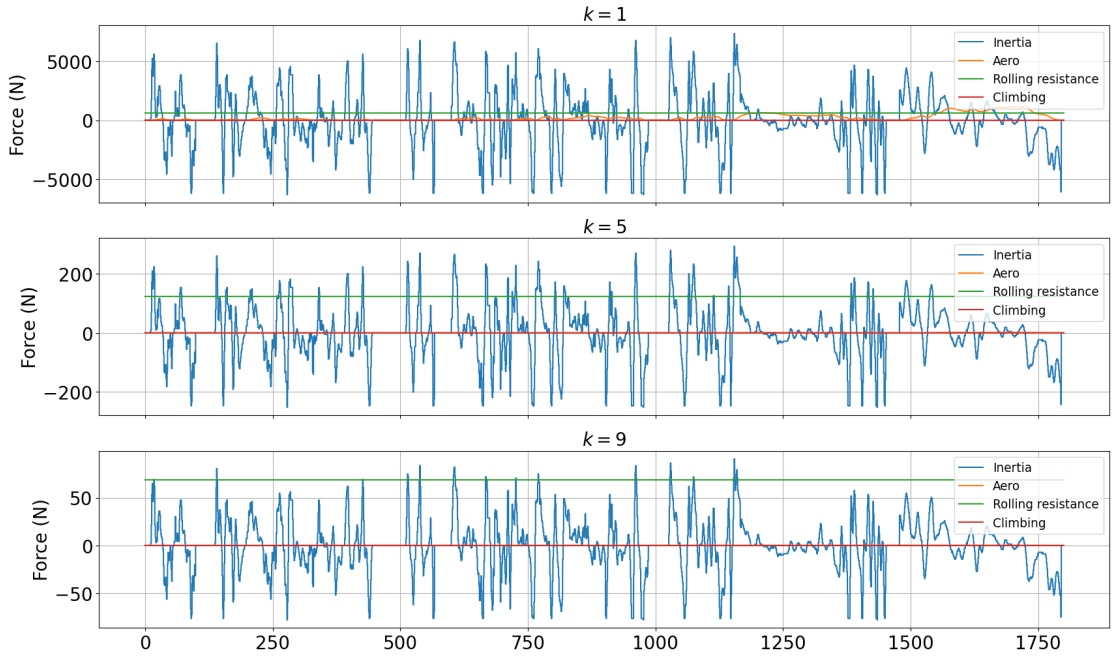

Figure 4.4: Components of the resistant force for $k = 1$, $k = 5$ and $k = 9$.

Based on the scaled-down power requests presented on figure 4.3, values of k strictly higher than 7, at which the power request still has some braking component, shall be considered not appropriate for the application at hand.

4.4 Determining the scaling factor k from a specified power ratio x

For the test bench application studied in this thesis, the interest is to specify a scaling-down ratio of the power request instead of the vehicle parameters.
In particular, what is of interest is to find the scaling-down factor k of the vehicle parameters associated to a given scaling-down factor x of the power request, in this case defined as the ratio between the maximum value of the full-scale power request and the maximum value of the scaled-down power request.
Moreover, it is important to see if the range of power ratios considered ($x \in [1, 100]$) yields a range of scaling-down factors whose values are systematically inferior to 7.
Finally, the analysis is conducted on three different test cases, which are detailed in table 4.5, in order to evaluate the robustness of the strategy that will be developed. In particular, Test 1 refers to the model used in this thesis, Test 2 refers to the model tested by the authors of [51] on the UDDS (Urban Dynamometer Driving Schedule) and Test 3 refers to a test on the WLTP cycle with a few parameter changes from Test 1.

Parameter	Notation	Unit	Test 1	Test 2	Test 3
Cycle	-	-	WLTP	UDDS (w/o initial 20s)	WLTP
Vehicle mass	M	kg	4200	2108	3100
Friction coefficient	k_r	kg/ton	15	17	10
Drag coefficient	C_d	-	0.316	0.280	0.316
Frontal area	A_f	m^2	4.58	2.15	4.58
Air density	ρ	$kg.m^{-3}$	1.21	1.225	1.21
Road inclination	α	degrees	0	0	0
Wind velocity	V_{wind}	$m.s^{-1}$	0	5	0
Rolling radius	r	m	0.350	0.352	0.350

Table 4.5: Definition of use cases used to test the robustness of the reverse procedure.

The first step of the process is to identify if there is a simple mathematical relation between the scaling factor k and the associated power ratio x. To achieve that, the power ratio x has been computed for a series of 20 values of the scaling factor k, between 2 and 10. The results are plotted on figure 4.5.
At first sight, all of the curves seem to have a similar behavior, which appears to be logarithmic. Moreover, it shows that the range of power ratios considered of $x \in [1, 100]$ is related to values of k up to 5.5, strictly and significantly inferior to the limit of 7, which confirms the relevance of the scaling-down method for the application at hand.

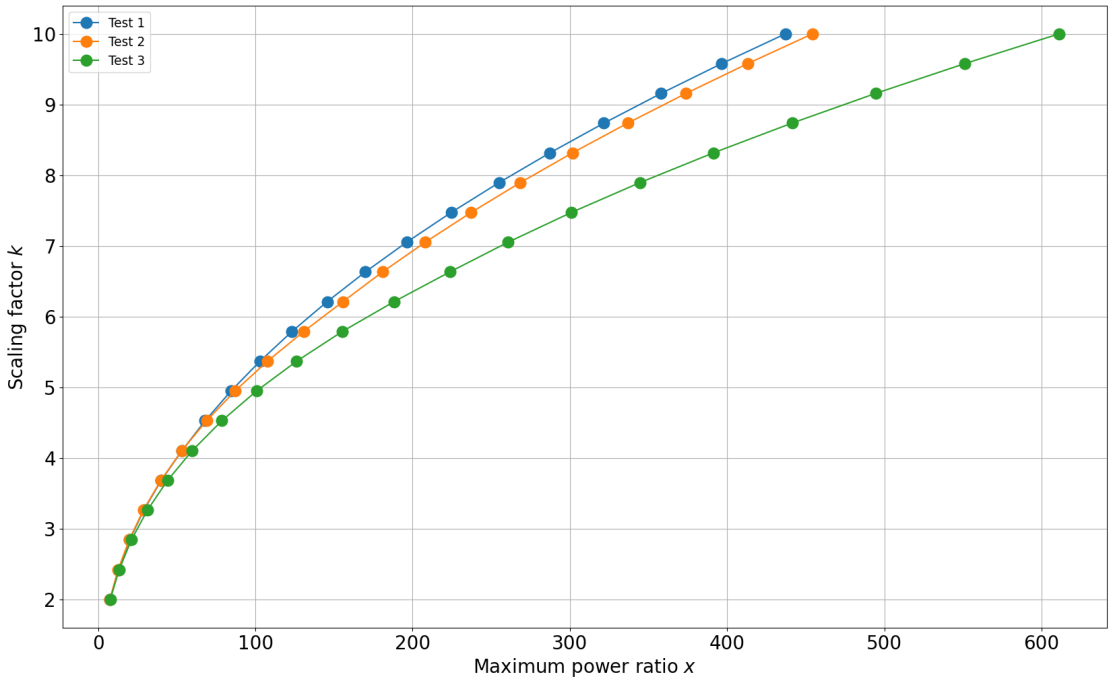

Figure 4.5: Scaling-down factors k plotted against resulting power ratios x for three test cases.

To confirm the logarithmic nature of the relation between k and x, the natural logarithm of both parameters have been plotted against one another, as is shown on

figure 4.6, which highlights that the hypothesis was correct by showing a quasi-linear relationship between $\log(k)$ and $\log(x)$.

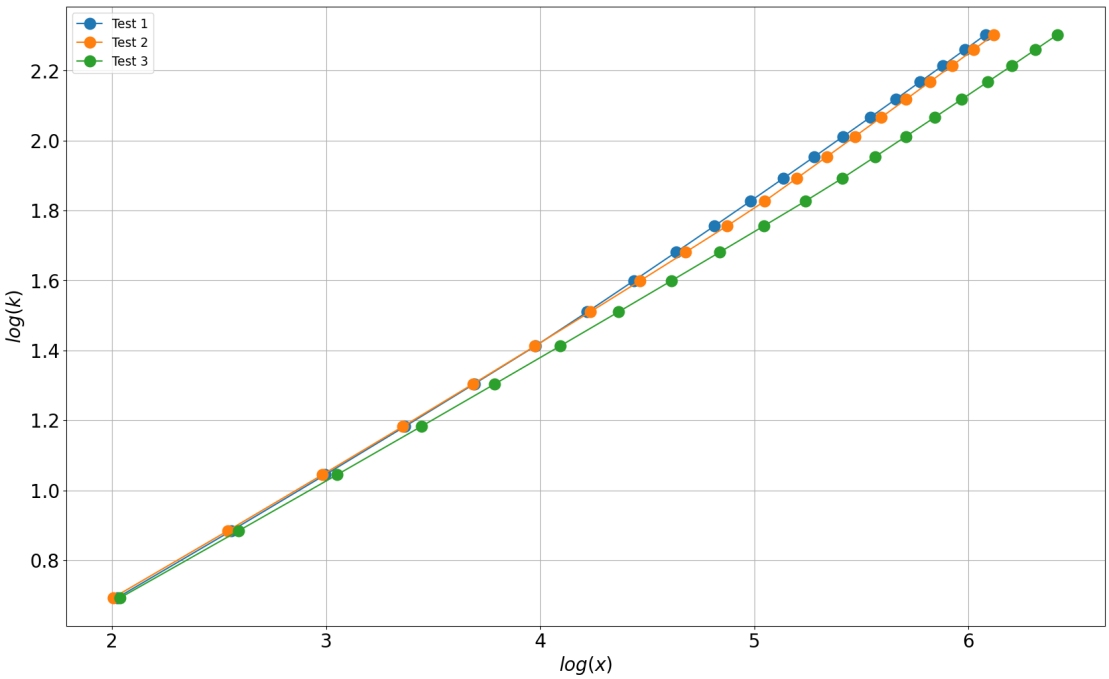

Figure 4.6: Logarithm of scaling-down factors $\log(k)$ plotted against logarithm of resulting power ratios $\log(x)$ for three test cases.

To understand how linear the relation is really is, a linear regression has been conducted for all three cases. The obtained results are plotted on figure 4.7, which shows that assuming the relation between $\log(k)$ and $\log(x)$ to be linear is an excellent approximation ($R^2 > 0.99$). As such, the relation can be written as:

$$\log(k) = a \log(x) + b \tag{4.9}$$

The slope and the vertical offset vary slightly depending on the case studied, as shown by the summary table 4.6. Because there is a high number of parameters for each model, a dedicated and separate study would be necessary to understand what impacts these differences.

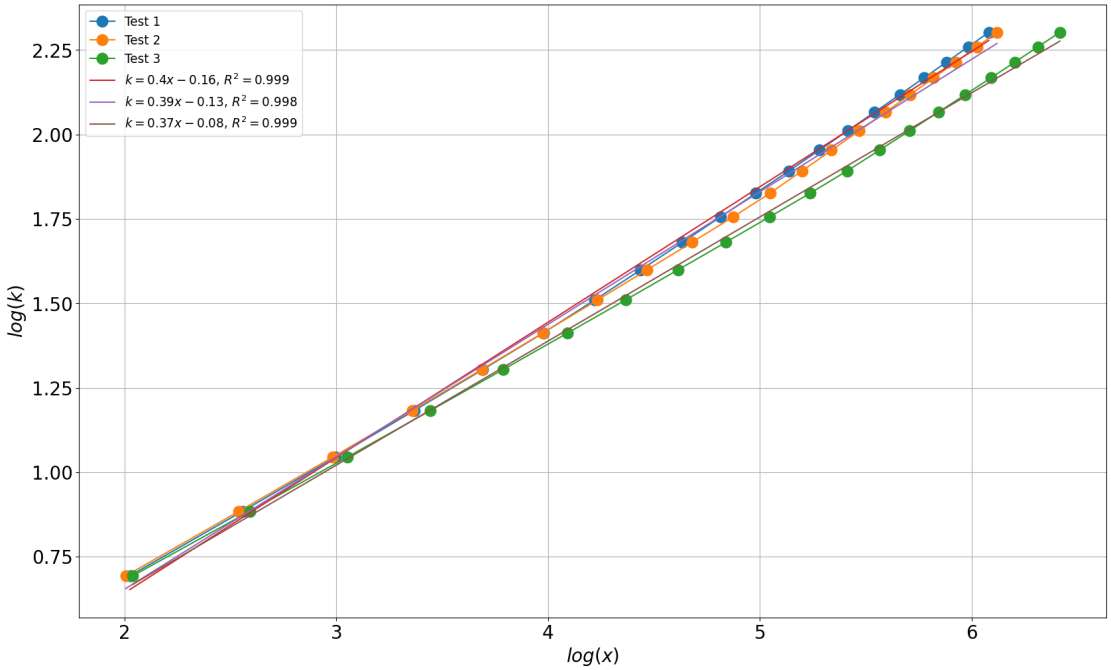

Figure 4.7: Logarithm of scaling-down factors $\log(k)$ plotted against logarithm of resulting power ratios $\log(x)$ and associated linear regressions for three test cases.

	Test 1	**Test 2**	**Test 3**
Slope a	0.40	0.39	0.37
Vertical offset b	-0.16	-0.13	-0.08
Coefficient of determination R^2	0.999	0.998	0.999

Table 4.6: Parameters of the linear regression between $\log(k)$ and $\log(x)$ for three different scenarios.

From equation 4.9 comes the possibility to determine the value of the scaling factor k from a given power ratio x:

$$k = \exp(a \log(x) + b) \tag{4.10}$$

The results obtained with this equation applied using the parameters determined by the linear regression are represented on figure 4.8 along the ground truth (where x has been determined by scaling down the model by k). It highlights that from knowing a and b, an excellent prediction of k knowing the ratio x of the maximum values of the full-scale and scaled-down power requests can be obtained. This is further confirmed by the computation of the relative error between the ground truth and computed values of k, plotted on figure 4.9, which highlights that the relative error is small, with values between -4% and 2.5%.

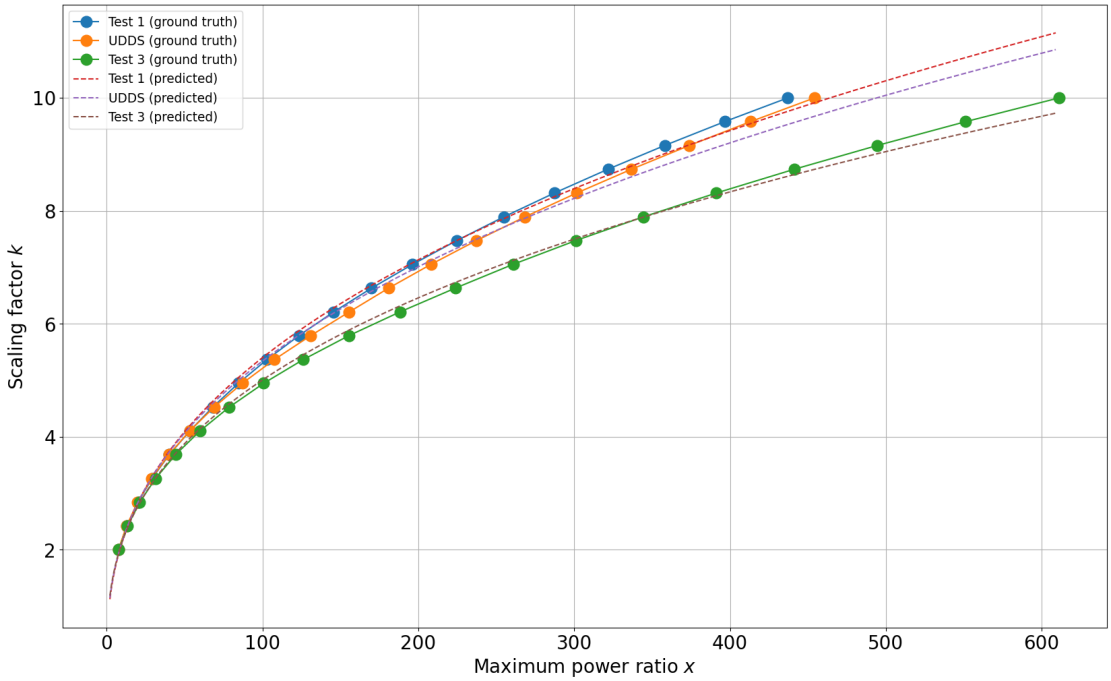

Figure 4.8: Computed and ground truth scaling-down factors k plotted against power ratio x for three test cases.

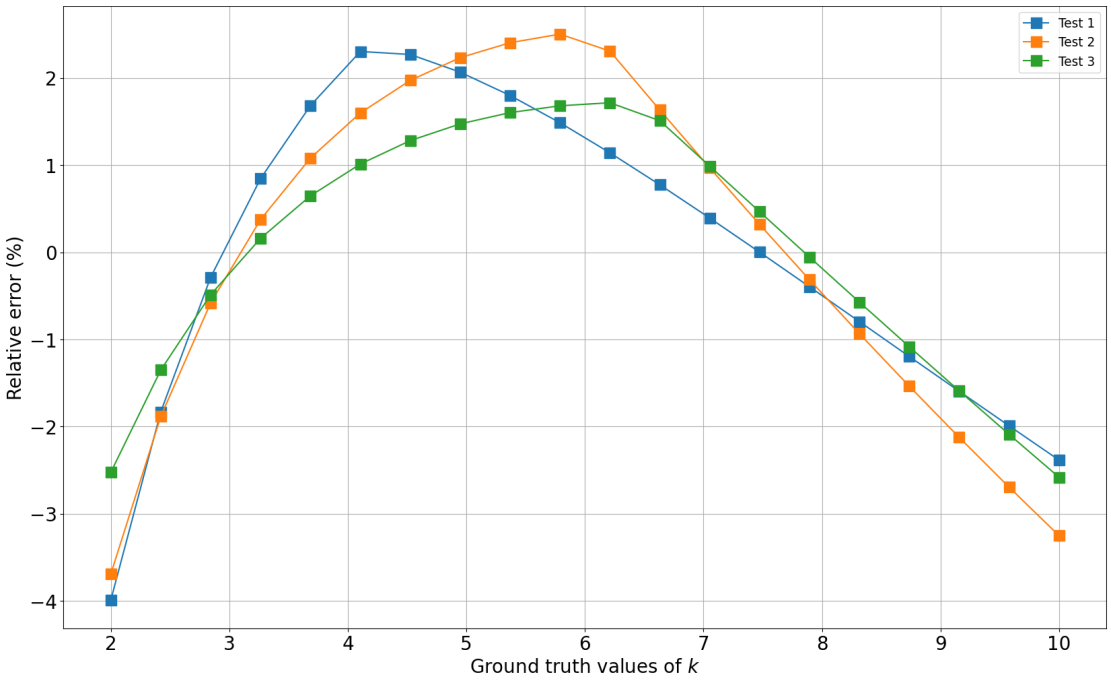

Figure 4.9: Relative difference (in %) between the ground truth values of the scaling-down factor k and the values computed from knowing the power ratio x.

Therefore, it has been found that the scaling-down method studied is compatible with the model at hand, is relevant to the application considered, and allows to easily find any value of the scaling-down factor k by specifying the desired power ratio x once the coefficients of a linear regression have been determined by running the simple model of the resistant forces for as little as 20 values of k.

4.5 Application to test bench

In the context of this thesis, a 140kW electric machine is considered for the vehicle model. For the scaled-down test bench, a 3kW electric machine is considered, which represents a rated power ratio of $\frac{140}{3} = 46.7$.
The rated power of the EM can be, in first approximation, considered to be equivalent to the maximum value of the associated power request, therefore the reverse method detailed above can be applied.
From equation 4.10 and the parameters of the Test 1 case presented in table 4.6, the value of the scaling-down factor k associated to $x = 46.7$ can be evaluated:

$$k = \exp(a \log(x) + b) = \exp(0.4 \log(46.7) - 0.16) = 3.96$$

The associated downscaled power request is plotted on figure 4.10.

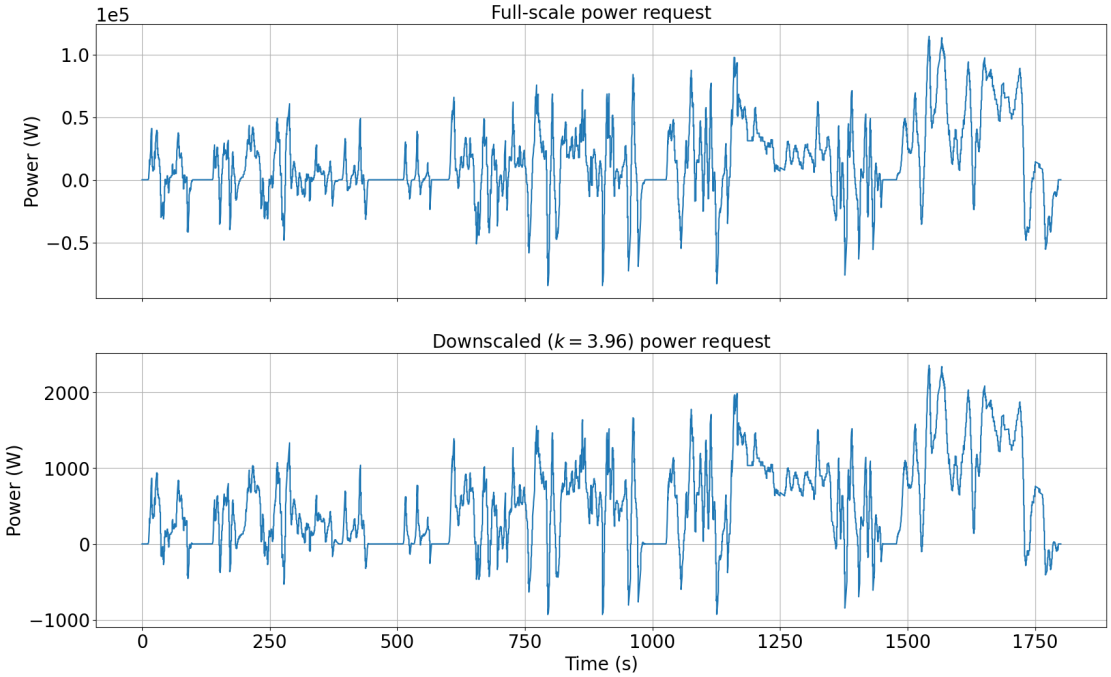

Figure 4.10: Full-scale and down-scaled power request for $k = 3.96$.

Chapter 5

Conclusion

The work developed in this thesis has been conducted in the context of the decarbonization of the automotive industry at the 2050 horizon. Alternative hybrid powertrains were explored and their relevance considered for a commercial light-duty vehicle. To achieve independence from fossil fuels and eliminate Tank-To-Wheel pollutant emissions, the fuel cell hybrid electric vehicle has been chosen as the object of study. The inclusion of supercapacitors as a support to the battery has been reviewed, with the most common power conversion architectures presented. Energy management strategies applied to hybrid electric vehicles have been introduced and examples of use from the literature were presented. The relevance of a scaled-down test bench was justified.

To begin with, a fuel cell hybrid electric vehicle has been modeled, with particular focus on the modeling of the power sources. An architecture with the fuel cell stack in series with the battery has been designed and implemented. The battery has been sized to a capacity of 135.3Ah by considering the impact of a constraining power request on the state of charge and C-rates experienced by the battery. A fuel cell stack model based on two look-up tables has been designed and its slow dynamics have been modelized with a first order low-pass filter with a time constant extrapolated from the literature.

A rule-based control strategy with two working modes has been designed for managing the power delivery of the fuel cell stack, allowing to downsize the battery by 37% with respect to a similar battery electric vehicle while limiting the increase of the C-rates to which it is subjected to values under 3C.

Supercapacitors were introduced in parallel to the battery in order to reduce the C-rates the latter is exposed to. A rule-based control strategy was designed to manage the power distribution between both components. The threshold parameters of this strategy were optimized through two designs of experiments. It was demonstrated that the introduction of the supercapacitors with its optimized energy management strategy resulted in a 10% decrease in the root mean square value of the C-rates experienced by the battery, effectively increasing its life duration.

An adaptive strategy was then developed for the power management of the fuel cell stack by defining a formulation that dynamically minimizes the variations of state of charge while optimizing the efficiency of the fuel cell stack. The efficiency

of this strategy with respect to the rule-based control one has been demonstrated by constraining equal final state of charges over the WLTP cycle, which resulted, with respect to results obtained with rule-based control strategy, in a 2.7% decrease in fuel consumption and a 1.5% reduction of the root mean square value of the C-rates experienced by the battery.

Finally, charge-sustaining mode was achieved with both management strategies by tuning the value of the SOC threshold parameter and the weighting factor of the formulation for the adaptive strategies. By optimizing the efficiency operating window of the fuel cell, the adaptive strategy resulted in fuel economy ranging from 1.6% up to 6.6%, at the cost of an increase in the RMS values of the C-rates ranging from 0.6% and 1.9%.

In the perspective of designing a downscaled test bench, scaling-down methods from the literature were reviewed and one strategy was selected for downscaling the electric machine of the hybrid vehicle. Its compatibility for use in this thesis was ensured by demonstrating a correlation of over 0.98 between the power request computed by the Simulink model and the one computed from the resistance forces at the wheels, regardless of the numerical derivation scheme used for computing the acceleration. The downscaled power request was then computed for several values of the scaling-down factor, resulting in the definition of a range of appropriate values for the factor between 1 and 7. Finally, a robust method for determining the value of the scaling-down factor from any given power ratio without having to compute the resistance forces was developed, resulting in relative errors below 5% in absolute value, regardless of the use case being studied. The method was applied to the electric machine studied in this thesis.

Future works could use the results found in terms of C-rates savings and convert them to quantified battery life gains, even measuring the impact in terms of resources use and associated CO_2 emissions. With respect to the energy management strategies developed throughout this work, a focus could be brought on the improvement of gains by using formalized optimization strategies for the power management of the supercapacitors and the fuel cell stack. Finally, more work needs to be done with respect to the downscaling of the vehicle, in particular at the power sources level, using the results obtained for the electric machine. The logarithmic relation between the scaling-down factor and the maximum or average power ratio could be explored to try and connect the parameters of the linear regression to the parameters of the different models and driving cycles tested.

Appendix A

Bisection results for adaptive strategy in charge-sustaining mode

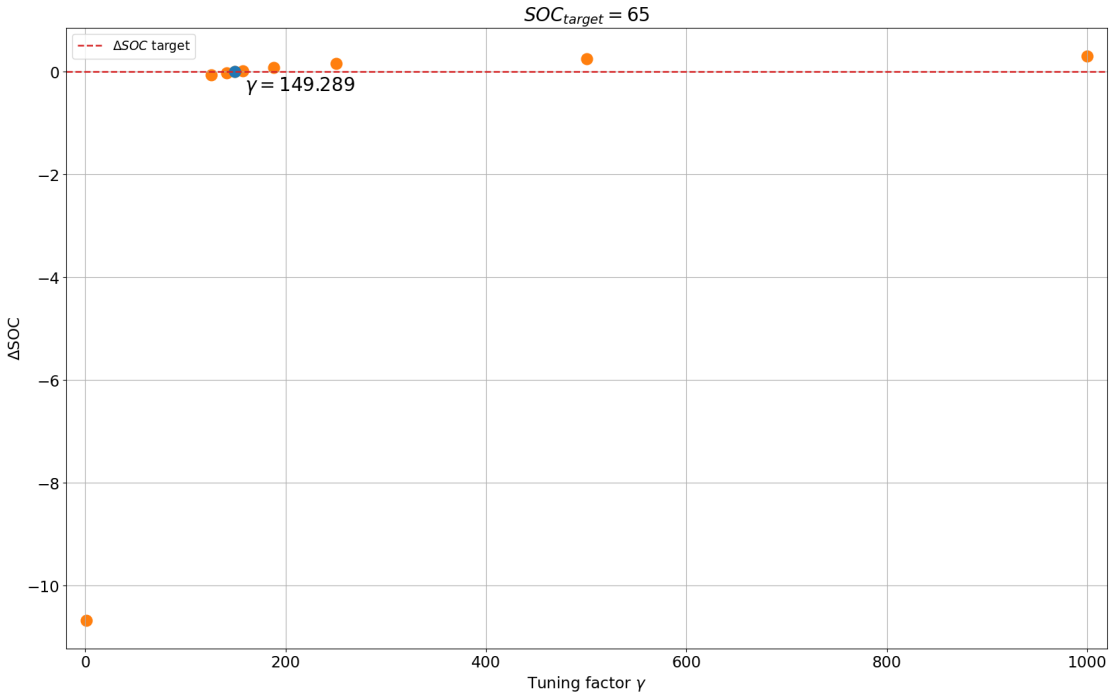

Figure A.1: Tuning of the γ factor through the bisection method to achieve charge-sustaining mode with the adaptive strategy with $SOC_{threshold} = 65\%$.

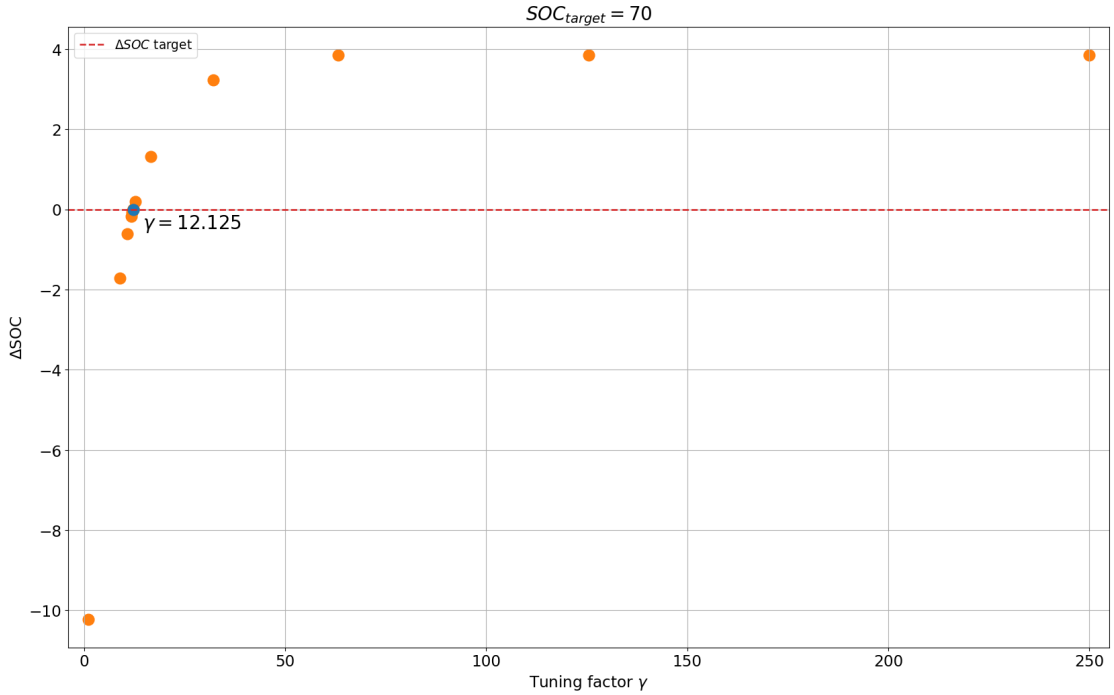

Figure A.2: Tuning of the γ factor through the bisection method to achieve charge-sustaining mode with the adaptive strategy with $SOC_{threshold} = 70\%$.

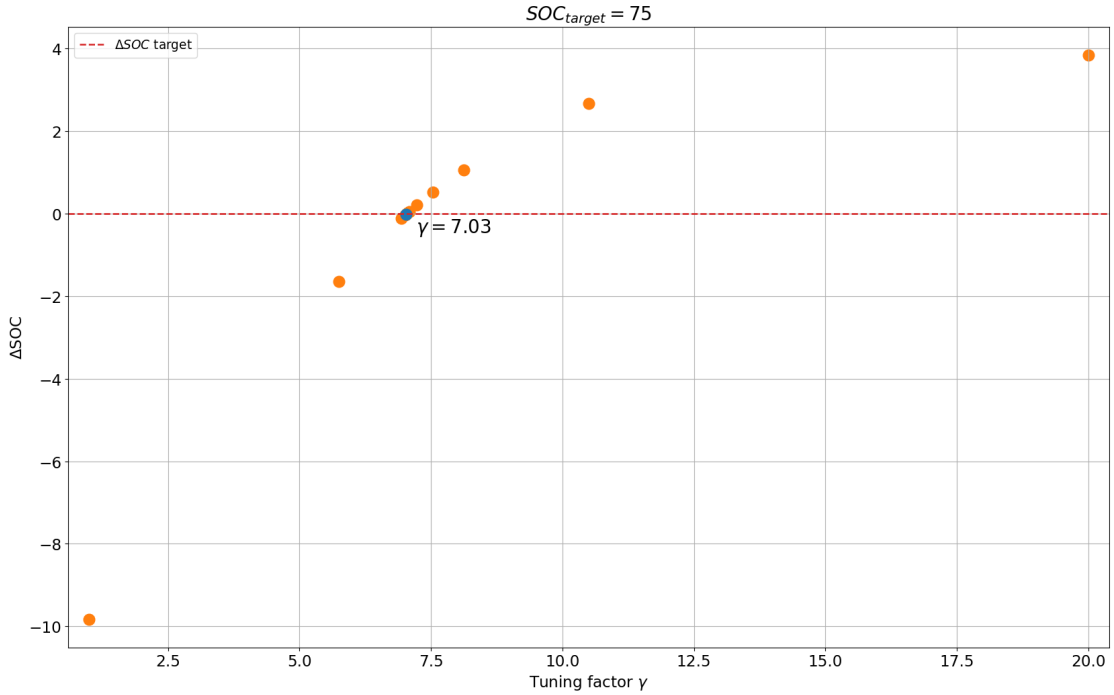

Figure A.3: Tuning of the γ factor through the bisection method to achieve charge-sustaining mode with the adaptive strategy with $SOC_{threshold} = 75\%$.

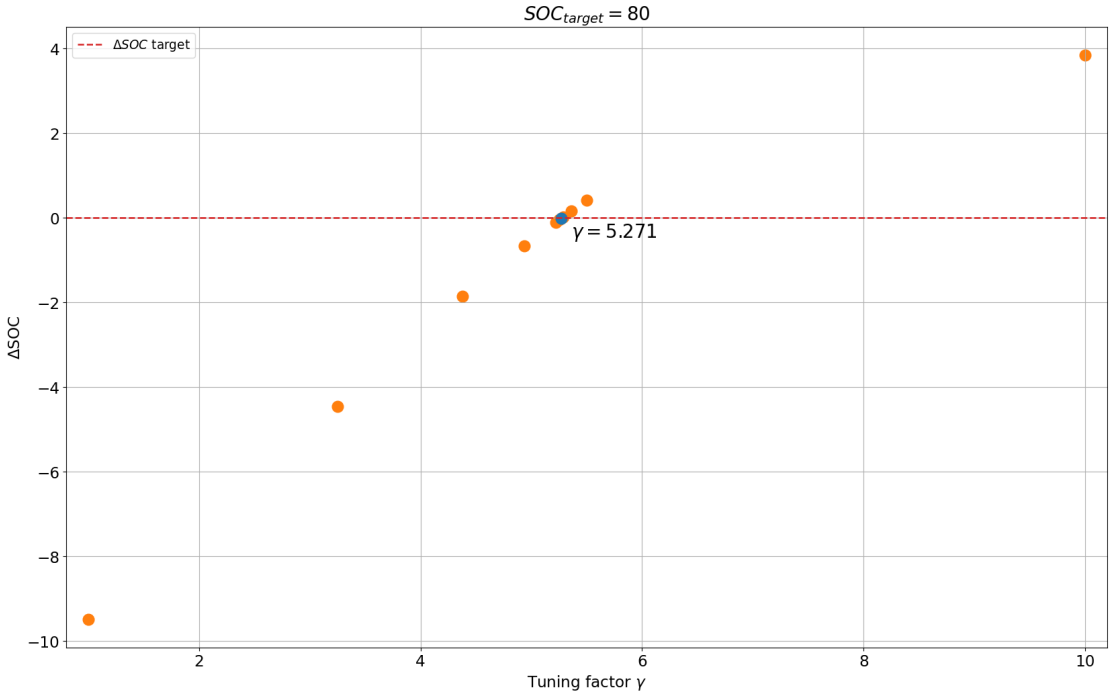

Figure A.4: Tuning of the γ factor through the bisection method to achieve charge-sustaining mode with the adaptive strategy with $SOC_{threshold} = 80\%$.

Bibliography

[1] H. Lee et al. *A Report of the Intergovernmental Panel on Climate Change.* 2023. URL: https://www.ipcc.ch/report/ar6/syr/ (visited on 08/28/2023).

[2] S. Acevedo et al. *Climate Change Will Bring More Frequent Natural Disasters Weigh on Economic Growth.* 2017. URL: https://www.imf.org/en/Blogs/Articles/2017/11/16/climate-change-will-bring-more-frequent-natural-disasters-weigh-on-economic-growth (visited on 07/28/2023).

[3] S. Keller. *A world of thoughts on Phase 2.* 2016. URL: https://theicct.org/a-world-of-thoughts-on-phase-2/ (visited on 09/27/2023).

[4] Y. Wang et al. «The impact of the corporate average fuel economy standards on technological changes in automobile fuel efficiency». In: *Resource and Energy Economics* (2021). DOI: https://doi.org/10.1016/j.reseneeco.2020.101211.

[5] T. Haas et al. «Decarbonizing Transport in the European Union: Emission Performance Standards and the Perspectives for a European Green Deal». In: *Sustainability* (2020). DOI: https://doi.org/10.3390/su12208381.

[6] G. Subramanian et al. «Integrated Li-Ion Battery and Super Capacitor based Hybrid Energy Storage System for Electric Vehicles». In: *IEEE International Conference on Electronics, Computing and Communication Technologies* (2020). DOI: https://doi.org/10.1109/CONECCT50063.2020.9198317.

[7] A. Lajunen et al. «Lifecycle cost assessment and carbon dioxide emissions of diesel, natural gas, hybrid electric, fuel cell hybrid and electric transit buses». In: *Energy* (2016). DOI: https://doi.org/10.1016/j.energy.2016.03.075.

[8] A. García et al. «Life cycle CO footprint reduction comparison of hybrid and electric buses for bus transit networks». In: *Applied Energy* (2022). DOI: https://doi.org/10.1016/j.apenergy.2021.118354.

[9] E. Emilsson et al. *Lithium-Ion Vehicle Battery Production - Status 2019 on Energy Use, CO2 Emissions, Use of Metals, Products Environmental Footprint, and Recycling.* 2019. URL: https://www.ivl.se/english/ivl/publications/publications/lithium-ion-vehicle-battery-production----status-2019-on-energy-use-co2-emissions-use-of-metals-products-environmental-footprint-and-recycling.html (visited on 09/13/2023).

[10] S. Mothilal Bhagavathy et al. «Impact of Charging Rates on Electric Vehicle Battery Life». In: *Findings* (2021). DOI: https://doi.org/10.32866/001c.21459.

[11] C. Cunanan et al. «A Review of Heavy-Duty Vehicle Powertrain Technologies: Diesel Engine Vehicles, Battery Electric Vehicles, and Hydrogen Fuel Cell Electric Vehicles». In: *Clean Technologies* (2021). DOI: https://doi.org/10.3390/cleantechnol3020028.

[12] C. C. Chan et al. «Electric, Hybrid, and Fuel-Cell Vehicles: Architectures and Modeling». In: *IEEE Transactions on Vehicular Technology* (2010). DOI: https://doi.org/10.1109/TVT.2009.2033605.

[13] C. Shen et al. «A Comprehensive Overview of Hybrid Electric Vehicles». In: *International Journal of Vehicular Technology* (2011). DOI: https://doi.org/10.1155/2011/571683.

[14] N. N. Mustafi. «An Overview of Hybrid Electric Vehicle Technology». In: *Engines and Fuels for Future Transport* (2021). DOI: https://doi.org/10.1007/978-981-16-8717-4_5.

[15] International Energy Agency. *World Energy Outlook Special Report*. 2016. URL: https://www.iea.org/reports/energy-and-air-pollution (visited on 09/27/2023).

[16] U.S. Energy Information Administration. «Hydrogen explained - Production of hydrogen». In: *U.S. Energy Information Administration* (2023). DOI: https://www.eia.gov/energyexplained/hydrogen/production-of-hydrogen.php.

[17] A. González et al. «Review on supercapacitors: Technologies and materials». In: *Renewable and Sustainable Energy Reviews* (2016). DOI: https://doi.org/10.1016/j.rser.2015.12.249.

[18] J. Libich et al. «Supercapacitors: Properties and applications». In: *Journal of Energy Storage* (2018). DOI: https://doi.org/10.1016/j.est.2018.03.012.

[19] J. J. Lamb et al. «Lithium-Ion Capacitors: A Review of Design and Active Materials». In: *Energies* (2021). DOI: https://doi.org/10.3390/en14040979.

[20] L. Kouchachvili et al. «Hybrid battery/supercapacitor energy storage system for the electric vehicles». In: *Journal of Power Sources* (2018). DOI: https://doi.org/10.1016/j.jpowsour.2017.11.040.

[21] C. Xiang et al. «A New Topology and Control Strategy for a Hybrid Battery-Ultracapacitor Energy Storage System». In: *Energies* (2014). DOI: https://doi.org/10.3390/en7052874.

[22] V. K. Kasimalla et al. «A review on energy allocation of fuel cell/battery/ultracapacitor for hybrid electric vehicles». In: *International Journal of Energy Research* (2018). DOI: https://doi.org/10.1002/er.4166.

[23] J. H. Wong et al. «Parallel configuration in energy management control for the fuel cell-battery-ultracapacitor hybrid vehicles». In: *IEEE Applied Power Electronics Colloquium* (2011). DOI: https://doi.org/10.1109/IAPEC.2011.5779870.

[24] I. Oukkacha et al. «Energy Management in Electric Vehicle based on Frequency sharing approach, using Fuel cells, Lithium batteries and Supercapacitors». In: *IEEE International Conference on Renewable Energy Research and Applications* (2018). DOI: https://doi.org/10.1109/ICRERA.2018.8566991.

[25] P. Thounthong et al. «Energy management of fuel cell/battery/supercapacitor hybrid power source for vehicle applications». In: *Journal of Power Sources* (2009). DOI: https://doi.org/10.1016/j.jpowsour.2008.12.120.

[26] O. El Ganaoui-Mourlan et al. «Design of a flexible hybrid powertrain using a 48V-battery and a supercapacitor for ultra-light urban vehicles». In: *SAE Technical Paper* (2020). DOI: https://doi.org/10.4271/2020-01-0445.

[27] Z. Fu et al. «A hierarchical energy management strategy for fuel cell/battery/-supercapacitor hybrid electric vehicles». In: *International Journal of Hydrogen Energy* (2021). DOI: https://doi.org/10.1016/j.ijhydene.2019.06.158.

[28] S. Park et al. «Power and Thermal Management with Battery Degradation for Hybrid Electric Vehicles». In: *IEEE Conference on Control Technology and Applications* (2021). DOI: https://doi.org/10.1109/CCTA48906.2021.9659119.

[29] C. Yang et al. «Efficient energy management strategy for hybrid electric vehicles/plug-in hybrid electric vehicles: review and recent advances under intelligent transportation system». In: *IET Intelligent Transport Systems* (2020). DOI: https://doi.org/10.1049/iet-its.2019.0606.

[30] Y. Zhang et al. «A two-layer hierarchical optimization framework for the operational management of diesel/battery/supercapacitor hybrid powered vehicular propulsion systems». In: *Journal of Cleaner Production* (2022). DOI: https://doi.org/10.1016/j.jclepro.2022.134658.

[31] I. Shafikhani et al. «MPC-based energy management system design for a series HEV with battery life optimization». In: *IEEE European Control Conference* (2021). DOI: https://doi.org/10.23919/ECC54610.2021.9655224.

[32] M. B. Camara et al. «Supercapacitors and battery power management for hybrid vehicle applications using multi boost and full bridge converters». In: *IEEE European Conference on Power Electronics and Applications* (2007). DOI: https://doi.org/10.1109/EPE.2007.4417315.

[33] M. B. Camara et al. «Design and New Control of DC/DC Converters to Share Energy Between Supercapacitors and Batteries in Hybrid Vehicles». In: *IEEE Transactions on Vehicular Technology* (2008). DOI: https://doi.org/10.1109/TVT.2008.915491.

[34] Sustainable Bus. *Here it comes the Iveco eDaily with fuel cell. The launch at IAA (with BEV version)*. 2022. URL: https://www.sustainable-bus.com/news/iveco-edaily-fuel-cell-iaa/ (visited on 08/08/2023).

[35] IVECO. *IVECO Daily*. 2022. URL: https://www.iveco.com/italy/Daily (visited on 07/15/2023).

[36] J. Beretta. *Automotive Electricity: Electric Drives*. Wiley-ISTE, 2010.

[37] P. Bubna et al. «Analysis, operation and maintenance of a fuel cell/battery series-hybrid bus for urban transit applications». In: *Journal of Power Sources* (2010). DOI: https://doi.org/10.1016/j.jpowsour.2009.12.080.

[38] Sustainable Bus. *Iveco Bus turns to Microvast (with FPT) for future electric Crossway battery system*. 2022. URL: https://www.sustainable-bus.com/news/microvast-fpt-iveco-bus-crossway-electric/ (visited on 08/14/2023).

[39] R. Negroiu et al. «Comparison between Zubieta model of supercapacitors and their real behavior». In: *IEEE International Symposium for Design and Technology in Electronic Packaging* (2016). DOI: https://doi.org/10.1109/SIITME.2016.7777276.

[40] H. Miniguano et al. «A General Parameter Identification Procedure Used for the Comparative Study of Supercapacitors Models». In: *Energies* (2019). DOI: https://doi.org/10.3390/en12091776.

[41] S. V. Rajani et al. «Experimental validation of the ultracapacitor parameters using the method of averaging for photovoltaic applications». In: *Journal of Energy Storage* (2016). DOI: https://doi.org/10.1016/j.est.2015.12.002.

[42] S. Pezzolato. *Modeling and Model Validation of Supercapacitors for Real-Time Simulations*. 2019. URL: https://amslaurea.unibo.it/20083/.

[43] M. Novak et al. «Drive Cycle Modeling of a Hybrid Bus with Fuel Cell». In: *IEEE Industrial Electronics Society* (2022). DOI: https://doi.org/10.1109/IECON49645.2022.9968796.

[44] J. Bauman et al. «A Comparative Study of Fuel-Cell–Battery, Fuel-Cell–Ultracapacitor, and Fuel-Cell–Battery–Ultracapacitor Vehicles». In: *IEEE Transactions on Vehicular Technology* (2008). DOI: https://doi.org/10.1109/TVT.2007.906379.

[45] A. Ahuja et al. «Fuel Cell Technologies for Automotive Applications». In: *Journal of Power Electronics and Power Systems* (2022). DOI: https://doi.org/10.37591/JoPEPS.

[46] W. Xin et al. «Energy Management of Fuel Cell Vehicles Based on Model Prediction Control Using Radial Basis Functions». In: *Journal of Sensors* (2021). DOI: https://doi.org/10.1155/2021/9985063.

[47] J. Jia et al. «Modeling and Dynamic Characteristic Simulation of a Proton Exchange Membrane Fuel Cell». In: *IEEE Transactions on Energy Conversion* (2009). DOI: https://doi.org/10.1109/TEC.2008.2011837.

[48] Toyota Motor Italia - Marketing Department. *Toyota MIRAI Technical Sheet*. 2023. URL: https://www.toyota.it/content/dam/toyota/nmsc/italy/gamma/pdf/scheda-tecnica/MIRAI_Scheda_tecnica.pdf (visited on 08/09/2023).

[49] Pod Point. *IVECO eDaily Van (2023)*. 2023. URL: https://pod-point.com/guides/vehicles/iveco/2023/edaily (visited on 09/02/2023).

[50] J. Cao et al. «A New Battery/UltraCapacitor Hybrid Energy Storage System for Electric, Hybrid, and Plug-In Hybrid Electric Vehicles». In: *IEEE Transactions On Power Electronics* (2011). DOI: https://doi.org/10.1109/TPEL.2011.2151206.

[51] M. Kardasz et al. «Systematic electric vehicle scaling for test bed simulation». In: *IEEE Transportation Electrification Conference and Expo* (2016). DOI: https://doi.org/10.1109/ITEC.2016.7520189.

[52] M. R. Kardasz. *Design and Implementation of a Modular Test Bed Platform for Hardware-In-the-Loop Simulation of Electric Vehicles*. 2019. URL: http://hdl.handle.net/10012/14769.

[53] M. D. Petersehim et al. «Scaling of hybrid-electric vehicle powertrain components for Hardware-in-the-loop simulation». In: *Mechatronics* (2009). DOI: https://doi.org/10.1016/j.mechatronics.2009.08.001.

[54] J. M. Cabello et al. «Scaling Electrochemical Battery Models for Time-Accelerated and Size-Scaled Experiments on Test-Benches». In: *IEEE Transactions on Power Systems* (2017). DOI: https://doi.org/10.1109/TPWRS.2017.2683398.

[55] R. Verma et al. «Development of a Scaled Vehicle With Longitudinal Dynamics of an HMMWV for an ITS Testbed». In: *IEEE/ASME Transactions on Mechatronics* (2008). DOI: https://doi.org/10.1109/TMECH.2008.915820.

[56] M. Hadartz et al. *Battery-Supercapacitor Energy Storage*. 2008. URL: https://hdl.handle.net/20.500.12380/82857.